國立臺灣大學理學院地質科學研究所

碩士論文

Department of Geosciences

College of Science

National Taiwan University

Master Thesis

大屯山與台北盆地鄰近區域地下速度構造分析

A Study of the Tomography and Seismicity in Taipei Basin and Tatun Volcano Regions, Taiwan and Their Structural Implications

林郁梅

Yu-Mei Lin

指導教授：吳逸民 博士

林正洪 博士

Advisor: Yih-Min Wu, Ph.D.

Cheng-Horng Lin, Ph.D.

中華民國 九十八 年 一 月

January, 2009

國立臺灣大學碩士學位論文
口試委員會審定書

大屯山與台北盆地鄰近區域地下速度構造分析
A Study of the Tomography and Seismicity in Taipei Basin and Tatun Volcano Regions, Taiwan and Their Structural Implications

本論文係林郁梅君（R94224102）在國立臺灣大學地質學系所完成之碩士學位論文，於民國九十八年一月十六日承下列考試委員審查通過及口試及格，特此證明

口試委員：吳逸民 林正洪（簽名）

（指導教授）

黃柏壽

張崇岳

ACKNOWLEDEGMENT

誌謝

這一頁雖然置於論文的開頭，卻是整本論文最後書寫的。寫到此，代表碩士生涯已告一段落，即將展開另一段旅程。回顧過去的這兩年半的時間，有很多很多要感謝的人，如果沒有這些指引、陪伴與扶持，讀研究所的路程或許會更苦悶。

首先想感謝的人是我研究路程的啟蒙者 林正洪老師。在大學階段給予我至中研院地球所學習的機會，兩個月的暑期生生活雖然看似很短，卻是我踏上地震學領域的契機。再來尤其要感謝的是中大蒲新杰學長，從當暑期生開始對於我的細心與不倦的指導，到後來一直是我請益的對象，感謝有你在學術上一路的幫忙與指引。進入台大地質就讀之後，感謝我的指導教授 吳逸民老師在生活上的關照與學術上很大資源的幫助，兩次美國地質年會的參與拓展了我的視野與經驗，老師大力的督促和支持，讓我比其他人擁有更多的機會。也感謝老師給予我很大的自由空間，學習自己成長，雖然過程很辛苦，卻是受用無窮。 龔源成老師、 洪淑惠老師與 喬凌雲老師則是我地震學領域的啟蒙者與良師，感謝三位老師孜孜不倦的教導，讓學生從零開始學習、理解了地震學的範疇。然後是很感激氣象局 張建興老師、地球所 黃文紀老師與 黃柏壽老師在資料與技術上的鼎力幫忙，尤其是張建興老師柔和的談吐與耐心的指導，對學生來說有如沙漠中的綠洲般親切。

同研究室的宜芬、道霖、信樺、阿天、阿狗、心儀學姊、秉延、芳儒、煒婷、韋安、章天、中研院林老師的助理小阿姨、在系館的永翔、胡老師研究室的筱婷、童忻、詠恬、楊宜蓉學姊以及龔老師和洪老師研究室的哲緯、水輝、雅婷、一帆、欣穎學姊、燕玲學姊，感謝你們不管在生活上以及學術上的一路相伴與扶持，碩士生活因為有你們而不孤單。再來是 陳于高老師及其研究室的諸位-嘉俞、憶菁、施威廉、阿和、鴉哥、蛋哥、韶怡學姊、珀儂學長、小黑學姊，能認識你們並跟你們相處在同一研究室真好！每天只要聽到 y 高老師爽朗的聲音，就會覺得很有活力與精神。也很感謝 y 高老師對我的照顧！中研院的小高、麗琴、溫老大、阿斌哥、林瑞仁，很感謝你們帶領並照顧我一起出野外的時光，讓我了解野外實地架設測站是怎麼一回事，也一起度過了在中研院學習的那段日子。

最後是給我最誠摯的親朋好友們：怡潔、小魁、小卓、詩盈跟我親愛的家人-爸爸、媽媽、弟弟和最可愛的妹妹，你們不管快樂或低潮時，一直陪伴在我身邊，同我分享所有的一切、走過所有的時期，感謝有你們！

中文摘要

位於台灣北部地區的台北盆地主要是由山腳斷層的陷落活動與未固結之第四紀沈積層所形成的鬆軟沈積盆地。大屯火山群則緊鄰於台北盆地之北緣，而目前大屯火山群仍有很明顯的後火山活動現象。台北盆地地區的地震活動度相當低，但相較來說，在大屯火山群之區域則觀測到不少的微震活動。因此，瞭解台北盆地與大屯火山群地區的地震構造是相當重要的工作。

於本研究當中，為了提升分析結果之解析度，增加了波線覆蓋率，總計使用四個佈置於台北與大屯火山地區的地震觀測網資料，對地震波做波相定位，並與地震目錄整合以建立該地區之地震層析影像。此四個地震觀測網分別為兩個小區域臨時監測網與中央氣象局負責之 CWBSN、TSMIP 監測網。從 1979 年至 2007 年之所有地震目錄中，共選用了 6861 個至少被 7 個測站所記錄的地震事件，用以進行 Vp 以及 Vp/Vs 的地下波速構造反演，並分析該區域其震源機制解之情況。

於最後層析影像結果中，在研究地區下呈現一低 Vp/Vs 比值的連續區域，與山腳斷層的地表分佈頗為一致，而於其上之高 Vp/Vs 比值區域則反應了鬆軟的台北盆地地區。此外，大屯火山群底下於淺部是低 Vp/Vs 比值、高 Vp 的區域，此即是反映了淺層已固結的堅硬火成岩體。

大屯火山地區之下的微震活動經重定位後可將其區分成兩群地震，此兩群地震分別位於七星山以及大油坑跟馬槽底下，而該區域地表則皆有頻繁的地熱活動現象。使用 P 波初動的方法得此區的震源機制皆是具有走向滑移分量的正斷層，但這些震源機制解之走向與傾角的差異極大，此種現象在火山活動地區極為常見。該區域之微震活動分佈可能是反應了大屯山底下的岩層破碎情況，並形成暢通的噴發管道路徑，以供氣體或者液體於大屯火山群底下流通。

因此，根據地震震源位置及其震源機制解的特性，本研究推論這些微震活動與金山斷層的關連性較小，而此兩群地震在空間分佈上的走向不太一樣，也可能

暗示了大屯火山地區的地熱活動可能有多處來源。

關鍵詞：層析影像法、大屯火山群、台北盆地

ABSTRACT

The Taipei Basin with ‘soft’ deposit in the north of Taiwan has been produced by the motion of the Shanchiao fault. To the north, Tatun Volcano Group (TVG) which has post-volcanic activities is located adjacent to Taipei Basin. The local seismicity in Taipei Basin is very low. On the contrary, there are quite a few micro-earthquakes being detected in TVG. Therefore, it is very important to understand the seismotectonics of the Taipei Basin and TVG.

In this research, in order to increase ray path coverage and improve the resolution, I picked the seismic arrival times and combined the earthquake catalogs from two local temporary seismic networks located in Taipei and Tatun region, the Central Weather Bureau Seismic Network (CWBSN) and the Taiwan Strong Motion Instrumentation Program (TSMIP) to establish a new seismic tomography image. Totally, 6861 events detected at more than 7 stations during periods from 1979 to 2007 were used to determine *Vp* and *Vp*/*Vs* structures as well as focal mechanisms.

In our tomography results, the pattern of low *Vp*/*Vs* ratio in this region seems to coincide with the Shanchiao fault, and the region with high *Vp*/*Vs* ratio above it reveals that the effects of basin amplification affects about several kilometers. Besides, the shallow region with low *Vp*/*Vs* and high *Vp* beneath TVG should represent the solidified igneous rocks.

The hypocenter distribution of micro-earthquakes beneath TVG can be classified into two groups. These two seismogenic zones at the shallow portion are coincident with the surface hydrothermal regions with hot spring and fumaroles. Those regions include Chishing Mountain, Matsao and Tayukeng. The focal mechanisms of those earthquakes are normal fault types with strike-slip component by using P wave first motions and

these solutions have various strikes and dips even the events are close in time and spatial windows. This phenomenon is commonly observed in a volcanic area. Thus, those earthquakes may reflect the broken zone and unobstructed conduits exist beneath the TVG and the gas and liquid can pass through.

So, based on the hypocenter distribution and focal mechanism solutions, it seems that these earthquakes are weakly correlated with the nearest fault - Chinshan fault. Besides, these two seismogenic zones incline to different directions and may imply that they are different passageways for the hydrothermal fluid and gas to ascend along from different sources.

Key words: tomography, Tatun Volcano Group, Taipei Basin

TABLE OF CONTENTS

LIST OF FIGURES

LIST OF TABLES

Chapter 1 Introduction

1.1 Motivation and Goal

Whether a volcano is active or not is generally defined as “a volcano with recently historical eruptions within the past few centuries or a volcano currently erupting”. So, if one volcano is inactive for a long time as compared to human history, it will be ascribed to the groups of quiescence stage or extinct stage. But, the recorded human history is very short as compared with the earth history and the properties of volcanoes also vary widely in the world. Thus, the traditional usage of “recorded eruptions” as a criterion to define the volcano is active or not is inappropriate.

Tatun Volcano Group (TVG) lies in the north of Taipei Basin in which the capital of Taiwan, Taipei City, is situated. Although TVG is broadly considered to be extinct because of a long repose time, some recent studies have suggested that the magma chamber may still exist beneath this region (Yang et al., 1999; Konstantinou et al., 2007; Lee et al., 2008). As we know that the post-volcanic activities in this area are still active and the spectacular sightseeing and the wonderful hot-springs attract a lot of visitors coming every year. But, if the magma chamber really exists, the possibility of the further volcanic activity and the capability of eruption should not be completely excluded. So, it is very important to study the subsurface structures around TVG and its possible eruption behavior.

Recently, several authors have examined the cause of the active post-volcanic activities in TVG, and the methods have included seismicity, geochemistry, topography etc (Lin et al., 2005a, 2005b; Konstantinou et al., 2007; Chan et al., 2006; Murase et al., 2007; Lee et al., 2008). But little literature has been published on seismic tomographic

imaging. The lack of such information represents a gap in our knowledge of the subsurface structure. A detailed seismic tomography can help us more comprehensively understand the interior state of TVG. Thus, the seismicity distribution and seismic velocity structure were investigated in this study. Furthermore, the seismic velocity distribution can reflect the properties of the rocks beneath TVG.

1.2 Summary Preview

Data from several seismic networks — two local temporary arrays, the Central Weather Bureau Seismic Network and Taiwan Strong Motion Instrumentation Program were combined. The body wave travel-time inversion method was used to simulate the tomographic images beneath the Taipei Basin and TVG surrounding area. Results from relocated hypocenter distribution and first-motion focal mechanisms were investigated to understand the seismogenic structures and its tectonic implications.

Totally, there are six chapters in this thesis. The motivation is introduced in chapter 1 and chapter 2 will address on the local geological background and most of the previous research in this study area. The seismic networks will be introduced in chapter 3. In chapter 4, the research procedure and methods of travel time inversion used in this study will be described. Finally, chapters 5 and 6 present the results and conclusions, respectively.

Chapter 2 Geological Background

2.1 Local Geological Background

Taiwan is located at the junction between the Philippine Sea Plate (PSP) and the Eurasian Plate (EP). According to the GPS measurements, the Philippine Sea Plate is moving toward the northwest (306°±1°) at a rate of about 82mm/yr (Yu et al., 1997).

Seismicity and geological features in Taiwan are closely related to the collision zone between two active subduction systems. The PSP is subducting beneath the EP at the Ryukyu trench in the northeast of Taiwan, and the Eurasian oceanic lithosphere of the South China Sea is subducting eastward beneath the Philippine Sea Plate in the south as shown in Figure 1. In addition, the PSP and the EP are colliding in the eastern Taiwan and the N-S trending geologic and tectonic features in Taiwan are generally accepted to be caused by the obliquely collision between the Luzon arc on the PSP and the Eurasian continental margin. Besides, The orogeny in Taiwan is relatively young in a geologic time scale and has just started about 5 Ma (Suppe, 1984). Based on results from field observations, tectonic analysis, geophysical data and experimental modeling, Lu et al. (1995) pointed out that contraction, transcurrent faulting, block rotation and extension are four essential tectonic mechanisms that dominate the oblique convergence and collision tectonics of the northern Taiwan region. They also concluded that extensional structures such as the Taipei Basin in the north of Taiwan have developed in response to increase belt curvature and related block rotations (Figure 2).

However, the Okinawa Trough, a back-arc basin dominated by extensional tectonics behind the Ryukyu trench-arc system, could be a cause to affect the tectonic development of the northern Taiwan (Figure 1). Teng (1996) proposed that the northern

part of the orogeny in Taiwan is subjected to crustal stretching and rifting as a result of flipping of subduction from the northwest-facing Luzon arc system to the south-facing Ryukyu arc system as shown in Figure 3. From a study of two-dimensional elasto-plastic finite-element modeling in and around Taiwan, Hu et al. (1996, 2002) proposed the crustal deformation in the Ryukyu-Taiwan area is controlled by two major factor: the indentation of the PSP into EP and the trench retreat due to suction at the Ryukyu trench (Figure 4).

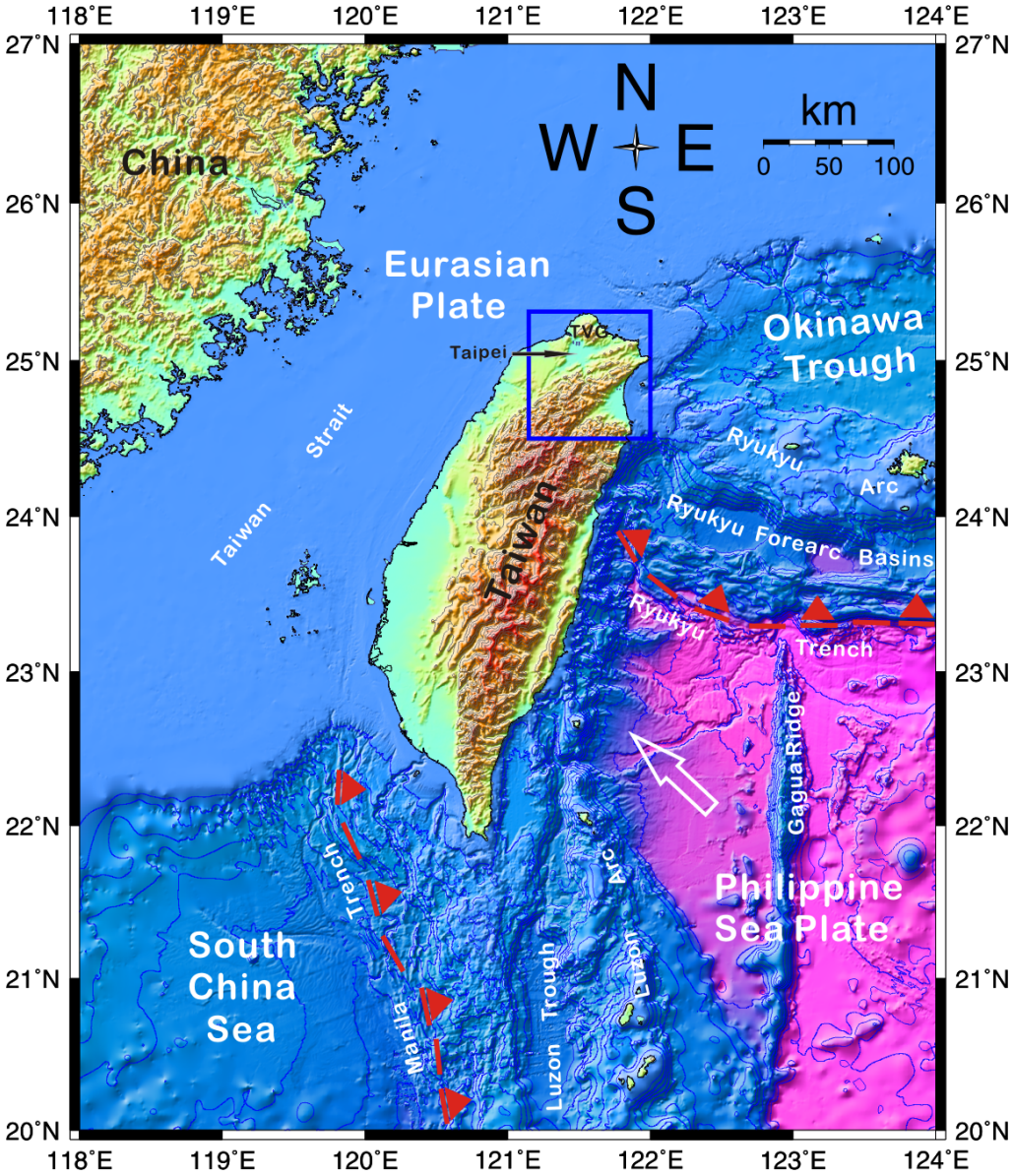

Figure 1. Geological settings of the Taiwan surrounding area. The blue square shows the study area.

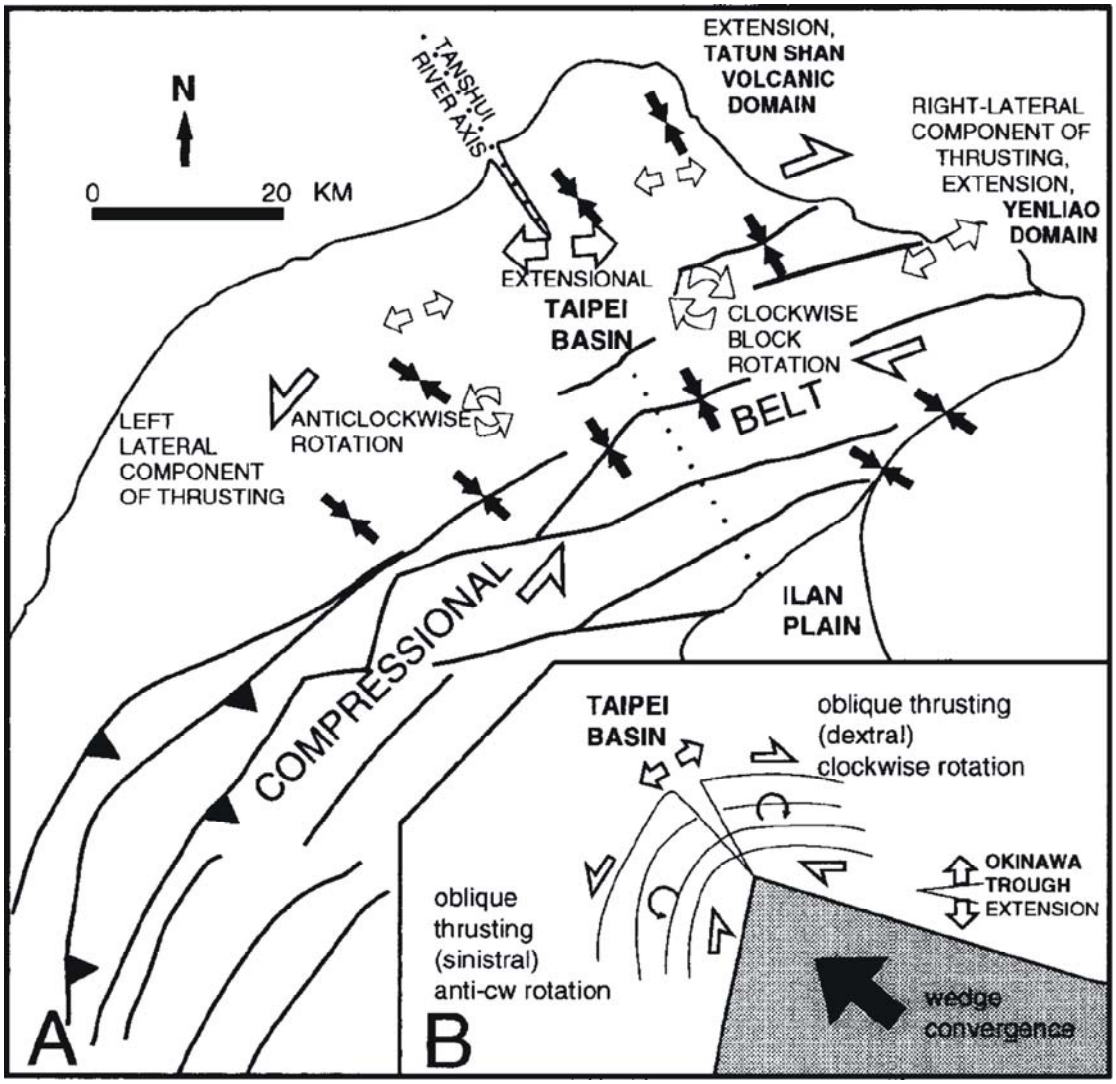

Figure 2. Model of the tectonic deformation in northern Taiwan. (A) An interpretative map is summarized to explain the tectonic model of northern Taiwan. (B) An explanatory sketch is proposed to interpret all geological features in Figure 2A. They are the result of an indentation by a wedge-shaped back-stop. (Lu et al., 1995)

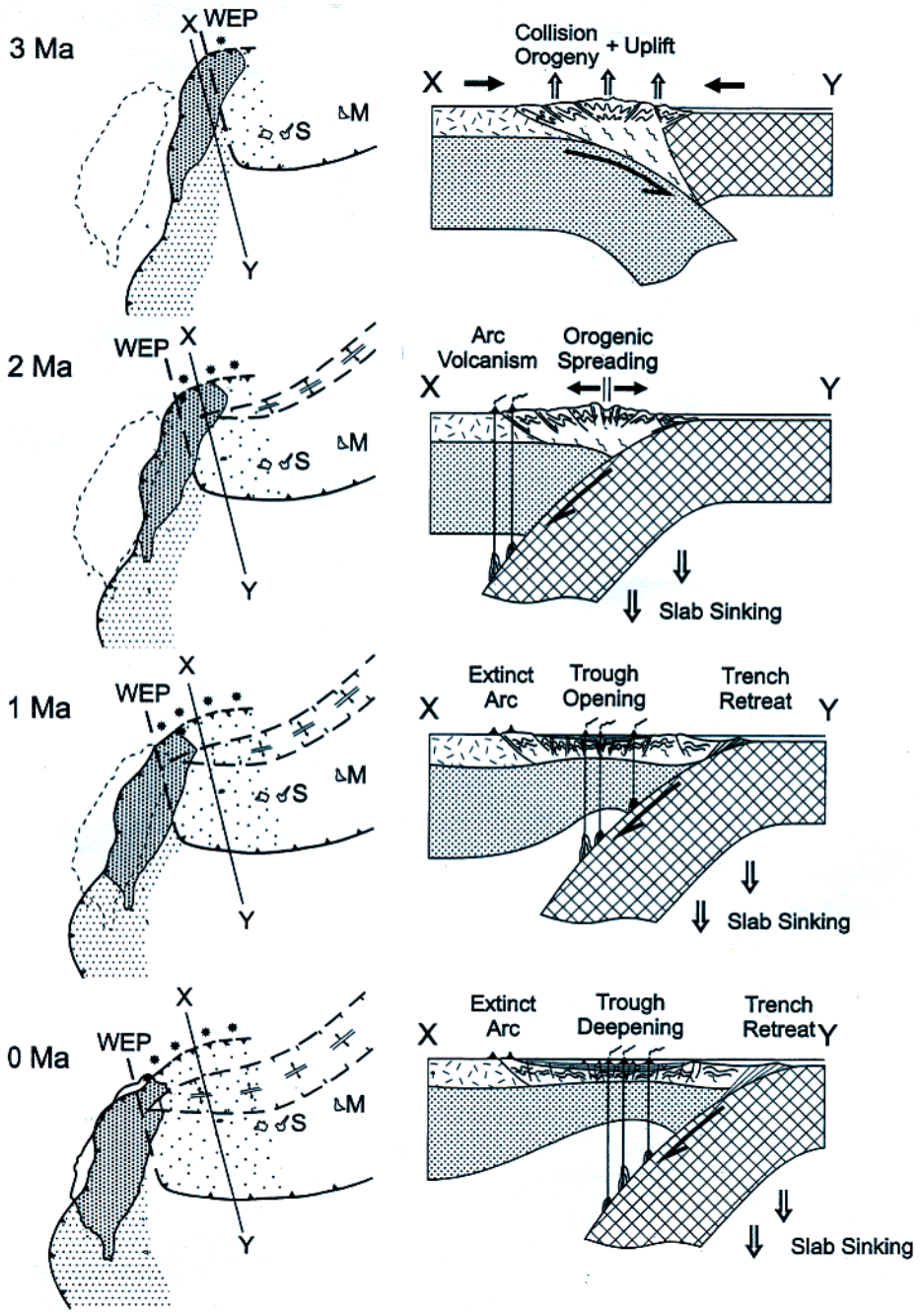

Figure 3. Geodynamic evolution of the southern Ryukyu and the northern Taiwan. Left panels show the plate kinematics of collision and subduction. Right panels are interpreted lithospheric dynamics of section X-Y on the left. (Teng et al., 1996)

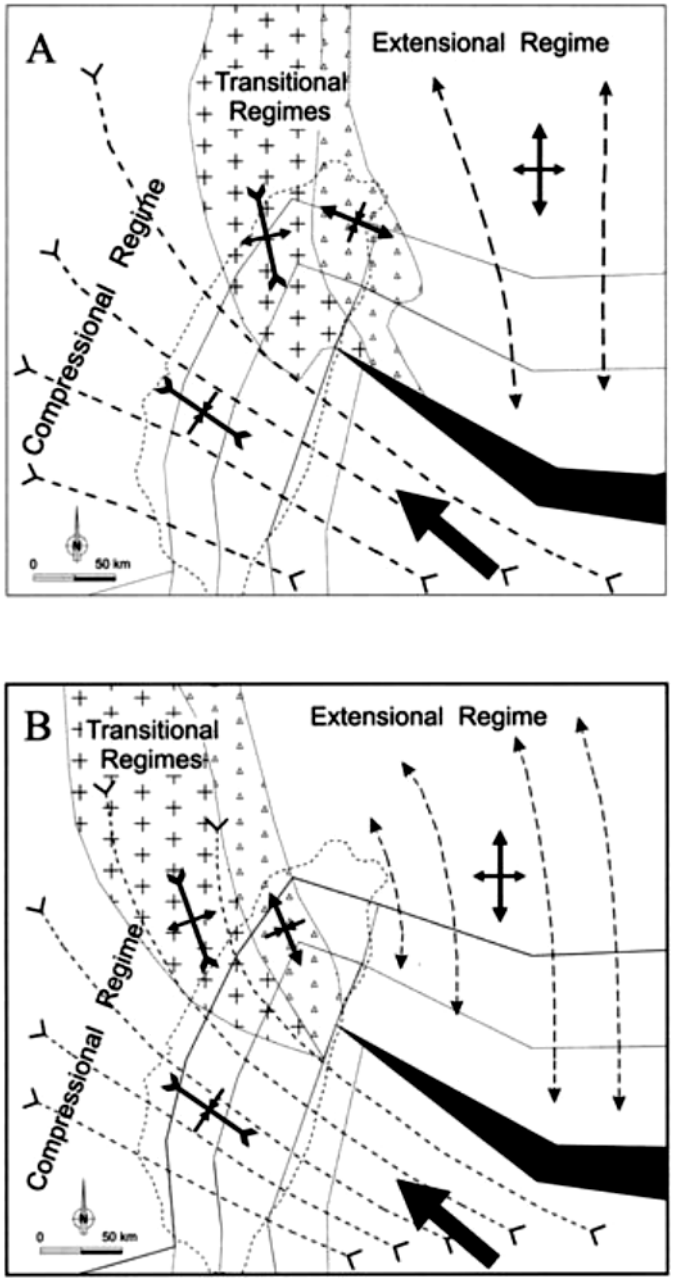

Figure 4. The tectonic regimes with different convergence-trench retreat model. The main difference between Figure 4A and Figure 4B is a westward shift of the transition from compression (Taiwan) to extension (Ryukyu) and it is induced by an increase of velocity of trench retreat southward. (Hu et al., 2002)

2.2 Taipei Basin

2.2.1 Geological Features

The Taipei Basin is a sedimentary basin with triangular shape in the north of Taiwan (Figure 5A & 5B). It is filled with Quaternary sediment and the deepest part of the basin is along the NW border, where the Shanchiao fault (the southern part of the Shanchiao-Chinshan fault systems) is located. Taipei, the capital of Taiwan, is located in the Taipei Basin.

The Taipei Basin is bounded by the TVG in the northern border, frontal foothills of the Taiwan thrust and fold belt in the southeastern side, and the Linkou Tableland in western side. The Shanchiao fault is an active fault and separates the Taipei Basin and the Linkou Tableland (Figure 5A). In addition, there are three known faults — Taipei, Kanchiao and Shanchiao — traverse across the basin. However, the fault systems and features beneath the Taipei Basin are still ambiguous. Among these faults, the Shanchiao fault along the NW border of the basin has a good possibility of being active. Based on the data from several continuous sedimentary profiles along the Shanchiao fault, it reveals evidence for abrupt thickening patterns that roughly implies several prehistoric rapid subsidence events (Huang et al., 2007). But, the remaining lack of the detail historic damaging earthquakes records leads to a poorly characterized earthquake hazard in Taipei Basin.

Although the seismicity in Taipei Basin is relatively low in comparison with the other parts of Taiwan, the thick and soft deposit in Taipei Basin is generally thought as the major factor to cause significant earthquake damage due to site amplification effects (Chen, 2003; Wang et al., 2004; Wang, 2007). Even if the earthquake occurs outside and

far from the basin, the intensity of earthquake motion probably becomes large to induce damage in Taipei Basin. For instance, the Chi-Chi earthquake in 1999, the epicenter about 200 km to the south of Taipei, also caused a building collapsing within the basin.

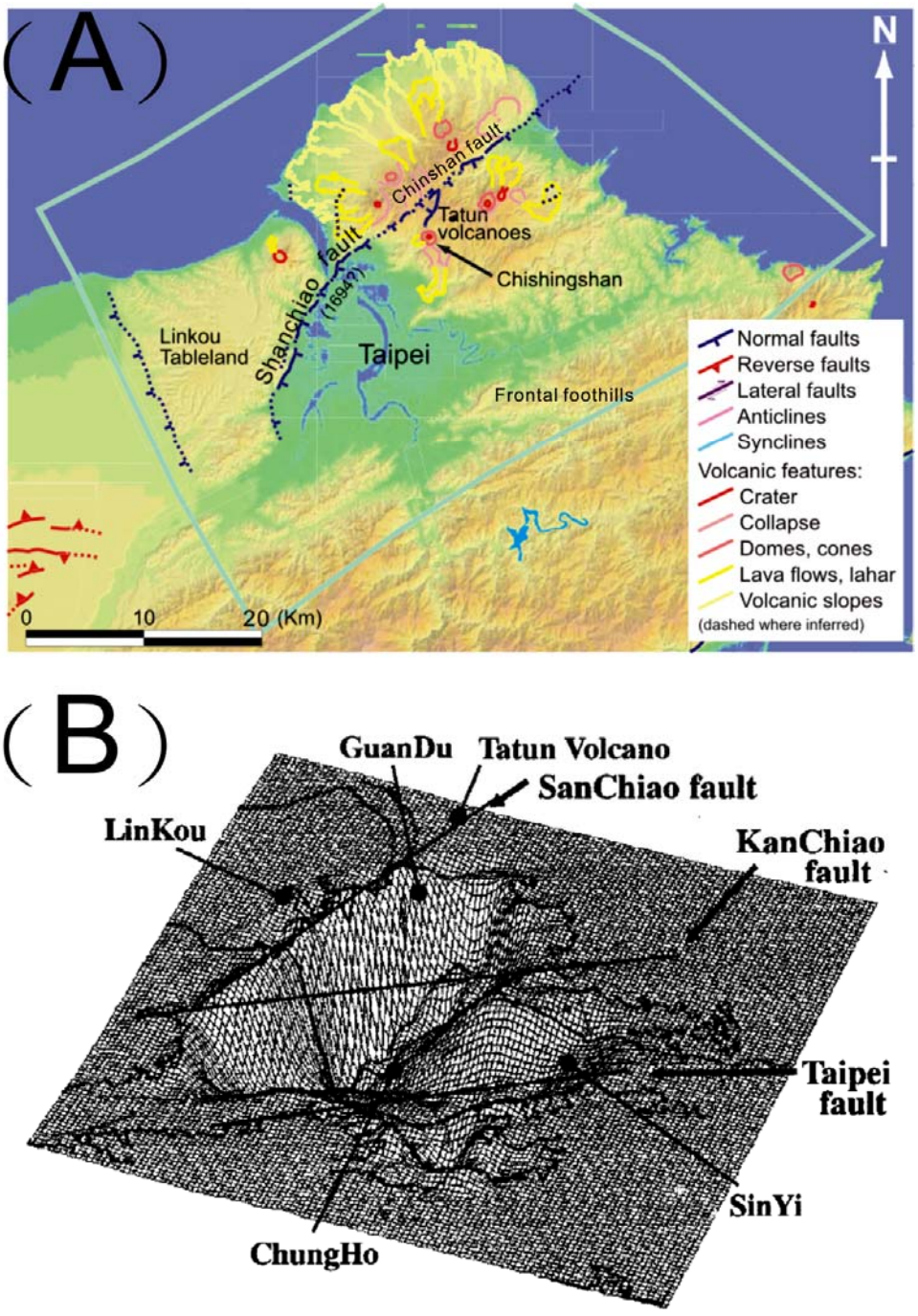

Figure 5. Geological settings of Taipei Basin. (A) Active tectonic map around Taipei region. (Shyu et al., 2005) (B) Shape of Taipei Basin is a half graben. (Wang et al., 2004)

2.2.2 The Formation History

The Taipei Basin is considered to be tectonic structure forming in origin (Ho, 1974). In the beginning collision processes, the three reverse faults — the Hsinchuang fault, the Kanchiao fault and the Taipei fault — were developed in this area from the Pliocene to the Pleistocene age. After that, the north Taiwan was into a tensile environment. It has produced the subsidence along the Shanchiao fault since 800 ka and the tectonic expansion has been thought induced by a pure tension (Teng et al., 2001). Many studies have demonstrated that the Taipei Basin has been created by the movement of Shanchiao fault and the evidences include the results from topography, drilling, shallow seismic reflection studies (Wang et al., 2004; Shyu et al., 2005; Huang et al., 2007). Because of one-side subsidence, it has made the Tertiary basement of the basin in a half-graben shape.

In contrast with the pure tension theory, a pull-apart mechanism model was proposed that the graben structure existed underground due to the segmentation of the block between the branching faults of the basin (Lee et al., 1999). They thought the configuration and deposition of the basin were controlled by the several pre-existing NE-trending thrusts, the relative movement between blocks of fault wedge of the NE-trending thrusts and the kinematic behavior of the crustal block due to the oblique collision.

Yu et al. (1999) carried out GPS surveys over the entire Taipei Basin during 1991 and 1996. They concluded that the Taipei region is in an extension rate of 0.08 ± 0.02 μstrain/yr in the direction of SEE-NWW ($283° \pm 6°$) and the Hsinchuang and Chinshan faults show slightly extensional deformation (Figure 6).

Teng et al. (2004) suggested that the Taipei Basin was a lake from 180 ka to 160 ka.

They examined the boreholes of the Taipei Basin and proposed that the lahars derived from the Tatun volcanoes was responsible for damming the Taipei Basin. The dammed-lake event also demonstrates that the Tatun volcanism is capable of causing catastrophic flooding in the Taipei metropolitan area if the Tanshui River is blocked.

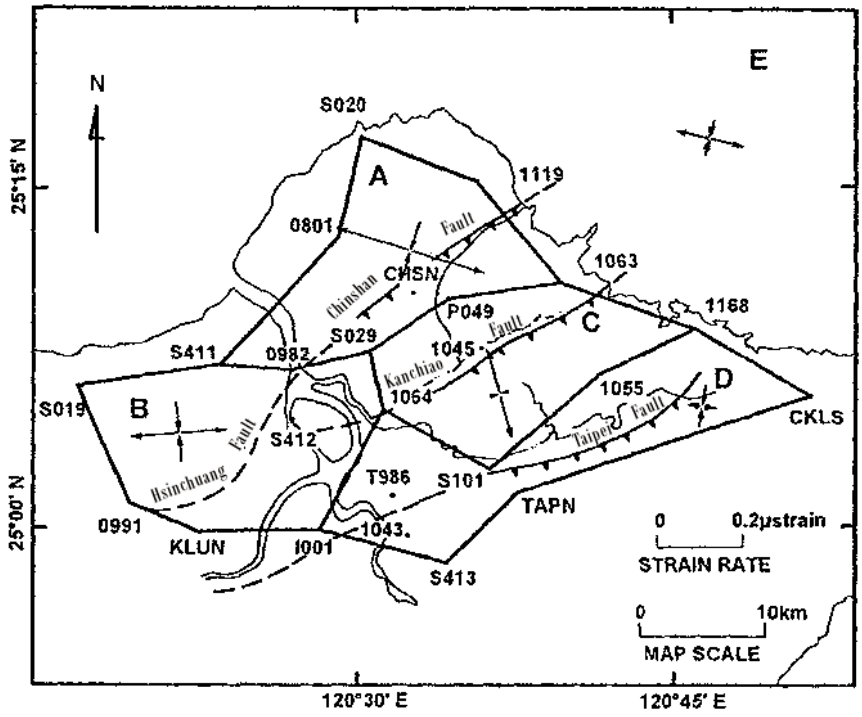

Figure 6. The strain rates around Taipei region. Based on the changes of observed baseline length, the main strain rates of the four sub-networks are shown. (Yu et al., 1999)

2.3 Tatun Volcanic Group

2.3.1 Geological Features

TVG is located adjacent to Taipei Basin and many hot springs, gas fumaroles, and a few micro-earthquakes are observed here. It was built on a late Tertiary sedimentary basement and is enclosed by two faults − the Chinshan (the northern part of the Shanchiao-Chinshan fault systems) and Kanchiao faults. The highest elevation in this

region is 1120 m at the peak of Chishing Mountain. Because of the Armed Forces prohibition, it was not until recently that scientists are permitted to execute detail surveys in TVG. Based on the DTM (Digital Terrain Model) analysis, Yang et al. (2004) identified a total of 10 volcanic craters, 29 volcanic cones, some 40 lava lobes and more than 200 ogives in this region (Figure 8).

TVG consists of a number of Quaternary volcanoes such as Chishing Mountain, Siaoguanyin mountain, Miantian mountain, Shamao mountain, Huangzuei mountain, Jhuzih mountain etc. The volcanic rocks unconformably overlie the Oligocene to Miocene sedimentary rocks. TVG is composed of typical multi-vent volcanoes, predominantly of andesite lavas and pyroclastic flows (Chen et al., 1971). The volcanic rocks occurred as lava flows, pyroclastic breccias, surges, tuffs, lahars and reworked volcaniclastics (Song et al., 2000a, 2000b). Figure 7 shows the simplified geological map of TVG. Moreover, taking into account the deposition of the eruptive products found in the Taipei Basin strata, it appears that the eruptive style of TVG was mainly effusive or silent rather than explosive (Song et al., 2000a).

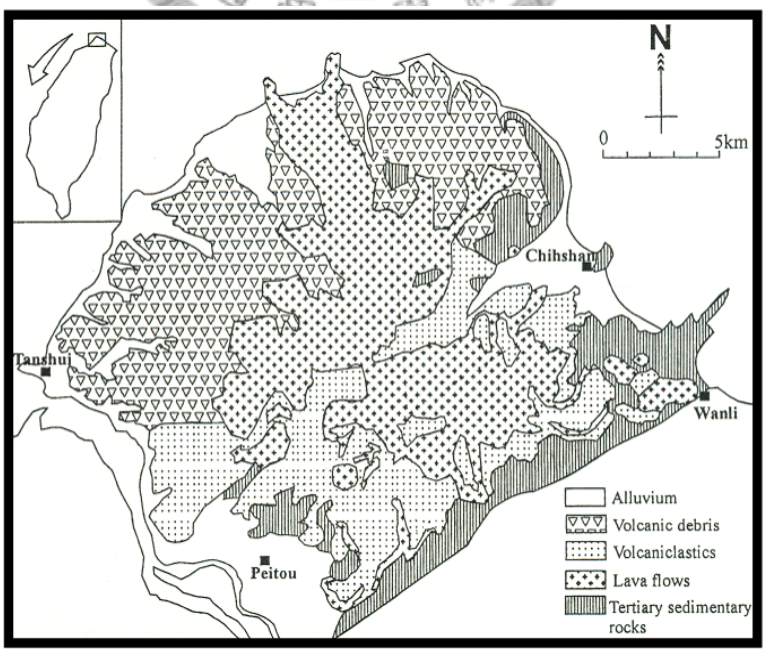

Figure 7. Simplified geological map of TVG. (Song et al. 2000a)

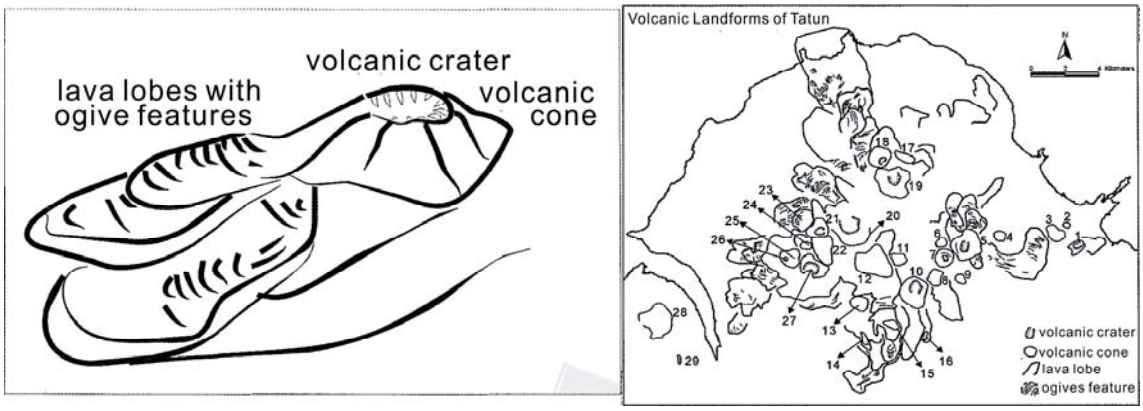

Figure 8. The volcanic characteristics of TVG. Left panel shows the characteristics of volcanic morphology and the right panel presents volcanic geological features of TVG based on DTM analysis. (Yang et al., 2004)

2.3.2 Tectonics Evolution & Eruption History

Although TVG has reposed for a long time, the nearby sediments recorded these episodes of volcanic activity through the deposits from former eruptive products. Judging from the distribution of subsurface strata, intrusive masses and faults, the Chinshan fault was thought to be suitable for upflows of magma (Yeh et al., 1984). The formation of TVG might associate with the PSP subducting beneath the EP. Thus, the TVG has been conventionally ascribed to westward propagation of the Ryukyu volcanic arc (Teng, 1996). However, there are some problems in considering the TVG as part of the Ryukyu volcanic arc. Given an example, there is an apparent discontinuity in geography between the TVG region and the Ryukyu volcanic arc zone.

Wang et al. (1999) argued that the volcanic rocks in TVG area are different from the Ryukyu arc based on trace element analysis. They suggested that it may actually be the result of post-collisional lithospheric extension in the northern Taiwan mountain belt and the mantle source regions involved in the melt generation have been significantly modified by the nearby Ryukyu subduction-related processes. The TVG has been broadly

thought as the southwest part of the Okinawa Trough rather than arc volcanism.

Juang and Bellon (1984) studied the main volcanic activity of the Tatun volcano groups and showed an active age ranging from the late Pliocene to the early or middle Pleistocene. According to radiometric dating analyses and fission track analysis (Juang & Chen, 1989; Wang & Chen, 1990), the volcanic activities can be divided into two periods: it began to erupt during 2.8~2.5 Ma for the first time, and then re-erupted in 1.5 Ma and lasted to 0.2 Ma. Later, based on regional geology, tectonic evolution and borehole data, Song et al. (2000a) proposed an evolution model of volcanism of TVG to explain the surface characteristic features (Figure 9). The model as following:

(1) The eruptions commenced at about 2.8 to 2.5 Ma in a compressional environment and then followed by a long period of volcanic quiescence until around 1.5 Ma.

(2) After that, sparse volcanic activities occurred and produced small amount of lavas still in compressional condition between 1.5 to 0.8 Ma.

(3) During 0.8~0.2 Ma, a large amount of andesitic lavas erupted quickly to form five large composite volcanoes consequent to the tectonic stress environment change from crustal stretching to collapsing.

(4) Finally, the volcanic activity was extinct after 0.2 Ma.

Based on the map of the relationship of lava flows, Chen et al. (2003) reconstructed the Tatun volcanic sequences to 7 lava-units and the lithologic sequences were divided in ascending order into hornblende andesite, hornblende-two pyroxene andesite, two pyroxene-hornblende andesite, two pyroxene andesite, hypersthene-hornblende andesite, olivine-hornblende-pyroxene andesite, and basalt (Figure 10).

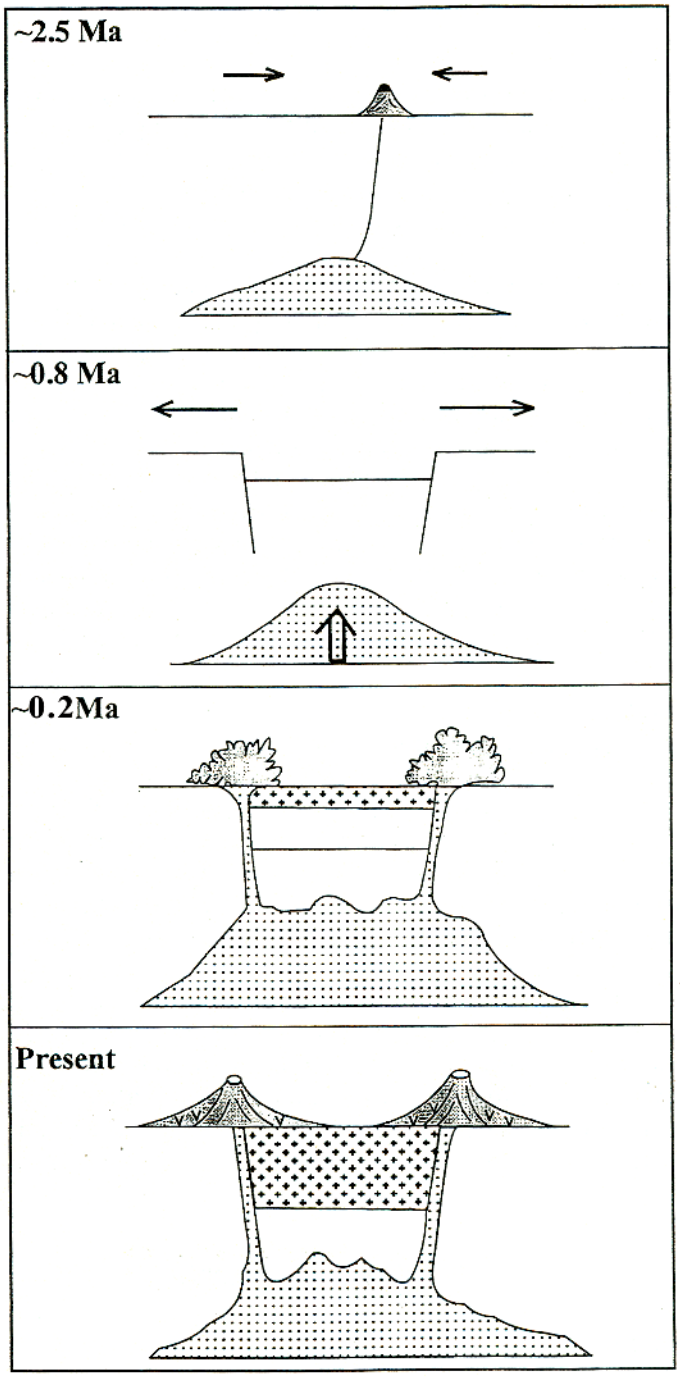

Figure 9. Tectonic and evolutions in the Tatun Volcano Group. (Song et al., 2000a)

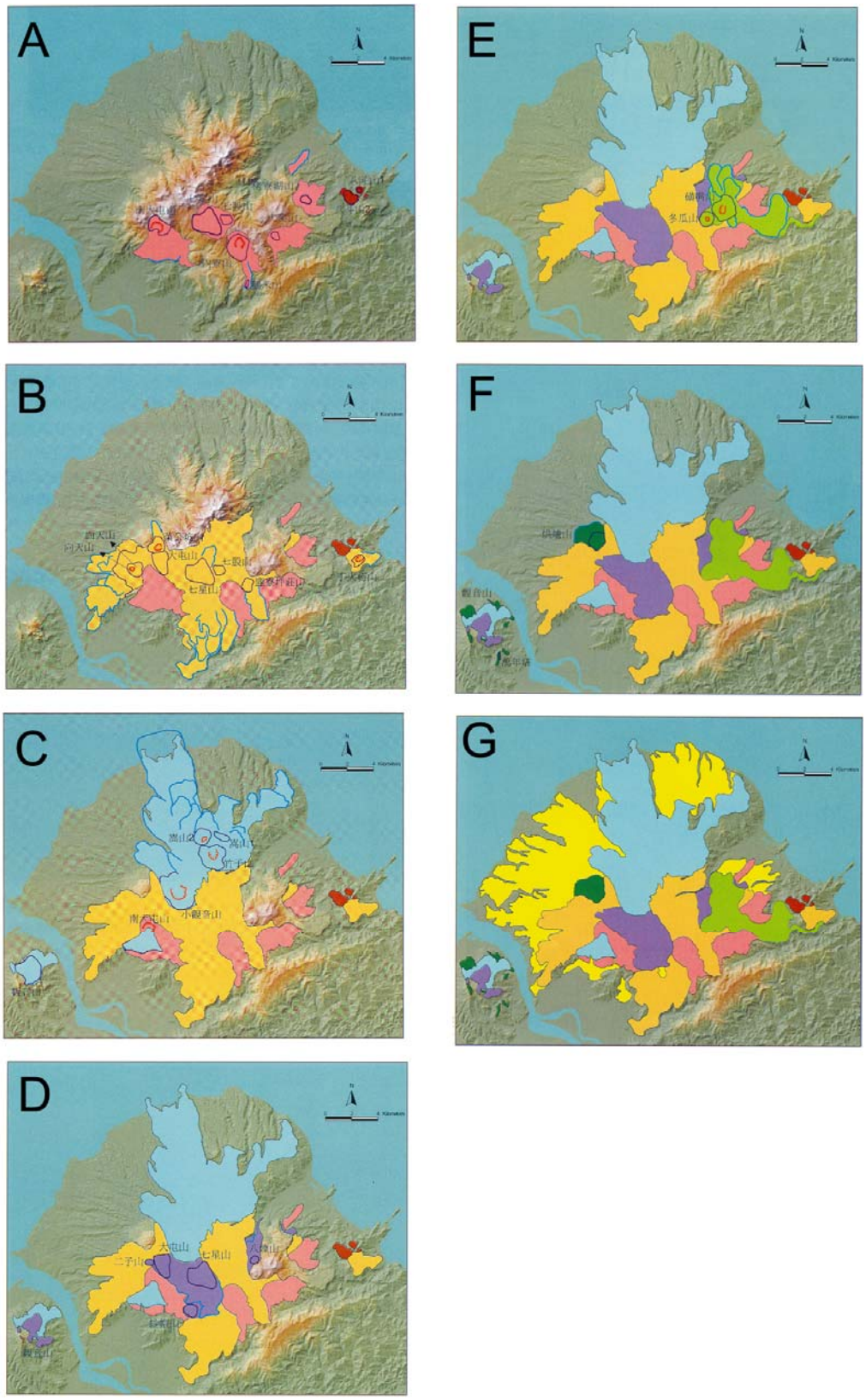

Figure 10. Seven lava-units of TVG. Based on the relationship of lava flows, the Tatun volcanic sequences can be classified into seven lava-units. (Chen et al., 2003)

2.3.3 The Previous Research Review

At 1966, Industrial Technology Research Institute first conducted a series of feasibility studies including geological survey, geochemical and geophysical investigation about geothermal energy in TVG. However, the investigation was terminated later because of the heated water with strong acid erosion.

After that, the Institute of Earth Sciences preparatory office of Academia Sinica was commissioned by the Exploration and Development Research Institute of Chinese Petroleum Corporation to carry out a detail micro-earthquake investigation in 1980. Totally, Yu et al. (1980) deployed 14 temporary seismic stations along the area with significant geothermal features. They monitored the seismic activity during 35 days and recognized 131 micro-earthquakes with maximum magnitude 2.1. According to the result of the micro-earthquake distribution, they found 81% of micro-earthquakes were located shallower than 2 km depth and 95% of micro-earthquakes occurred between 0 – 4 km depth. Based on the surface geothermal characteristic locations and the hypocenter distribution, they proposed that most of the hypocenters were located around and outside the hydrothermal alteration zone, and the strength of the rock below the zone is too weak to sustain the tectonic strain and then resulted in the occurrence of the earthquakes. Moreover, the earthquakes beneath Macao were located shallower than 2 km and it indicated the Wuchihshan formation beneath Macao was relatively broken. In contrast to those in Macao, the earthquakes beneath Chishing Mountain, Shamao and Siaocao mountains were located below 3 km and the focal mechanisms of these earthquakes had considerable difference in strikes and dips. Thus, they speculated these earthquakes might relate to small gravity faults with different strikes and the Chinshan fault might have nothing to do with these earthquakes.

Chen and Yeh (1991) used data from gravity and micro-earthquake surveys to examine the relationship between the earthquakes, Chinshan fault and the geothermal activities in this area. Twenty-one composite fault plane solutions from their results indicated that most of the focal mechanisms were normal fault type and might corresponding to the geothermal activities of Chishing Mountain or Tatun volcanoes. Yang et al. (1994) stood on the analysis of the gravity and magnetic anomalous distribution to interpret the subsurface structures and concluded the local high gravity zone with a low magnetic anomaly could be the result of hydrothermal alternation beneath the Chishing mountain region.

In addition, the measurement of the $^{3}He/^{4}He$ isotope ratio from fumarolic gas showed that more than 60% of helium composition exhibit mantle-derived characteristics and imply a deep magmatic source might still exist beneath TVG region (Yang et al., 1999) (Figure 11).

More recently, numerous earthquakes with peculiar waveforms unnoticed and not reported in the Central Weather Bureau (CWB) catalog have been identified (Kim et al., 2005a; Lin et al., 2005a; Lin et al., 2005b). These newly identified earthquakes showed similarities in waveforms, arrival time differences and occasionally occurred in a very short period as swarms. Furthermore, some signals were recorded as volcano-tectonic earthquakes such as harmonic signals, tornillos, spasmodic bursts and signals with complex coda (Lin et al., 2005a). Kim et al. (2005a) suggested that these earthquake clusters are most probably associated with hydrothermal/magmatic activities in a back-arc extensional environment and the significantly high b-value (1.22) for the Tatun volcano area compared with entire Taiwan indicated that the crust is weak and cannot sustain high strain levels. From the whole Taiwan island seismic tomographic studying, it reveals that there is an anomalous region of low *Vp* and high *Vp/Vs* ratio at depth from 6

to 10 km beneath the Tatun volcano, and it is an indication of possible partial molten materials or magma reservoir (Kim et al., 2005b). Konstantinou et al. (2007) proposed a possible configuration of the volcano-hydrothermal system beneath the Chishing mountain surrounding area as Figure 12 derived from the geothermal structures, waveform analyses and the depth of seismogenesis ceases. Besides, Lee et al. (2008) analyzed the gas compositions of fumaroles with time and proposed two possible processes to explain the temporal variations. They suggest that a magma chamber might exist beneath the TVG area, particularly in the area of Tayukeng (Figure 13).

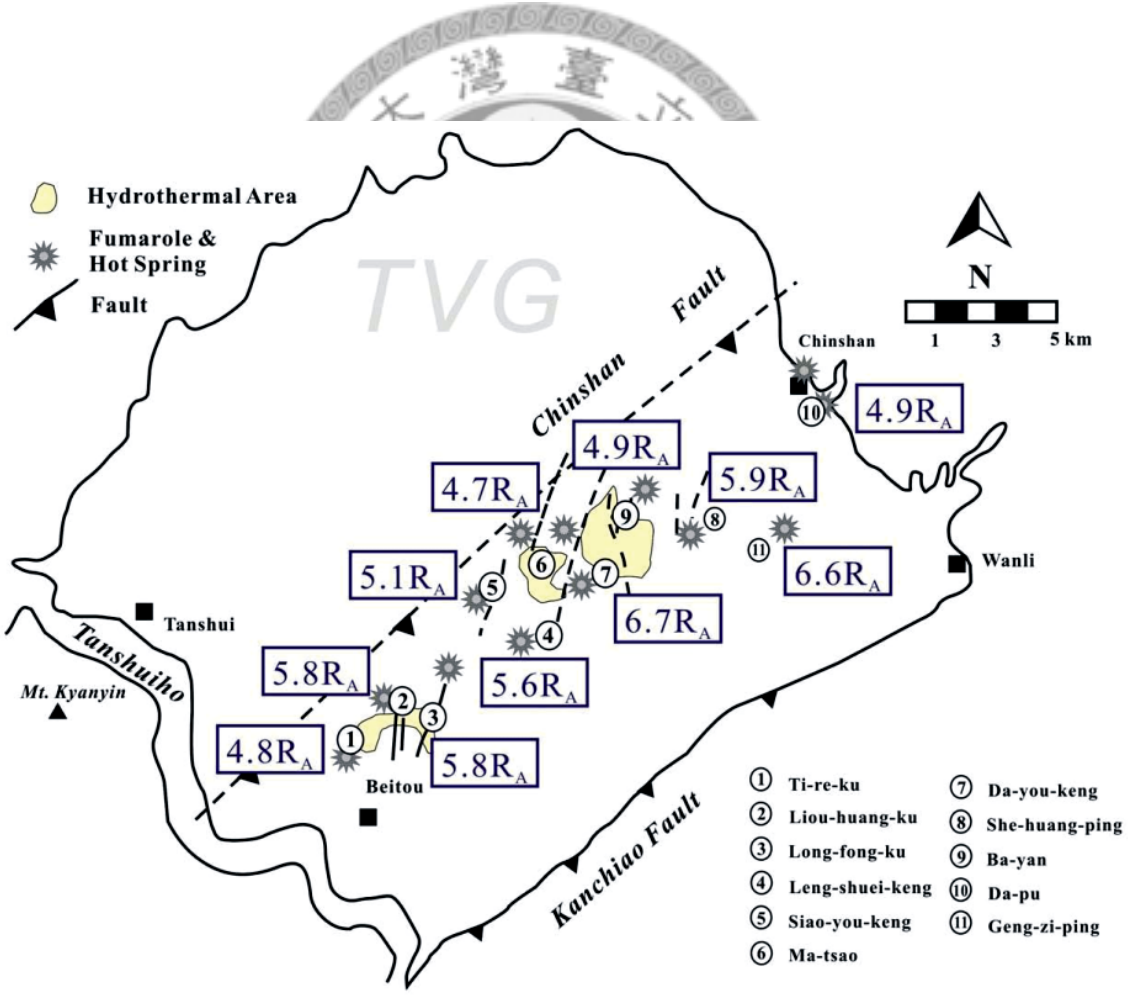

Figure 11. Distribution of $^{3}He/^{4}He$ ratio of the TVG. (Yang et al., 2003; Lee et al., 2008)

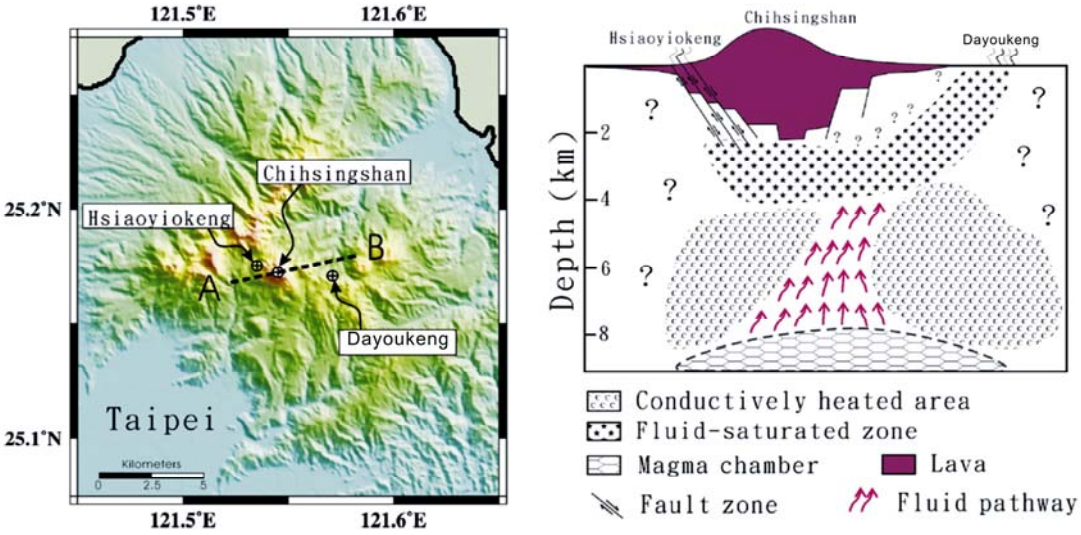

Figure 12. The possible hydrothermal system beneath TVG. Right panel shows the possible hydrothermal system beneath the cross-section AB in left panel. (Konstantinou et al. 2007)

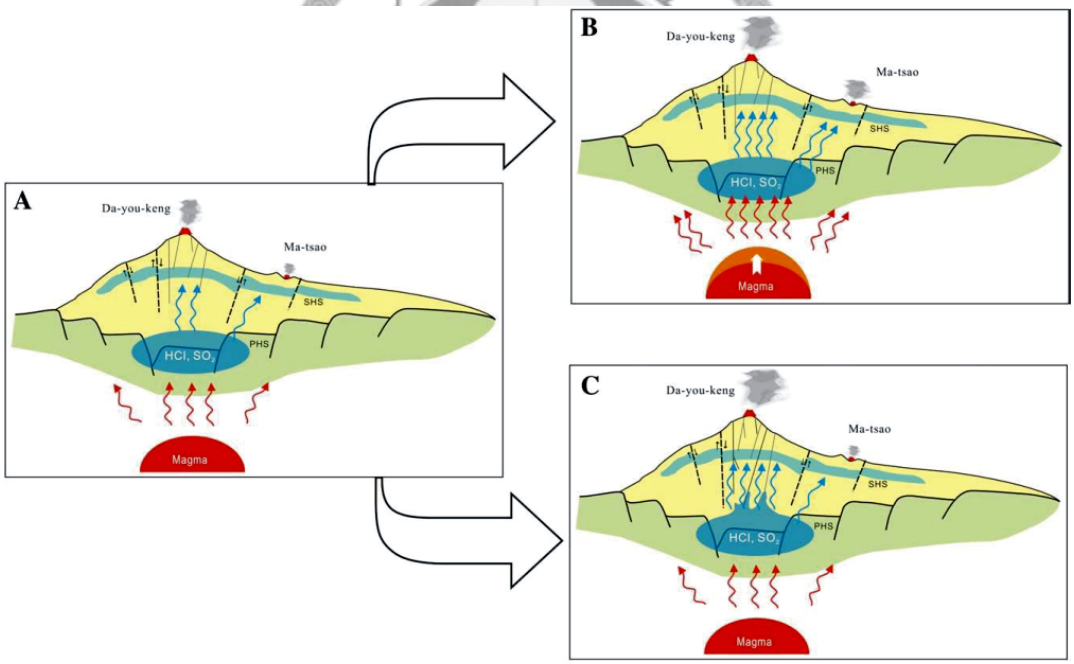

Figure 13. The possible processes of the gas compositions in TVG. According to the possible state of the hydrothermal system in left panel, two possible processes in right panels are proposed to explain the temporal observations of gas compositions. Figure B presents more magmatic fluids were released from the ascending magma, but the Figure C shows that more magmatic fluids were released from the fractures. (Lee et al., 2008)

Chapter 3 Data

Seismicity in Taipei surrounding region is fairly low and the distribution of permanent stations conducted by Seismological Observation Center of the Central Weather Bureau (CWB) around TVG is not dense enough (Figure 14) for the purpose of this study. In order to increase the ray-path coverage entire the studying region, data from four different seismic networks were used in this study. These four seismic networks included two local temporary seismic networks located in Taipei and Tatun region, the Central Weather Bureau Seismic Network (CWBSN) and the Taiwan Strong Motion Instrumentation Program (TSMIP). The improvement of the ray-path coverage will be helpful to enhance the resolution of tomographic image.

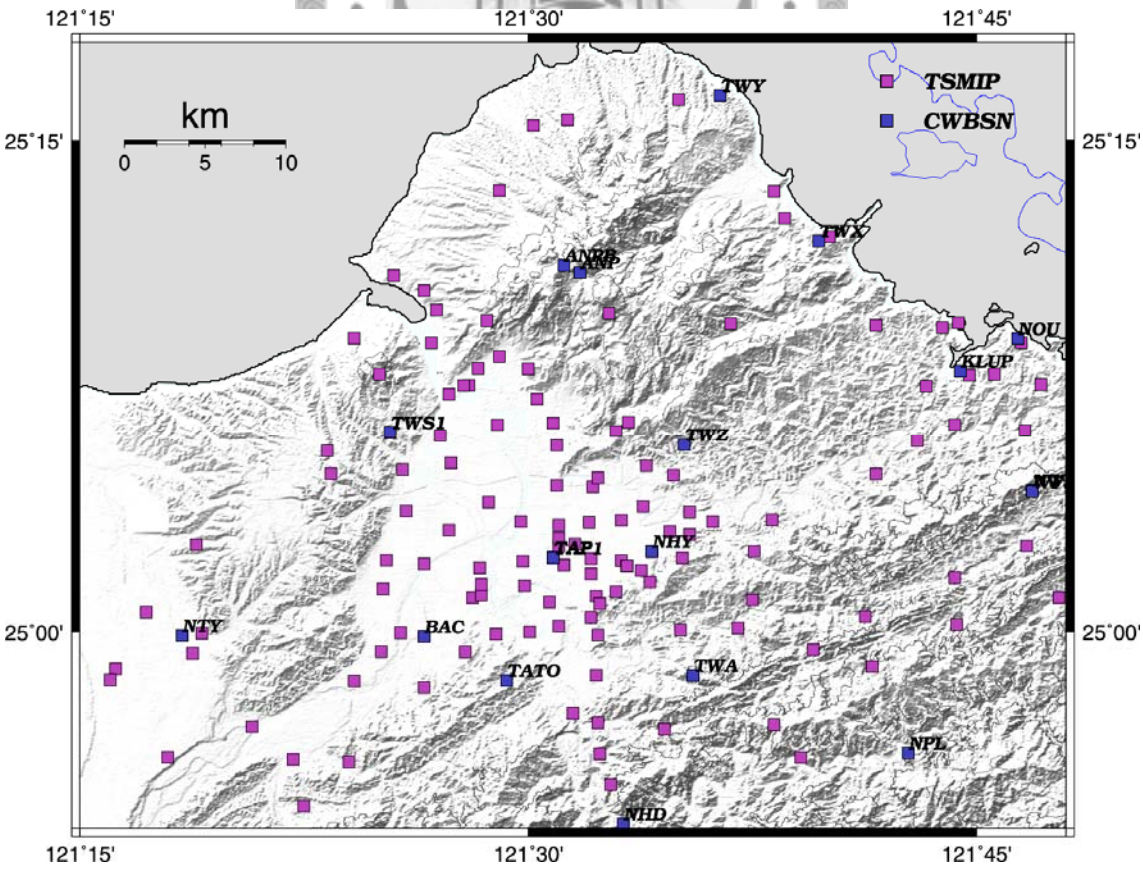

Figure 14. Station distribution of the TSMIP and CWBSN around northern Taiwan.

3.1 National Permanent Seismic Networks

Taiwan Central Weather Bureau Seismic Network (CWBSN) has 71 stations around whole Taiwan now. The CWBSN is responsible for monitoring regional earthquakes and the real-time digital recording has begun since 1991. The stations are equipped with 3-component S13 velocity sensors and the earthquake is detected automatically by the network system followed by manual verification.

The TSMIP, consisted of 680 digital accelerographs in free-field sites was established since 1991. The main purpose of TSMIP is to study the characteristics of ground motion in different geological conditions and the response of various types of man-made structures. All stations are equipped with the triaxial force-balance accelerometers and most of the stations were installed in the metropolitan areas. Apart from the sparsely populated and high-mountain areas, the TSMIP stations have achieved an average station spacing of 5 km kilometers. Not all of the TSMIP stations equip Global Position System (GPS) timing system. However, S-P times from the TSMIP stations could be used for earthquake location and *Vp*/*Vs* structures determination. (Chang, 2004; Wu et al., 2007)

3.2 Small Seismic Monitoring at TVG

One of the temporary seismic networks is installed around TVG and designed to monitor the micro-earthquakes. It is a small-aperture seismic network (Figure 15). The seismic observation has been carried out since May 2003 and this project was funded by the National Research Council of Taiwan and the Yangminshan National Park during the past few years. The Institute of Earth Sciences, Academia Sinica (IES) has been in charge of site selection for the seismic network, installation, instrument maintenance, data

collection, and analysis. The signal is continuously recorded. Instruments equip with three-component short period or broadband sensor and absolute timing is automatically provided by GPS system. Each of the seismic stations is constructed on a concrete-platform and was completely covered with Fiber Reinforce Plastic (FRP).

The first five seismic stations (YM01 – YM05) were distributed around the Chishing Mountain volcanic cone where the micro-earthquakes were clustered. After that, the other stations were installed in the nearby area of Tayukeng where most of the present hydrothermal activity is observed. Up to now, this array is composed of 12 seismic stations (Figure 15; Table 1).

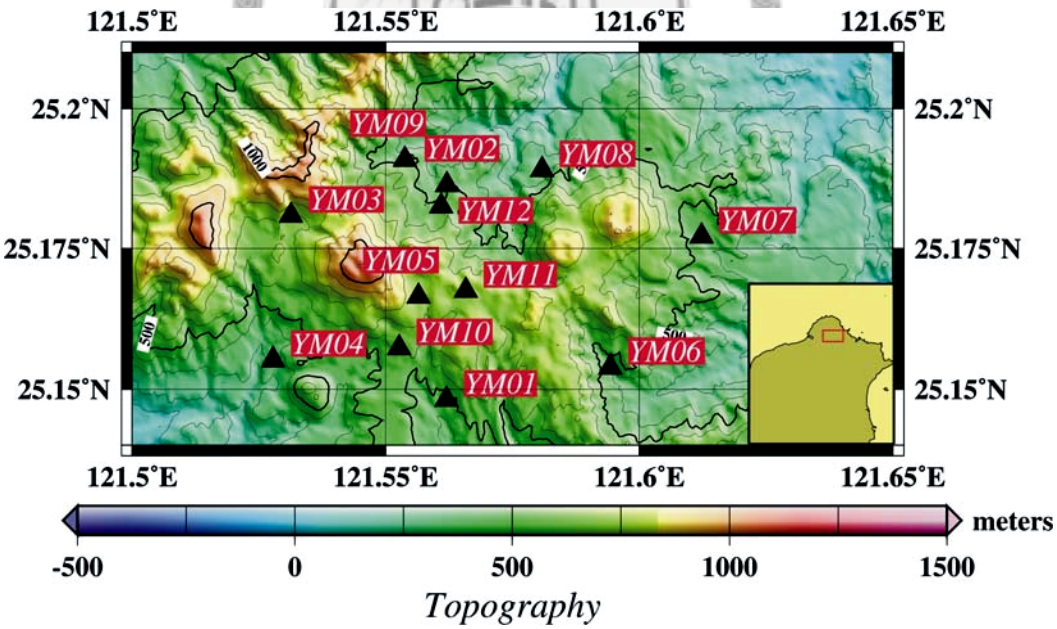

Figure 15. The station distribution of small seismic monitoring at TVG. (Lin and Pu, 2007).

Table 1. Stations parameters in TVG project.

Tatun Seismic Array List				
Station Name	**Longitude(E)**	**Latitude(N)**	**Altitude(m)**	**Start Time**
YM01	121.5620	25.1482	488	2003/05/13
YM02	121.5621	25.1863	521	2003/05/13
YM03	121.5314	25.1809	702	2003/05/18
YM04	121.5278	25.1552	401	2003/05/16
YM05	121.5564	25.1665	740	2003/06/02
YM06	121.5943	25.1538	445	2003/09/09
YM07	121.6123	25.1771	456	2003/09/09
YM08	121.5808	25.1890	342	2003/09/08
YM09	121.5538	25.1909	519	2006/01/10
YM10	121.5526	25.1573	622	2006/04/03
YM11	121.5658	25.1675	772	2006/06/07
YM12	121.5609	25.1826	555	2006/06/07

3.3 Seismic Network in Metropolitan Taipei

The IES was a contractor of the Central Geological Survey to execute a four years (2004 - 2007) project of 「Geophysical investigation and monitoring for micro-earthquake in metropolitan Taipei」. The purpose of this project is to install the down-holes and surface seismic stations to observe the seismicity of active faults surrounding Taipei area and the volcanic activity of the northern Taiwan. Each surface station is equipped with a three-components broadband seismometer.

In 2004, the stations were installed along the Shanchiao fault at the both sides (Figure 16, Table 2). Then, in 2005, a newly seismic network was deployed and the stations were widely installed in the whole Taipei Basin (Figure 16, Table 3). Based on the seismic observation during the previous two years, they placed some seismic stations in the peripheries of the Taipei Basin and in the north of TVG during 2006 to improve the monitoring ability of the networks (Figure 16, Table 3). Up to now, the purpose of this project has accomplished and some stations have been moved away.

The final station and epicenter distribution around entire study region are shown in Figure 17.

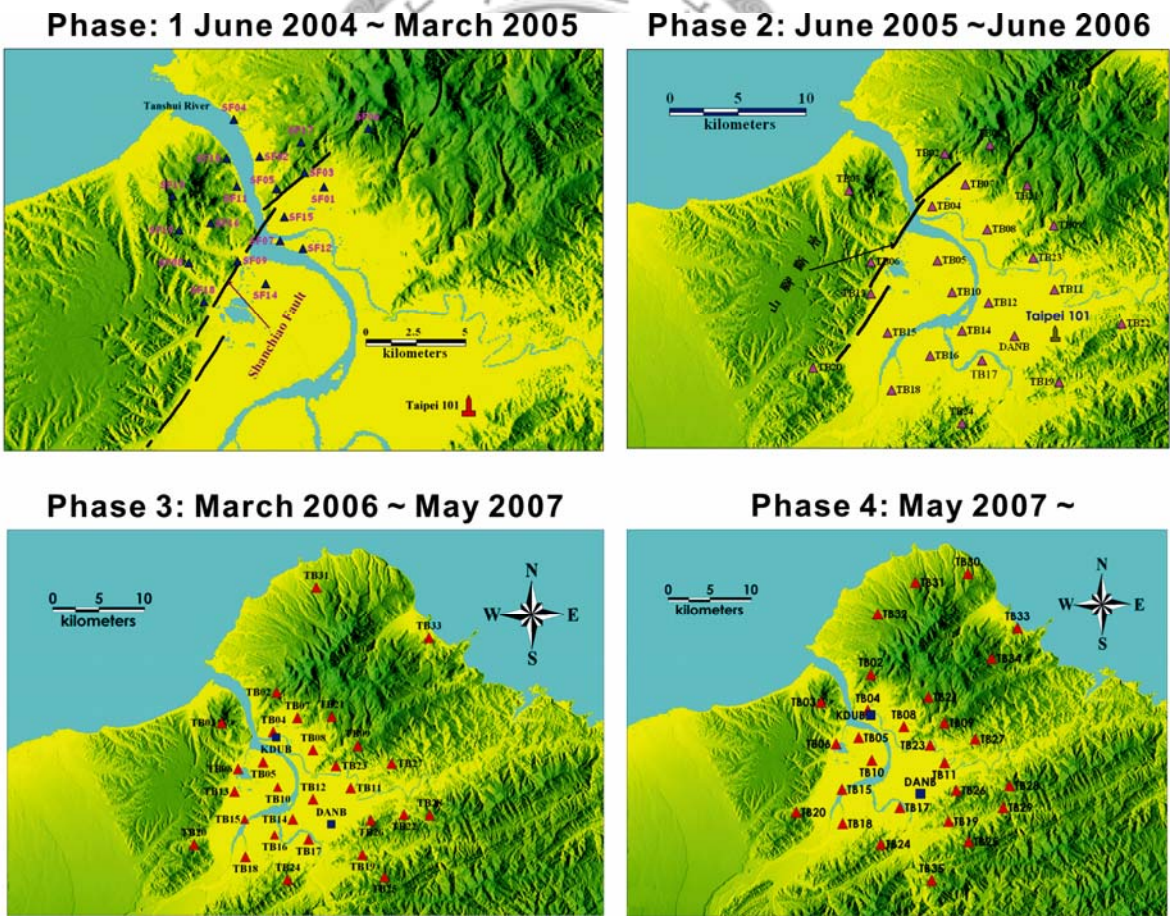

Figure 16. The station distribution of seismic network in metropolitan Taipei. (Huang, 2008)

Table 2. Stations parameters in Taipei Basin project during Phase 1.

Station Name	Sensor	Recorder	Longitude(E)	Latitude(N)	Start Time
SF01	KS-2000	DL-24	121.4930	25.1334	2004/06/21
SF02	KS-2000	DL-24	121.4604	25.1473	2004/06/15
SF03	KS-2000	DL-24	121.4833	25.1394	2004/06/14
SF04	KS-2000	DL-24	121.4489	25.1647	2004/06/10
SF05	KS-2000	DL-24	121.4636	25.1556	2004/06/14
SF06	KS-2000	DL-24	121.5111	25.1485	2004/06/24
SF07	KS-2000	DL-24	121.4629	25.1101	2004/06/23
SF08	KS-2000	DL-24	121.4234	25.1014	2004/06/07
SF09	KS-2000	DL-24	121.4489	25.0998	2004/06/28
SF10	KS-2000	DL-24	121.4458	25.146	2004/06/16
SF11	KS-2000	DL-24	121.4482	25.1354	2004/06/16
SF12	KS-2000	Q330	121.4743	25.1073	2004/06/18
SF13	KS-2000	DL-24	121.4175	25.1289	2004/06/25
SF14	KS-2000	DL-24	121.4681	25.0905	2004/06/11
SF15	KS-2000	DL-24	121.4644	25.1192	2004/07/30
SF16	KS-2000	DL-24	121.4285	25.1191	2004/08/13
SF17	KS-2000	DL-24	121.4759	25.1555	2004/10/08
SF18	KS-2000	DL-24	121.4295	25.0822	2004/09/15
SF19	KS-2000	Q330	121.4240	25.1119	2004/08/11
SF20	LE-3D	801H	121.5161	25.1514	2004/06/01
SF21	STS-2	Q680	121.5202	25.1865	2004/06/01

SF22	CMG3T	KS54000	121.4881	24.9754	2004/08/11

Table 3. Stations parameters in Taipei Basin project during Phase 2~4.

Station Name	Sensor	Recorder	Longitude(E)	Latitude(N)	Start Time
TB01	KS-2000	DL-24	121.5111	25.1485	2004/06/25
TB02	KS-2000	DL-24	121.4759	25.1555	2004/10/08
TB03	KS-2000	DL-24	121.4175	25.1289	2004/06/25
TB04	KS-2000	DL-24	121.4644	25.1192	2004/07/30
TB05	KS-2000	DL-24	121.4618	25.0905	2005/06/25
TB06	KS-2000	DL-24	121.4352	25.0837	2005/06/25
TB07	KS-2000	DL-24	121.4913	25.1353	2005/06/30
TB08	KS-2000	DL-24	121.5070	25.1054	2005/08/12
TB09	KS-2000	DL-24	121.5555	25.1079	2005/06/25
TB10	KS-2000	DL-24	121.4813	25.0633	2005/06/29
TB11	KS-2000	DL-24	121.5562	25.0648	2005/06/29
	GMG40	801H			2006/04/10
TB12	KS-2000	DL-24	121.5078	25.0563	2005/06/29
	GMG40	801H			2006/04/07
TB13	KS-2000	DL-24	121.4232	25.0628	2005/07/05
	GMG40	801H			2006/03/21
TB14	KS-2000	DL-24	121.4885	25.0373	2005/06/27
	GMG40	801H			2006/05/25
TB15	KS-2000	DL-24	121.4342	25.0362	2005/07/01
TB16	KS-2000	DL-24	121.4652	25.0203	2005/06/27
TB17	KS-2000	DL-24	121.5027	25.0170	2005/06/27

TB18	KS-2000	DL-24	121.4367	24.9975	2005/06/28

Table 4. Stations parameters in Taipei Basin project during Phase 2~4. (continued)

Station Name	Sensor	Recorder	Longitude(E)	Latitude(N)	Start Time
TB19	KS-2000	DL-24	121.5592	25.0023	2005/07/04
TB20	KS-2000	DL-24	121.3790	25.0127	2005/06/28
TB21	Trillium	Q330	121.5363	25.1346	2005/08/18
TB22	GMG40	801H	121.6050	25.0417	2005/06/25
	KS-2000	DL-24			2006/03/28
TB23	Trillium	Q330	121.5405	25.1188	2005/08/19
TB24	KS54000	Q680	121.4971	24.9735	2004/08/11
TB25	KS-2000	DL-24	121.5840	24.9797	2006/01/29
TB26	KS-2000	DL-24	121.5695	25.0351	2006/08/08
TB27	KS-2000	DL-24	121.5920	25.0892	2006/03/29
TB28	KS-2000	DL-24	121.6343	25.0391	2006/05/26
TB31	Trillium	Q330	121.5202	25.2614	2006/05/08
TB33	Trillium	Q330	121.6412	25.2112	2006/05/17
DANB	VSE355GR	Q330	121.5268	25.0355	2005/10/08
GDUB	VSE355GR	Q330	121.4684	25.1165	2006/11/03

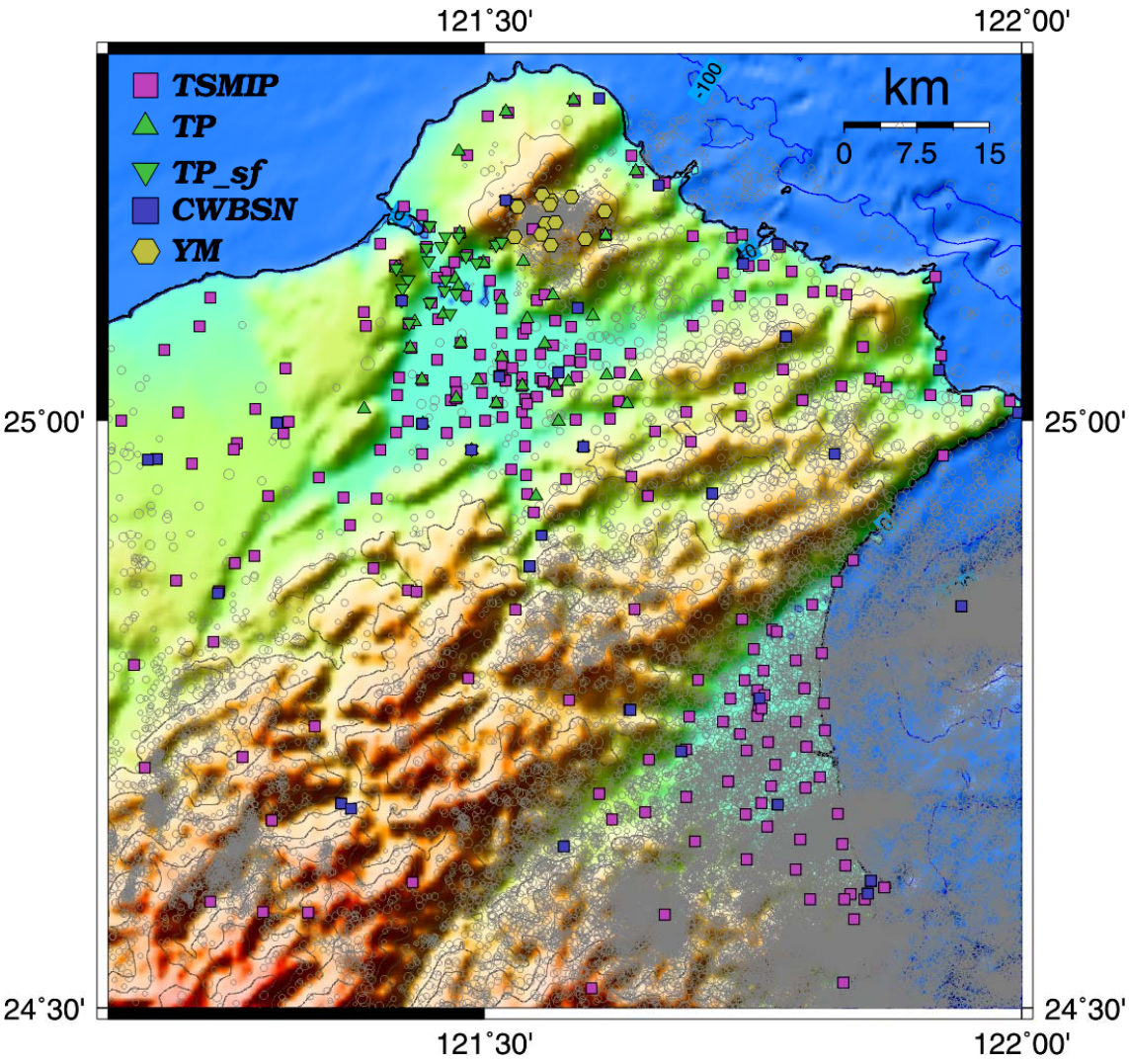

Figure 17. The earthquake location and stations distribution. The whole area is the inversion region and the gray hollow circle represents epicenter.

Chapter 4 Theory and Method

In order to understand the Earth internal properties and further analyze the seismogenic structures, the seismic tomography, also named seismic image, is a methodology to simulate the material properties such as seismic wave propagating velocities and Poisson's ratio. The modern excavation technique only can excavate several kilometers into the earth and the high heat and pressure felt at these depths prevents humans from going much deeper, so the seismic tomography is a widespread method to depict the underground structures up to several hundred kilometers (Thurber & Atre, 1995; Kurashimo & Hirata, 2004; Dias et al., 2007; Wu et al., 2007; Clifford et al., 2008; Matsubara et al., 2008). Especially, in order to understand the magma chamber with particular seismic wave velocity properties, the seismic tomography method also extensively applies to the volcanic region (Patane et al., 2002; Lees, 2007).

A well seismic three-dimension model can be used for accurate earthquake location. Furthermore, some interesting relationships can be found between the geological and tectonic setting, the earthquakes distribution and the tomography image (Natale et al., 2004; Tahara et al., 2008). The velocity model results are also combined with other geophysical and geological information to infer the geological structures. For instance, the role of that in controlling the seismic coupling and the rupture nucleation of large earthquakes has been discussed (Husen et al., 2000; Zhao et al., 2007).

4.1 Local Earthquake Tomography

When earthquake occurs, the seismic energy is emitted out and penetrates the

mediums to the surface. It is a good way for seismologists to analyze the intervening structure and components based on its travel time from the hypocenter to the seismic station (Figure 18). But, because of the uneven distribution of earthquakes, the observations of human-made explosions sometimes are carried out to increase the data set.

Tele-seismic three-dimensional velocity inversion, continental reflection profiling and local earthquake tomography are the three seismological techniques to demonstrate the structural heterogeneity of the crust and upper mantle. However, for tele-seismic method, because of the low frequency content and the narrow angle of incidence of the rays in one location, the resolution of near-surface structure will remain poor. So, the local and regional tomography has become a powerful tool to investigate the structural heterogeneity of the crustal-scale. Because of the higher frequency content of local earthquake seismograms and the presence of the earthquake sources within the model volume, the local earthquake tomography method has the potential for higher-resolution imaging of shallow structure.

Since the theory was first proposed (Aki & Lee, 1976), the approach, theoretical method and its application have been modified and have greatly advanced (Thurber & Aki, 1987; Um & Thurber, 1987; Thurber & Eberhart-Phillips, 1999; Lin et al., 2007; Zhao et al., 2007). First of all, an initial model is often assumed first and then compare the difference between predicted and observed arrivals to reconstruct the velocity distribution in the real earth. But, it is never completely recovered. Tomographic inversion should always be seen as lower bounds on the levels of perturbations in the real earth because of its several inherently constraints (Lees, 2007). The most important thing to keep in mind is the method of seismic tomography applies to the solid Earth is a nonlinear process (Pavlis & Booker, 1983). The paths of the seismic rays from the source

to the receivers depend on the model parameters such as velocity that are being sought. So, it is a coupled hypocenter-velocity model problem. Thus, some approximate assumptions and linearized methods are applied into the inversion procedures (Aki & Lee, 1976; Nolet, 1978; Edi Kissling, 1988). In this study, the VELEST and SIMUL2000 program were used to establish one-dimension (1-D) and three-dimension (3-D) model, respectively. The 1-D model determined by the VELEST is taken as the initial input model for the SIMUL2000 to calculate the 3-D velocity models.

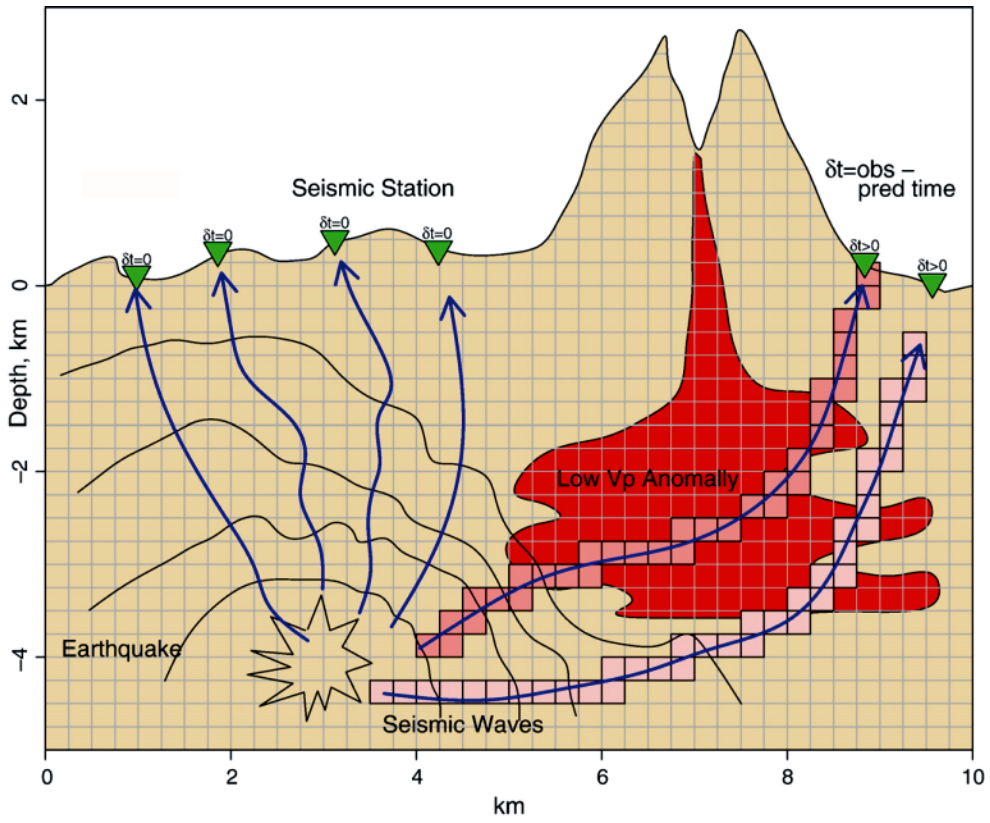

Figure 18. The concept of tomography method. The cartoon shows relationships between the earthquake, ray-paths and stations used for a 3-D tomographic inversion. The travel-time difference can be projected back along the ray-path (Lees, 2007).

4.2 The Minimum 1-D Velocity Model

The result of the seismic image of the three-dimensional inversion is deeply affected

by the initial reference model. Kissling et al. (1994) pointed out that using an inappropriate initial reference model may not only affect the quality of the 3-D image by introducing artifacts but also influence the confidence calculations by underestimating the uncertainties of the result (Figure 19). Thus, they proposed a 1-D tomographic solution called the "minimum 1-D model" to overcome these problems (Kissling, 1988; Kissling et al., 1994). The "minimum 1-D model" is thought as a well-suited 1-D velocity model for earthquake location and for 3-D seismic tomography. In this study, a "minimum 1-D model" determined by the Fortran computer program named VELEST with version 3.3 and its algorithm was proposed by Kissling (1995).

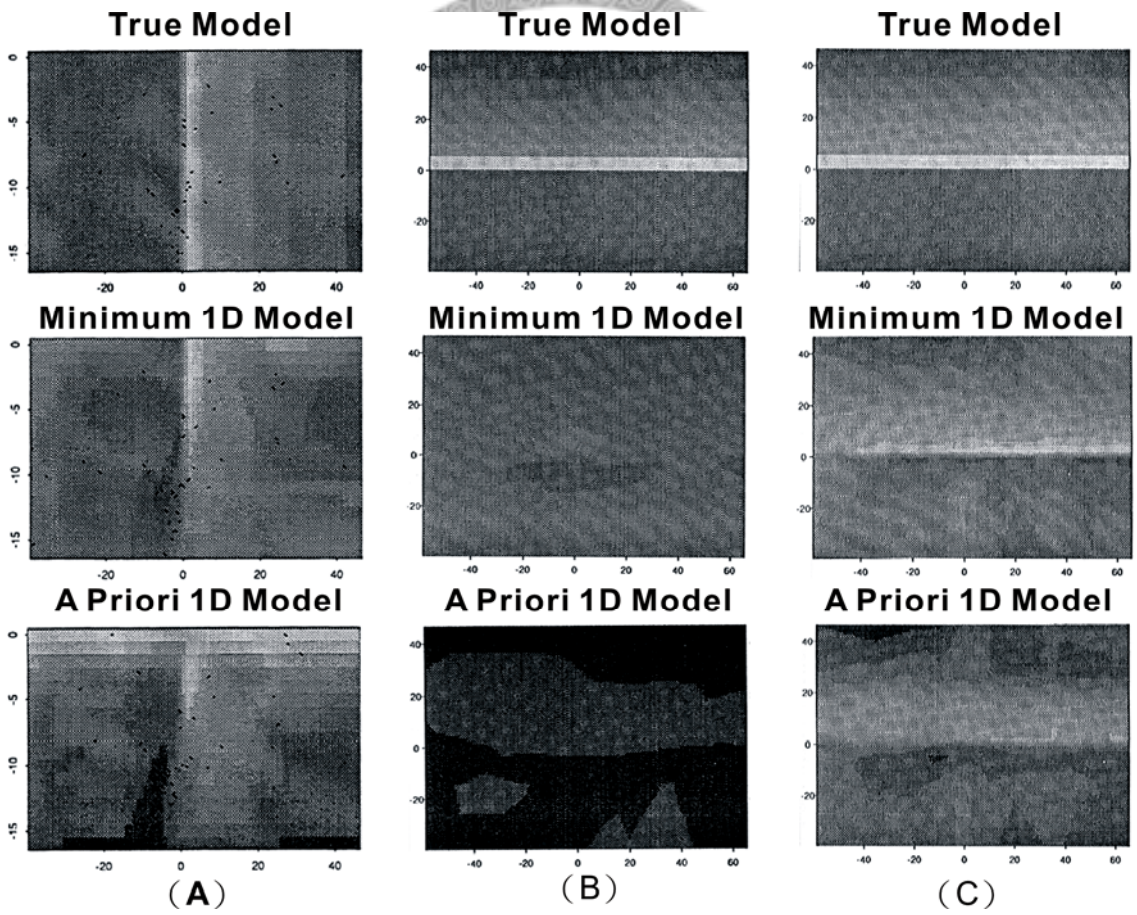

Figure 19. The 3-D images with different initial 1-D model. The 3-D image obtained with the minimum 1-D model is much closer to the true model than that obtained with a priori 1-D model. (Kissling et al., 1994)

4.2.1 Hypothesis and Inversion Method

The VELEST program is a FORTRAN77 routine that has been designed to derive 1-D velocity model. It was modified, implemented some methods and tested several times since 1976 (Kissling, 1995). Now, it can be used to simultaneously invert a large number of earthquake travel time data for hypocentral and velocity model parameters — P- and S-wave velocities. Because this inversion is a non-linear problem, the solution is obtained iteratively. One-iteration consists of solving both the forward and inverse problem once. The briefly procedures as following flow chart:

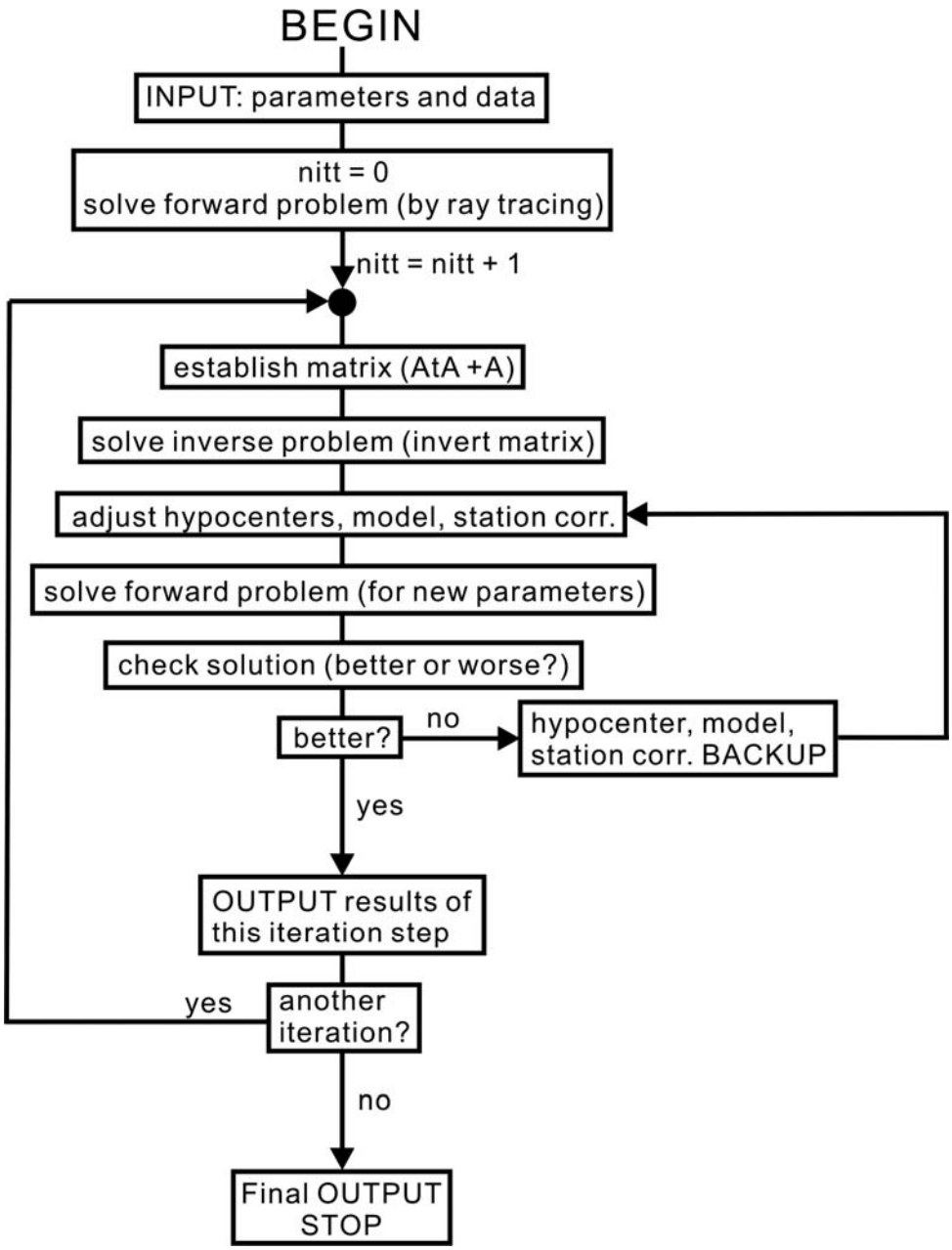

Figure 20. The procedure flow chart of minimum 1-D model. (Kissling, 1995)

4.2.1.1 Travel Time of a Single Ray

The travel time between a seismic source and a receiver for a given velocity model with ray-tracing is a forward problem. And, the arrival times of seismic waves generated by an earthquake and observed at the seismic stations are a function of the hypocentral parameters and the velocity model:

$$t = F(t_0, x_0, y_0, z_0, V(x, y, z))$$

t	arrival time
t_0	origin time
x_0, y_0, z_0	coordinates of hypocenter
$V(x, y, z)$	velocity model

Consequently, the residual travel time is a function of the differences between the estimated and the true hypocentral and velocity parameters:

$$t_{res} = t_{obs} - t_{calc} = F(dt_0, dx_0, dy_0, dz_0, dV(x, y, z))$$

Applying a first-order Taylor series expansion to the equation, a linear relationship between the residual travel time and adjustments to the hypocentral and velocity parameter is obtained:

$$t_{res} = t_{obs} - t_{calc} = \sum_{j=1,4} \frac{\delta F}{\delta h_j} \bullet \Delta h_j + \sum_{k=1,n} \frac{\delta F}{\delta m_k} \bullet \Delta m_k$$

t_{res}	travel time residual
m_k	the estimated velocity parameter, is $V(x, y, z)$
$\frac{\delta F}{\delta h_j}$	partial derivative of travel time with respect to *j*th hypocentral parameter
$\frac{\delta F}{\delta m_k}$	partial derivative of travel time with respect to *k*th velocity model parameter

This formula contains forward problem and inverse problem.

4.2.1.2 Coupled Hypocenter Velocity Model Problem

The determination of the unknown hypocentral parameters and the velocity parameters from a set of arrival time is a coupled hypocenter-velocity-parameter problem:

$$t_i = \frac{\delta F}{\delta t} \bullet \Delta t_0 + \frac{\delta F}{\delta x} \bullet \Delta x_0 + \frac{\delta F}{\delta y} \bullet \Delta y_0 + \frac{\delta F}{\delta z} \bullet \Delta z_0 + \sum_{k=1,n} \frac{\delta F}{\delta m_k} \bullet \Delta m_k$$

t_i	the ith travel time residual
n	the total number of observations for this event

Continuously, the formula is written in matrix notation and separated into two matrices representing the hypocentral and the velocity model parameters. And it was added by an error vector that contains remaining part of the travel time residual. The remaining part is what cannot be explained by adjustments to the unknown parameters. The relation can be written as follows:

$$t = Hh + Mm + e = Ad + e$$

t	vector of travel time residuals
H	matrix of partial derivatives of travel time with respect to hypocentral parameters
h	vector of hypocentral parameter adjustments
M	matrix of partial derivatives of travel time with respect to model parameters
m	vector of model parameter adjustments
e	vector of travel time errors
A	matrix of all partial derivatives
d	vector of hypocentral and model parameter adjustments

And the method used for the formula is solved by full inversion of the damped least squares matrix.

Although the VELEST algorithm can simultaneously invert P- and S-wave arrival times for 1-D P- and S-wave velocity models. In this study, 1-D P-wave velocity model was the only one to be determined by the VELEST algorithm. Then, the Wadati-diagram was applied to get the *Vp/Vs* ratio in the target area, and the 1-D S-wave velocity model could be obtained. The procedures to obtain a “minimum 1-D P-wave model” followed

the guidelines proposed by Kissling et al. (1994). The brief guidelines for a minimum 1-D model as following:

Step 1. Establishing the "a Priori 1-D Model" based on the previous study

Step 2. Establishing the Geometry and the Velocity Intervals of Potential 1-D Model

Step 3. Relocation and Final Selection of Events

Step 4. Calculation of Minimum 1-D Model

4.3 3-D Image Tomography

Traditionally, seismic arrival times are used to produce a velocity model, especially the arrival time data of body waves. *Vp* and *Vs* are modeled from P and S arrivals, respectively. Thurber (1993) proposed an approach for *Vp/Vs* ratio from t_s-t_p. In this study, computer algorithms (SIMUL2000) developed by Thurber (1983, 1993) and Eberhart-Phillips (1990) (documentation provided by Evans et al. (1994)).

4.3.1 Hypothesis and Inversion Method

The SIMUL2000 program is a damped-least-squares and full matrix inversion intended for using with natural local earthquakes, with or without shots and blasts. The iterative damped-least-squares method is applied to obtain a solution for the 3-D structures of *Vp* and *Vp*/*Vs* ratio, and simultaneously achieves new hypocenter solutions.

P arrivals and S-P times were used in this study. The conceptual approach parallels that of Aki and Lee (1976) and the velocity of the medium is parameterized by assigning at a large number of discrete points in three dimensions. The velocity at a given point is determined by interpolation among the surrounding grid points.

Usually, the problem is formulated as over-determined. So, the damped-least-squares solution to the linearized problem is obtained from

$$m = (M^T M + L)^{-1} M^T t$$

m	vector of model perturbations
t	vector of travel time residuals
L	diagonal matrix of damping parameter
M	matrix of partial derivatives

Among these parameters, the matrix M is constructed according to the parameter separation techniques of Pavlis and Booker (1980). After the equation is solved, the velocity parameter changes are applied to the model and the earthquakes are individually relocated in the new model. The simultaneous inversion is repeated iteratively and the F test (DeGroot, 1975) is used to select a stopping point for the procedure.

This method uses the pseudo-bending ray-tracing algorithm (Um and Thurber, 1987) to find the rays and calculates the travel times between the events and seismic stations. The algorithm utilizes direct minimization of the travel time: an initial path estimate is perturbed by using a geometric interpretation of the ray equations, and the travel time along the path is minimized in a piecewise fashion. The perturbation is iteratively performed until the travel time converges.

4.3.2 Grid Method

There are many strategies to set the model values within a model such as regular node, block spacing, non-regular block sizes and variable-sized tetrahedral model elements. In traditional local earthquake tomography research, the regular node has been in widespread use. However, the highly irregular source distribution and non-uniformly spaced stations are always the major puzzles in inversion research. If one might wish to have localized area of denser model gridding, the denser gridding must

extend across the full grid in regular gridding approach. (Figure 21B). Eberhart-Phillips et al. (1995) shows that solving for a coarse node-grid prior to a fine node-grid typically gives much more accurate results. Thus, Thurber and Eberhart-Phillips (1999) proposed an alternative 'flexible' gridding strategy combing regular gridding with fixed-node capability to adjust the inversion grid to the target dataset (Figure 21C). Flexible gridding inversion permits the use of denser grid in localized area and grid nodes to be linked where sampling is sparse. Besides, Flexible gridding strategy also can be used after an inversion with regular gridding is completed, because the result of a preliminary inversion with relatively uniform grid spacing can be treated as the master node sets. Meanwhile, the areas with highest and lowest resolution can be identified.

In this study, the flexible gridding method was adopted in during 3-D tomography inversion. After a minimum 1-D P-wave velocity model was obtained, the minimum 1-D model was used as the starting model for the coarse 3D velocity inversions. Since the preliminary inversion result is the coarse node-grid inversion. Then, more nodes in the interested region-TVG and the Taipei Basin area were added for the fine node-grid inversion. The nodes outside the target region was set linear link to one of neighboring nodes. The intervals of inversion grid points for the whole coarse node-grid inversion were 5 km (Figure 22A) and that for the fine node-grid were 2.5 km in the interesting regions (Figure 22B).

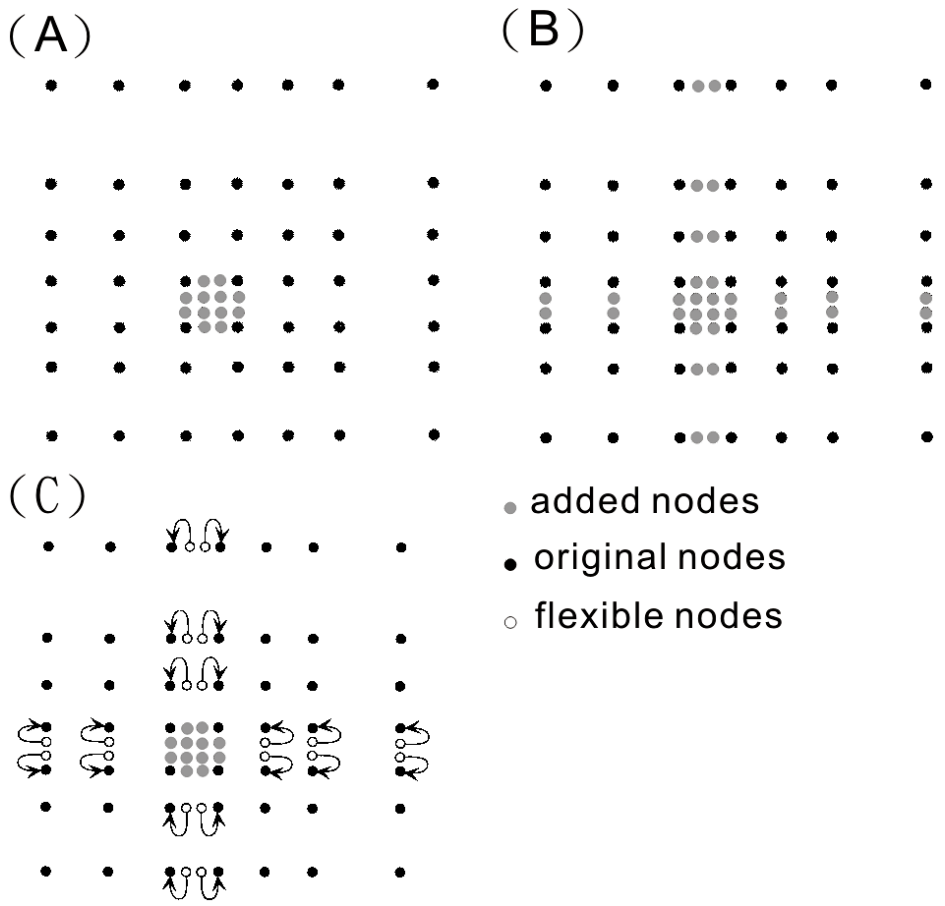

Figure 21. Gridding approach. When one might wish to have localized area of denser model gridding such as Figure A, the denser gridding must extend across full grid in regular gridding approach (Figure B). The flexible gridding can be introduced in localized area (gray circles) and the values of nodes extending away from target area (open circles) can be linked (arrows) to values at adjacent nodes (black circles) (Figure C). (Thurber and Eberhart-Phillips, 1999)

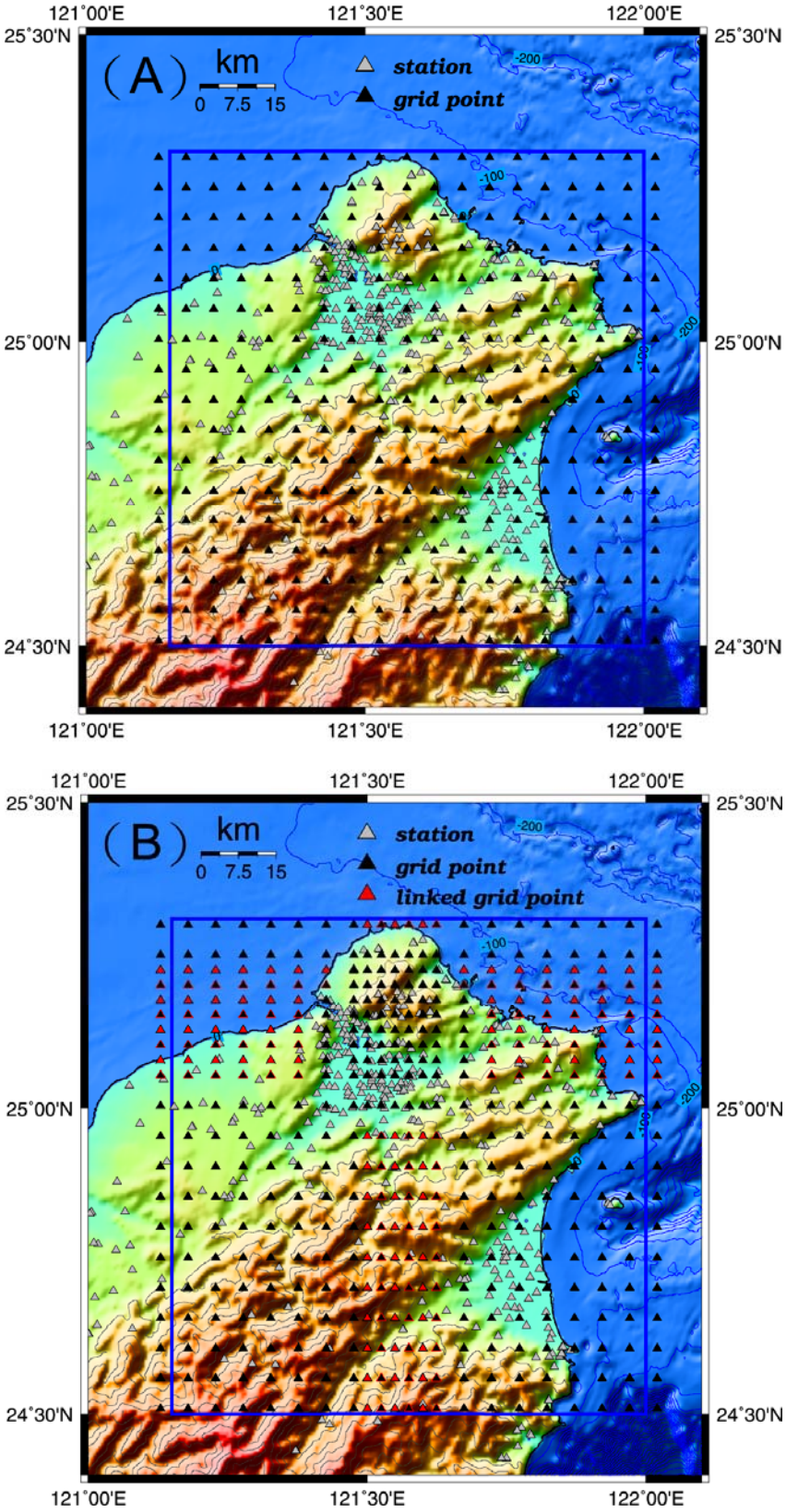

Figure 22. Gridding distribution in inversion. The coarse (Figure A) and finer (Figure B) gridding distribution during 3-D tomographic inversion in distribution during 3-D tomographic inversion in this study.

4.3.3 Damping Parameters

Damping is introduced to efficiently handle the underdetermined part of the inversion problem (Nolet, 1978, 1987). Traditionally, the appropriate damping parameters are determined on the basis of a trade-off curve between data variance and model variance (Eberhart-Philips, 1990). It is chosen empirically by running a series of single-iteration inversions with a large range of damping values and the trade-off curve is a concave, roughly hyperbolic curve. The proper damping is a value that is a good compromise between a large data variance (too smooth a model) and a large model variance (too complex and fitting to noise in the data). If below some damping value, the modeling results start to wander away from this simple hyperbola, it indicates that the inversion is not behaving linearly and must be chosen somewhat above that damping value.

In order to choose an optimal damping parameters for *Vp* and *Vp*/*Vs* ratio, in this study, *Vp* was chosen with a trade-off curve with holding *Vp*/*Vs* damping fixed at a large value—800 to reduce the effect of the S-P data as small as possible. Then, *Vp*/*Vs* damping was obtained as 150 while keeping *Vp* damping as the optimal parameter—200 chosen in the previous step (Figure 23).

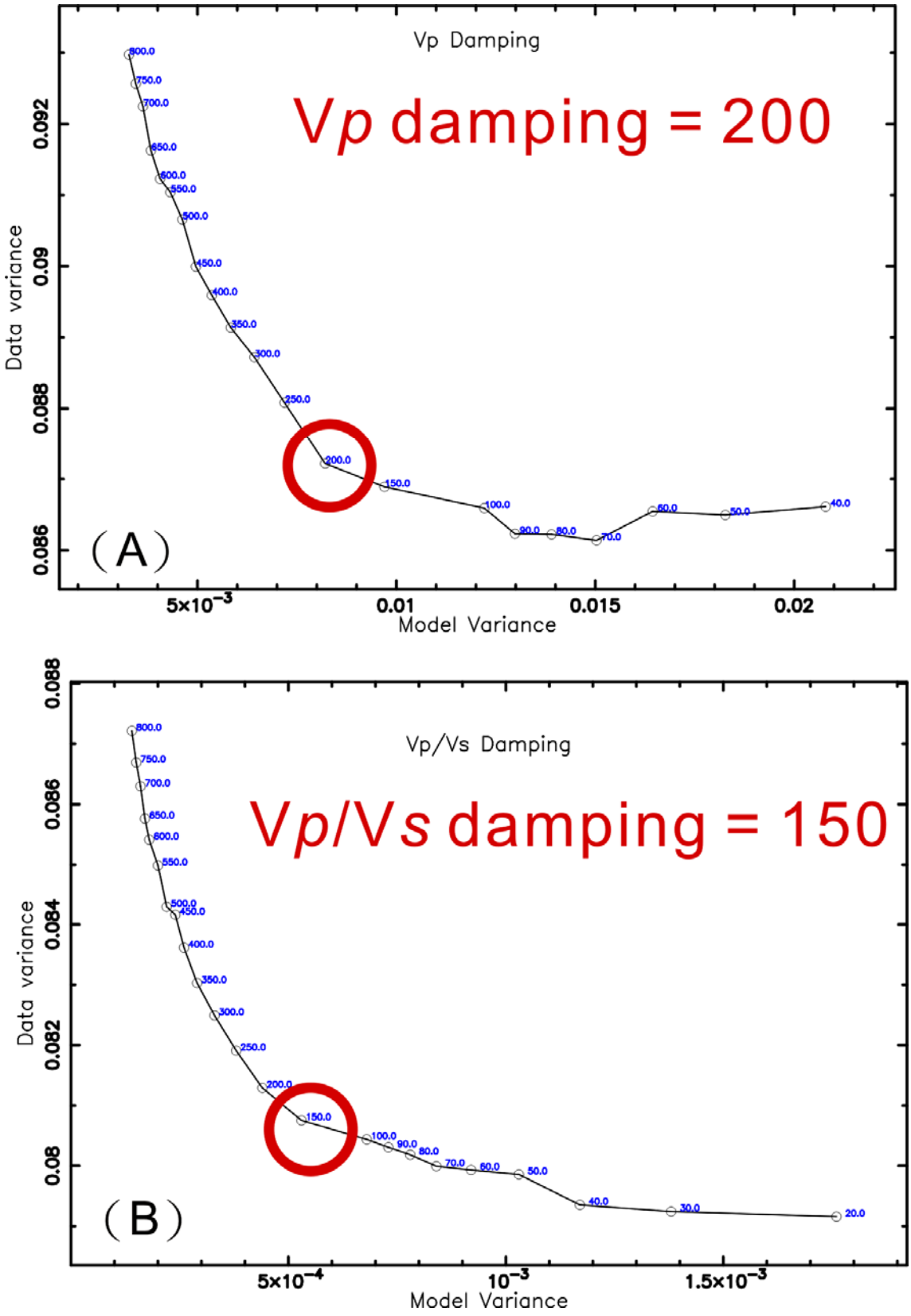

Figure 23. The trade-off curve of choosing *Vp* and *Vp*/*Vs* damping values.

4.3.4 Resolution Test

4.3.4.1 Checkerboard Resolution Test

The basic idea of the checkerboard resolution test (CRT) was given by Humphreys and Clayton (1988) and has been applied by Grand (1987) and Inoue et al. (1990). The test has been used widely to evaluate the resolution of the solution. Thus, the steps of CRT method as followings:

(1) Make a checkerboard — First step is to assign the positive and negative velocity perturbations to the 3-D blocks of a homogeneous velocity model at the same interval.

(2) Calculate a set of synthetic travel times — Then, a set of travel time delays that result from tracing rays through the synthetic structure is calculated.

(3) Invert again — Finally, invert those delays as if they are real data and then compared the synthetic inversion result with the initial synthetic structure. The resolution of the solution is judged by examining whether the solution after inversion is returned to the checkerboard or not.

4.3.4.2 Restoring Resolution Test

In order to check the reliability of the tomographic solution, Restoring Resolution Test (RRT; Zhao et al., 1992) was carried in this study. The RRT is used to examine how the reliability of the tomographic image is affected by errors or noise in the data during inversion. The significant error is the picking uncertainties for the arrivals. Besides, the test also can inspect how well of the velocity structure can be retrieved from the inversion. The stability of the solution is judged by inspecting whether the solution in returned to normal tomographic images or not. The steps of RRT method as followings:

(1) Set a synthetic model — The tomographic image obtained by the normal inverting the real data set is taken as the synthetic model.

(2) Calculate a set of synthetic travel time — Then, synthetic arrival times are calculated from three-dimensionally tracing rays in the synthetic model and added the random error as that contained in the real data set to the synthetic data set.

(3) Invert again — By inverting the synthetic data set by using the same inversion algorithm in normal inversion, the restoring image of the synthetic data is obtained.

(4) Comparing the images — By comparing the two result images between the normal inversion and the RRT, how well the main trend or some special structures in the real result is realistically restored can be found out.

4.3.4.3 Derivative Weight Sum

Solution quality is also described by a weighted hit count called the "Derivative weight sum (DWS)", an estimate of ray density near a grid point weighted by ray-node separation and ray-path length in the vicinity of the node (Evans et al., 1994). The DWS describes the amount of data actually constraining the velocity at that node. So, the DWS was taken into account in this study. The DWS values of 200 and 500 approximately are equal to recovery rates of 0.4 and 0.6 (Nakamichi et al., 2007). The recovery rate is zero when the resulting velocity perturbations are zero or have signs opposite the initial ones. Thus, the results with adequate ray coverage had DWS values of 200 or greater were used for analysis in this study.

Chapter 5 Procedure and Result

5.1 Study Procedure

Because the local seismicity is rather low in Taipei surrounding region, the study area was extended southward in order to increase more earthquake records and to offer more ray-paths for velocity inversion. The inversion region is bounded by latitude 24.50°N-25.31°N and longitude 121.15°E-122.00°E (Figure 17).

Because of the different monitoring purposes, the detection lower limit of earthquake magnitude of those networks that their records were used in this study is different. For instance, the network at TVG is small enough to monitor the micro-earthquakes those can not be detected in the CWBSN. Thus, the arrivals of events recorded by two temporal networks were picked manually (see appendix Ⅰ) to increase the ray-paths in this study. Then, these earthquakes were relocated by using 3DCOR computer program proposed by Wu et al. (2003) with the velocity model determined by Wu et al. (2007).

Consequently, the events with good quality were selected to determine *Vp* and *Vp*/*Vs* structures as well as focal mechanisms. Totally, 486 events including 5517 P arrivals and recorded by 286 stations were used for minimum 1D P-wave velocity model. These events were selected for at least 9 stations with station coverage gap less than 180°. All of the stations with epicenter distances were less than 50 km and the picking weightings of P arrival were less than 3 (Figure 25, Figure 26, Table 4). The P-wave velocity within the study region of the Wu's tomographic model was averaged as the priori model to obtain the minimum 1-D P-wave velocity model. The depths of the grid points are 0, 2, 4, 6, 9, 13, 17, 21, 25, 30, 35, 40, 50, 70, 90, 110, 140, 300 and

700 km. Because of the uncertainties of the S-wave arrivals, the Wadati diagram was calculated to obtain the *Vp*/*Vs* ratio in this target (Figure 28).

Results of the minimum 1-D P-wave velocity model, the value of *Vp*/*Vs* ratio from the Wadati diagram analysis and the appropriate damping parameters were taken as the initial models for the 3-D velocity model inversion. Totally, 6861 events were used with gap less than 270° and recorded by at least 7 stations with picking weighting of arrivals less than 3. The numbers of P-arrivals and S-P times for 6,861 events at 310 stations are 63,544 and 51,030, respectively. The P arrivals and S-P times were used in the inversion to determine *Vp* and *Vp*/*Vs* ratio model. In addition, the SIMUL2000 program also takes into account accuracy and reading error of arrival time by the manual weighted factors. The coarse tomographic result was obtained first and then calculated the finer tomographic result. The briefly procedure flow chart was shown as following:

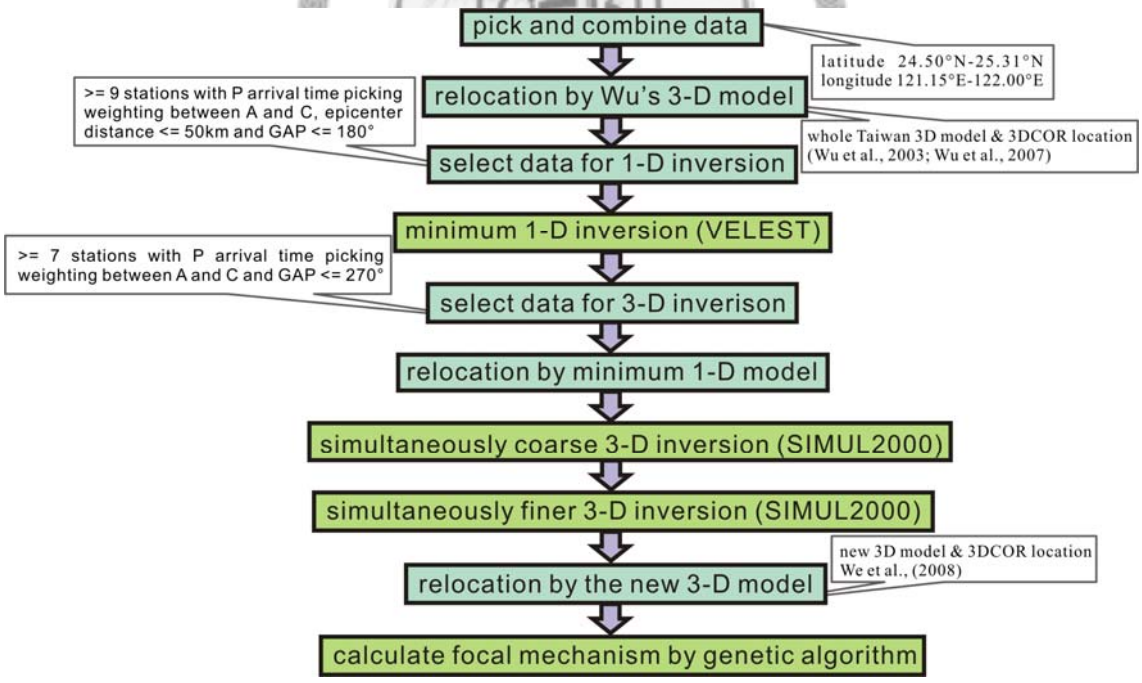

Figure 24. Data processing and analysis flow chart in this study.

5.2 Minimum 1-D Model Result

The VELEST program minimized the total estimated location errors with

corresponding station residuals (Figure 29). All of the station corrections were respect to a reference station. In this study, TWA station (red square in Figure 29) near the center of the inversion region and offers a large amount P and S arrivals. It was chosen as the reference station and maintained its initial delay as zero. Generally speaking, the stations with negative travel time residuals should lie in local high-velocity areas with respect to the reference station and those with positive travel time residuals should locate at the areas with local low-velocity. From the station residuals distribution in Figure 29, it does make some geological sense such as most of the stations in sedimentary region with positive travel time residuals and those in mountain region with negative travel time residuals. So, the station residual distribution does not violate a priori information within study region.

Besides, the average root-mean-square (RMS) of the hypocenter location was reduced from 0.155 to 0.096 sec (38% decrease) (Figure 30) and the average GAP was 102°. The priori and final minimum 1-D velocity model are shown in Figure 27.

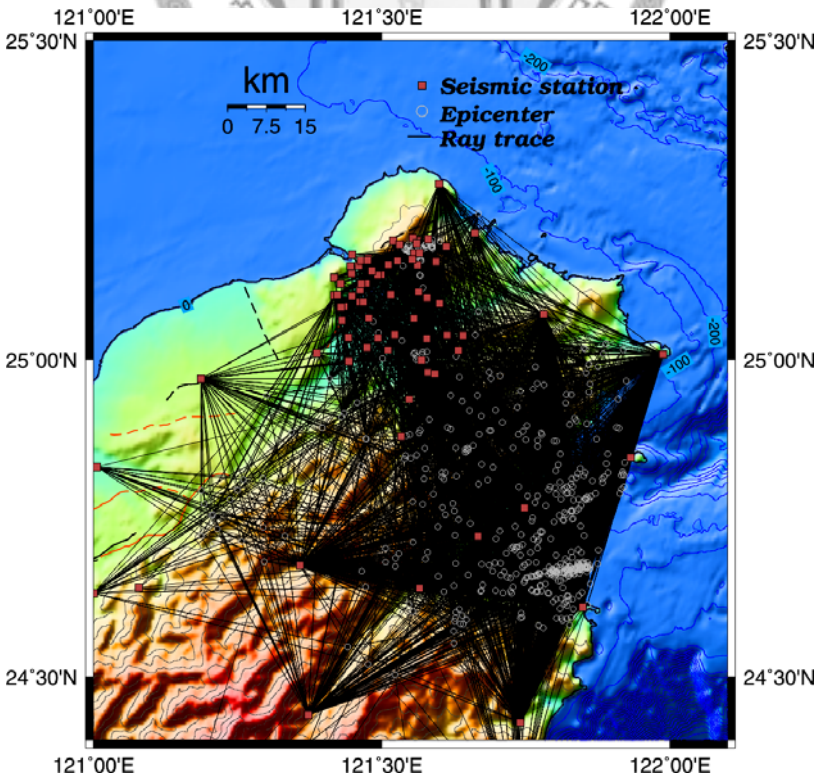

Figure 25. The ray-paths between earthquakes and recording stations.

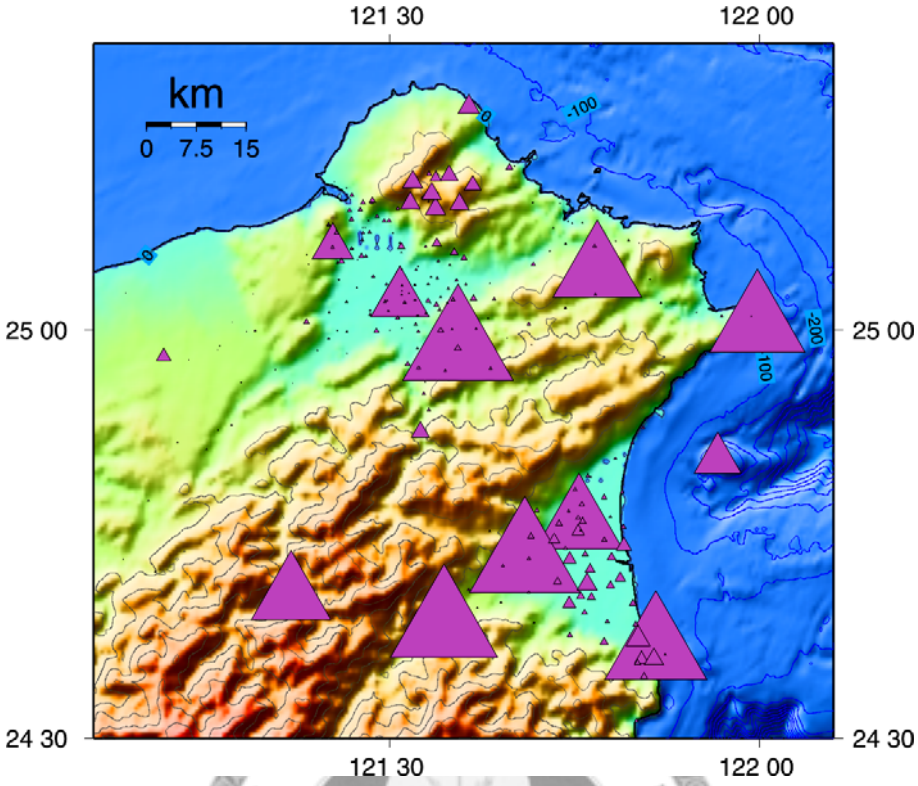

Figure 26. The recording number for VELEST. The cartoon shows seismic recording number in each station during executing VELEST. (see Table 4).

Table 5. The recording number for VELEST

Station	Number	The recording number (P arrivals only)							
TWA	416	TAP	210	YM05	73	E038	49	E042	31
TWE	416	EGS	178	E068	72	E028	47	E058	31
ENT	403	TWS1	155	YM06	72	YM02	43	E010	31
TWC	384	NNS	139	TWU	69	E037	42	E026	30
TWB1	359	E032	91	YM08	68	EHC	41	TWZ	29
NWF	335	TWY	82	YM07	63	E005	40	E014	29
ENA	330	YM01	77	E055	57	E008	37	E059	28
ILA	329	E027	75	NCU	54	TB09	35	TB08	27
NSK	299	YM03	75	E031	53	ANP	32	E060	27
TAP1	220	YM04	73	E046	49	E041	32	⋮	

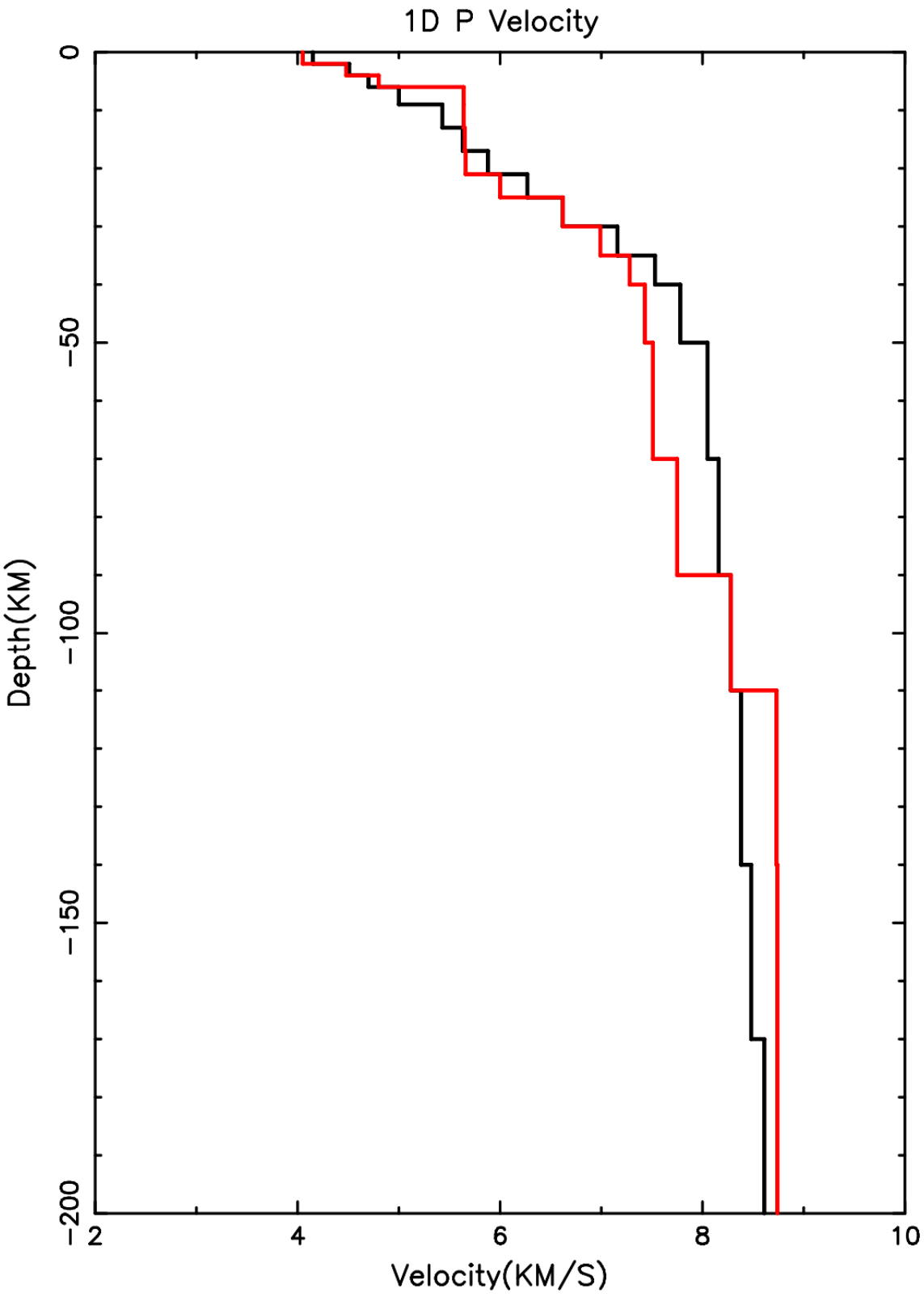

Figure 27. 1-D P-wave velocity model. The priori P-wave velocity model (black line) and the final minimum P-wave velocity model (red line).

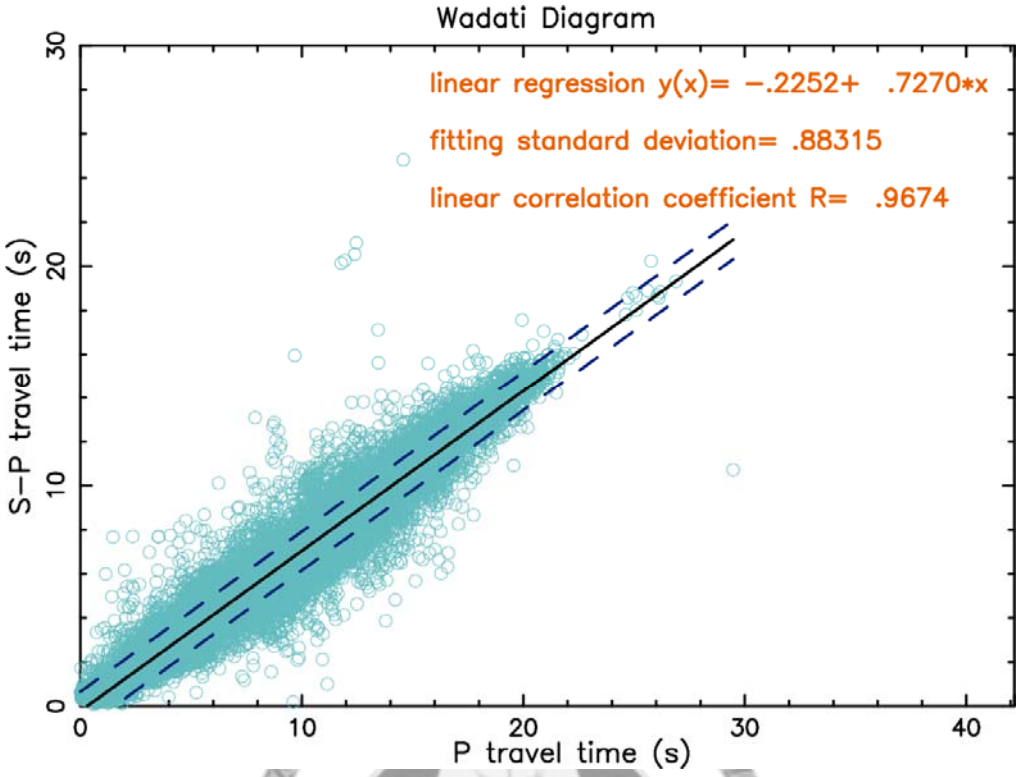

Figure 28. Wadati-diagram in the inversion region.

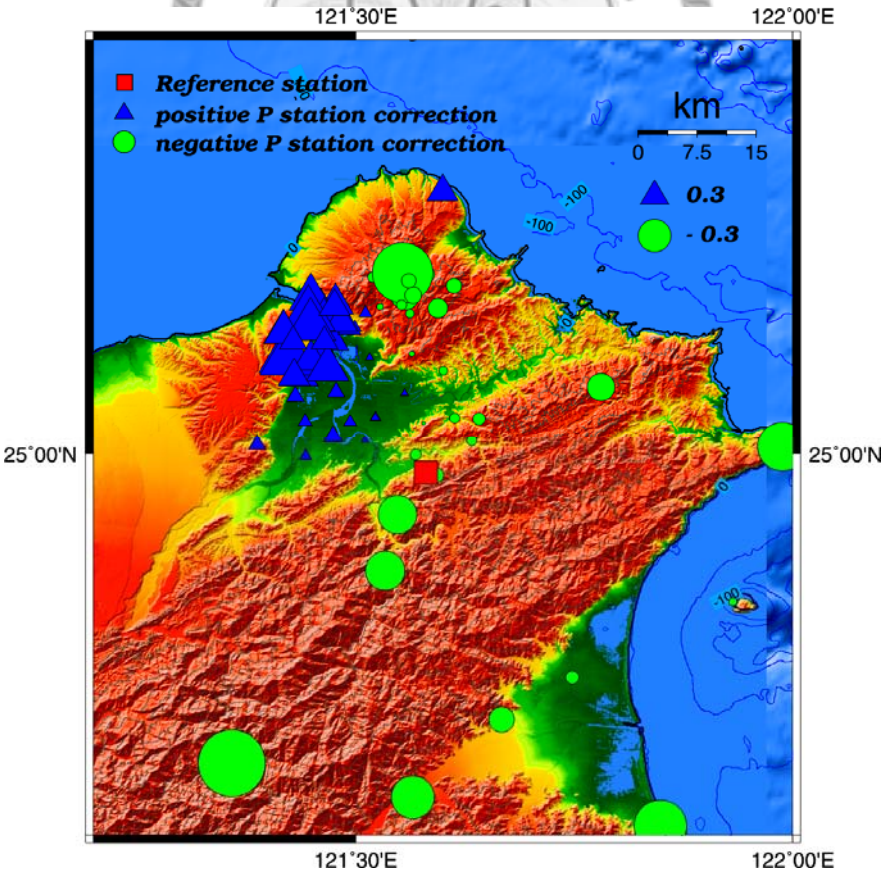

Figure 29. Station residuals of 1-D *Vp* model. The corresponding station residuals in the final minimum 1-D P-wave velocity model.

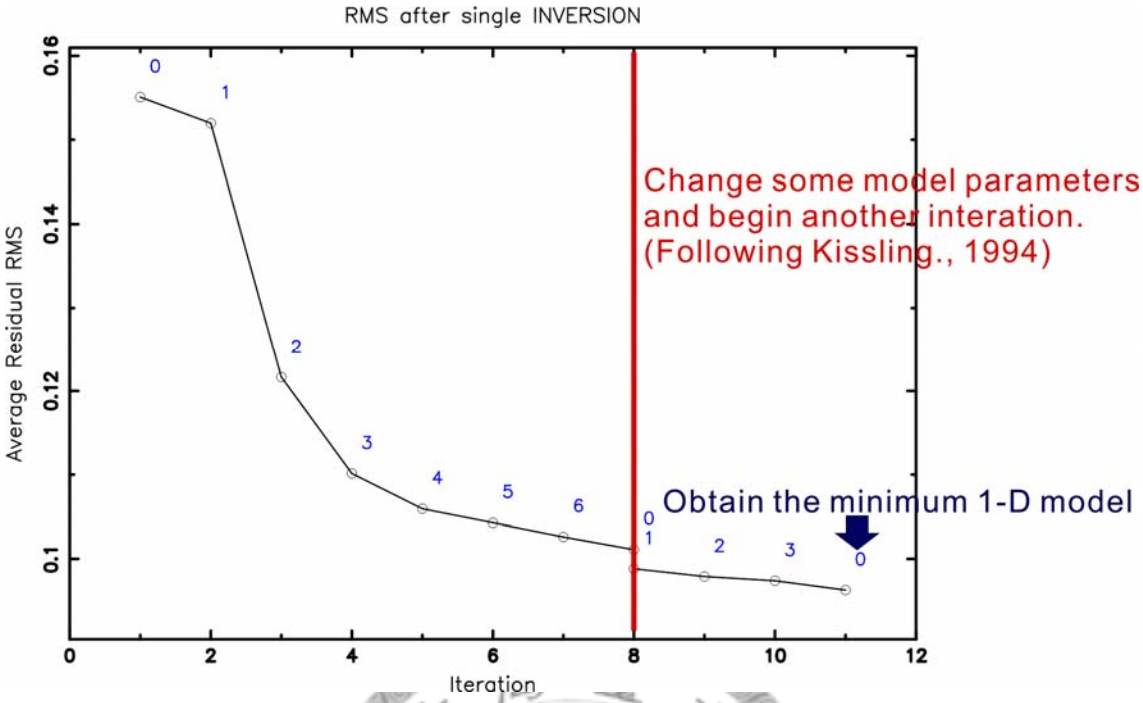

Figure 30. The RMS reduction in VELEST. RMS of the hypocenter location was continuously reduced during obtaining minimum 1-D velocity model.

5.3 Resolution Test

In order to check the reliability of the 3-D tomographic solution, the Checkerboard Resolution test (CRT; Grand, 1987) and the Restoring Resolution test (RRT; Zhao et al., 1992) were carried out. The checkerboard velocity model was constructed by assigning the velocity perturbations of $+3\%$ and -3% to the grid points and it lead to 6% velocity discontinuity across the boundary of checkerboard boxes. The block size in CRT is the same as that in coarse 3-D inversion.

From the P-wave velocity results of CRT, it shows only the portion with depth shallow than 9 km is well return to the checkerboard model in Taipei Basin and Tatun region. The small green squares in Figure 31 and 32 represent the station distribution of the seismic networks in metropolitan Taipei and the small seismic monitoring at TVG. The resolution is good within the region covered with the seismic stations. Moreover,

the *Vp*/*Vs* resolution is poor than P-wave velocity resolution and it is only good in layers at depths shallow than 6 km in target region. It is because that most of earthquakes occurred within the target region are shallow than 10 km and seldom earthquake occurred between 10 and 60 km (Figure 33). Those earthquakes with depth larger than 60 km are associated with the subducting slab. So, the poor resolution in the target region makes sense. Thus, the results on the shallow portion of the target region were discussed.

On the other hand, the reliability of the coarse solution was checked by RRT. The arrival time data was made by adding random errors with standard deviations of 0.02 s for P-wave and 0.05 s for S-wave to theoretical data set, respectively. It is because that S-wave is generally contaminated by the P-wave coda and then has larger picking errors. Moreover, the same picking errors were used in Nakamichi et al., (2007) and its inversion region is approximately the same as the target region in this study. In order to understand the image recovery, a quantity called the "recovery rate" was introduced (Nakamichi et al., 2007). It is drawn in black when the tomographic result of coarse normal inversion is completely recovered or a little bit over-recovered and is approximately white when the resulting velocity perturbation is zero or has sign opposite the tomographic result of coarse normal inversion. If the tomographic result of RRT is widely over-recovered, the region is drawn in light purple. In Figures 35 to 39, most of area is over-recovered, especially beneath TVG. But the main pattern of the tomographic results does not have significant difference. So, it means the main geological trend and structures is approximately imaged upon the data set. Besides, the recovery results seem to correlate with the hypocenter and station distribution. It means it is deeply influenced by the ray-paths of seismic waves. Thus, the lack of events in the target region is a dominant influence in obtaining the detail tomographic images.

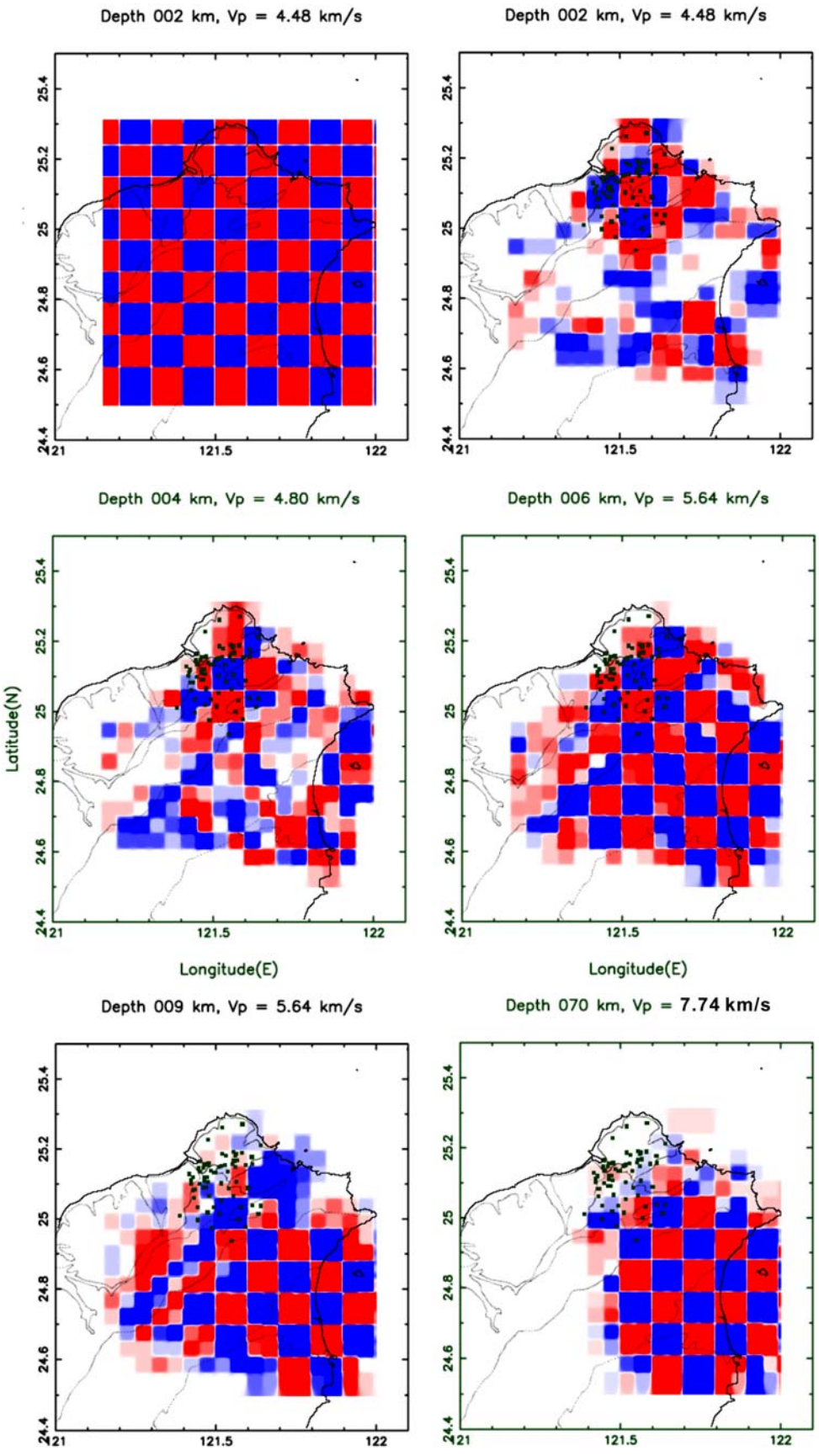

Figure 31. The checkerboard test result of P-wave velocity.

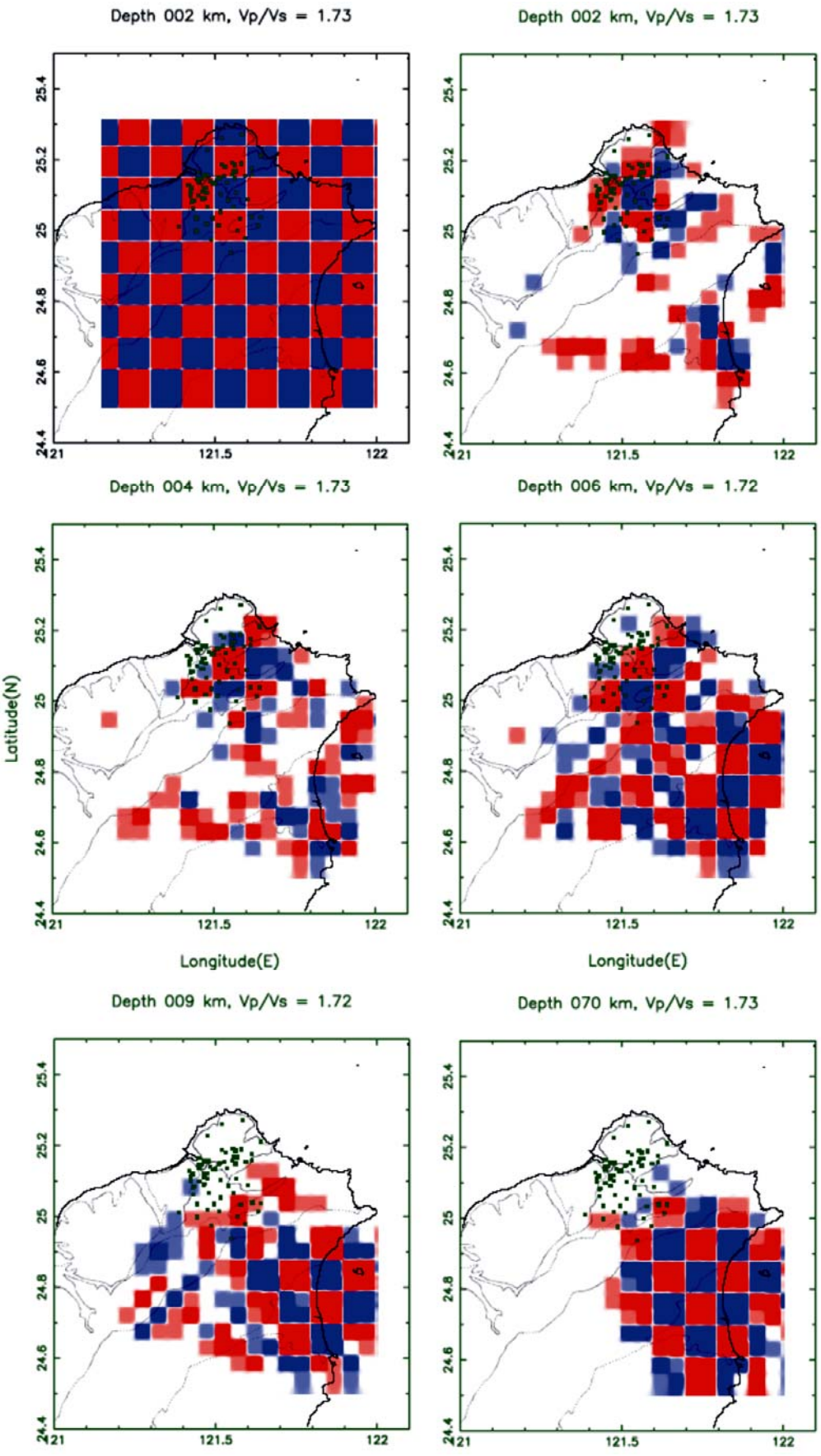

Figure 32. The checkerboard test result of *Vp*/*Vs* ratio.

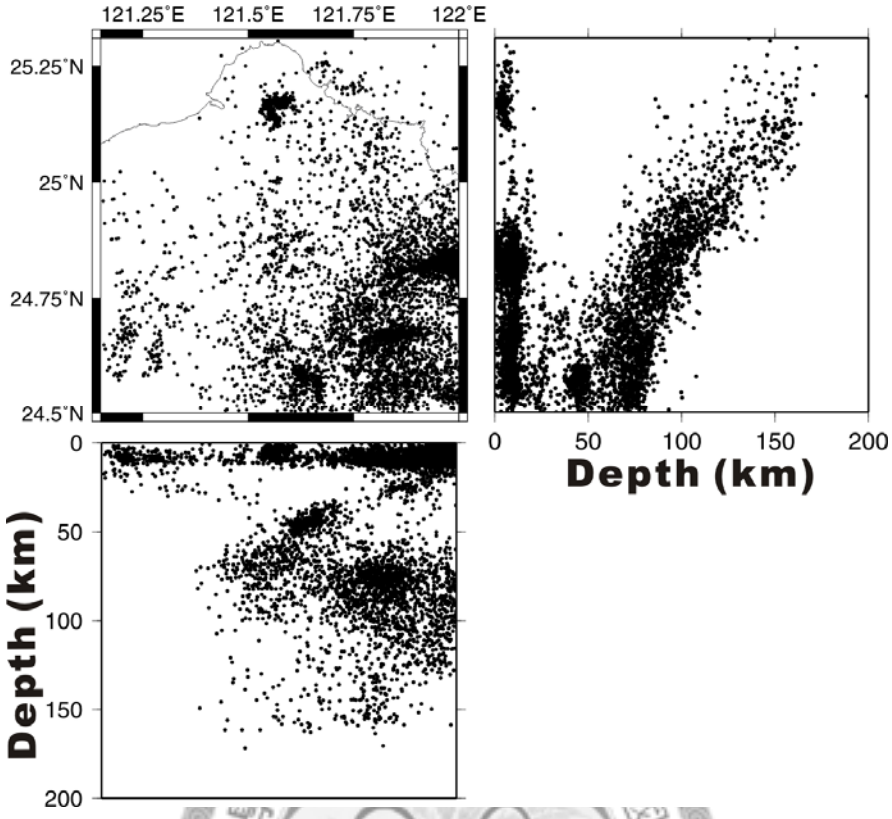

Figure 33. The relocated earthquakes distribution.

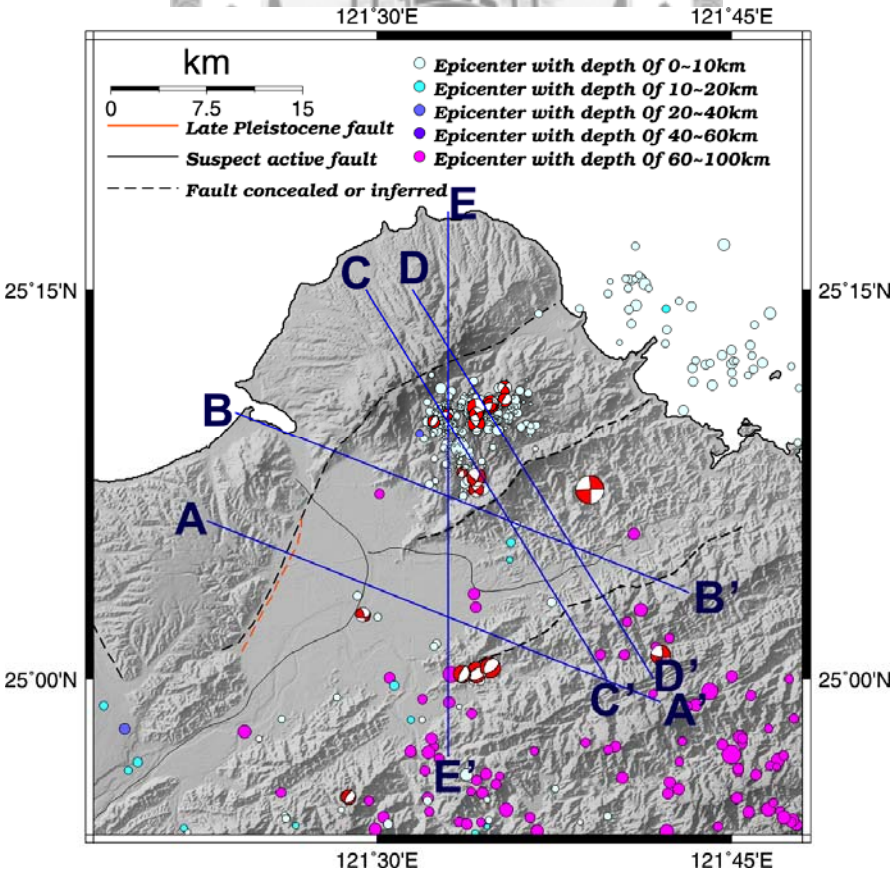

Figure 34. Locations of profiles A to E.

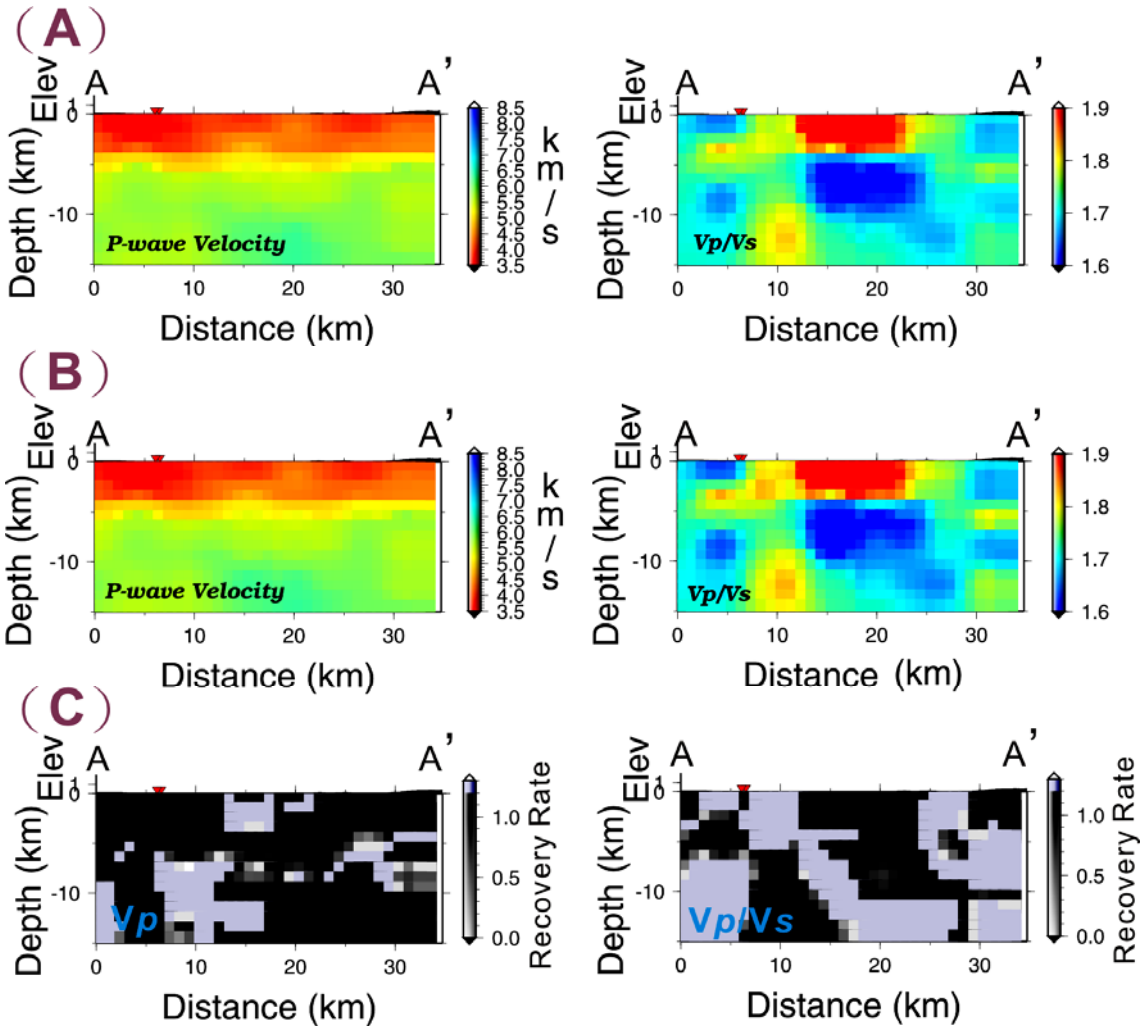

Figure 35. Reliability test along profile AA'. (A) Results of the coarse normal inversion along AA'. (B) Results of the RRT along profile AA'. (C) Tomographic recovery rate along profile AA'.

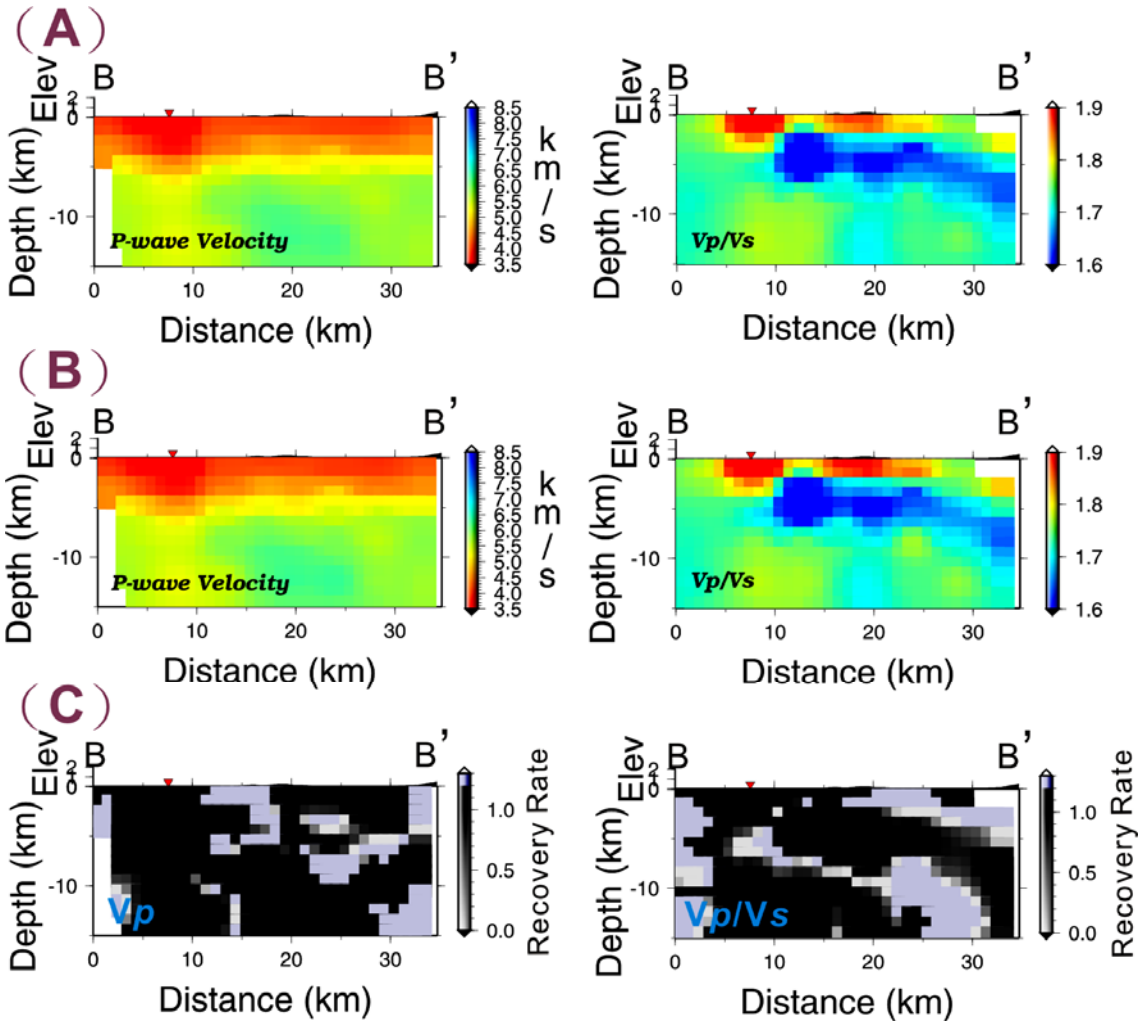

Figure 36. Reliability test along profile BB'. (A) Results of the coarse normal inversion along BB'. (B) Results of the RRT along profile BB'. (C) Tomographic recovery rate along profile BB'.

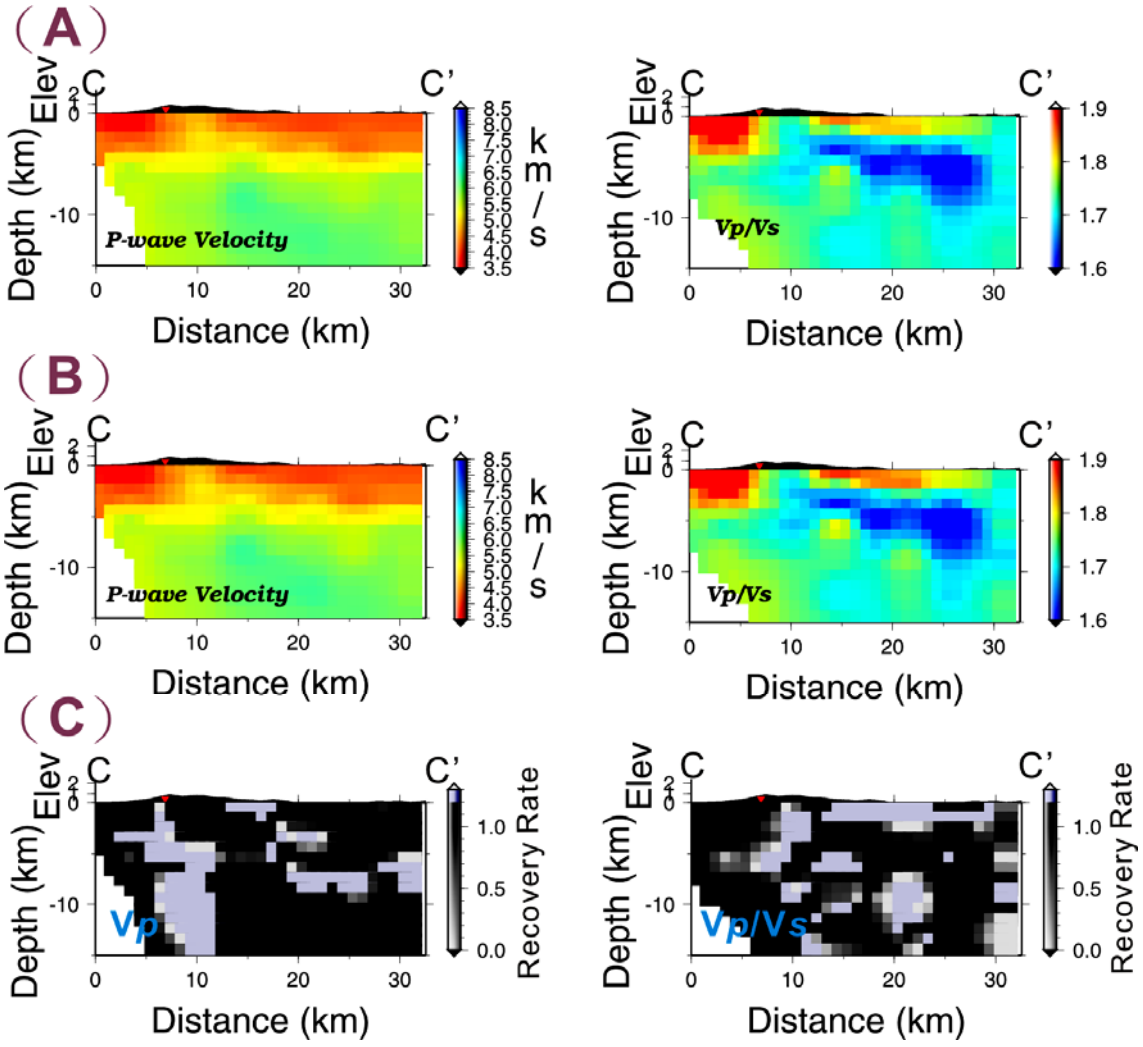

Figure 37. Reliability test along profile CC'. (A) Results of the coarse normal inversion along profile CC'. (B) Results of the RRT along CC'. (C) Tomographic recovery rate along CC'.

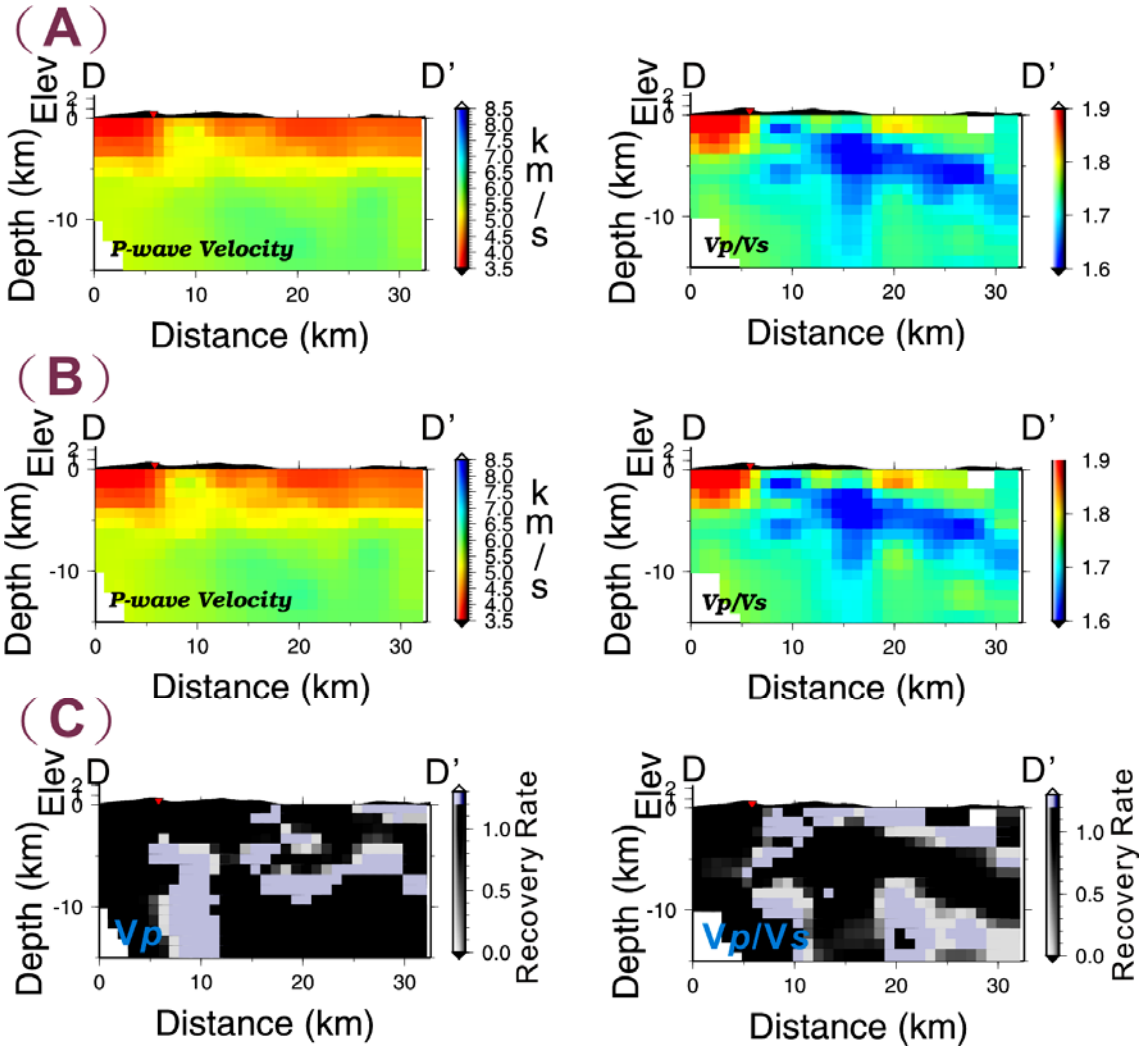

Figure 38. Reliability test along profile DD'. (A) Results of the coarse normal inversion along profile DD'. (B) Results of the RRT along profile DD'. (C) Tomographic recovery rate along profile DD'.

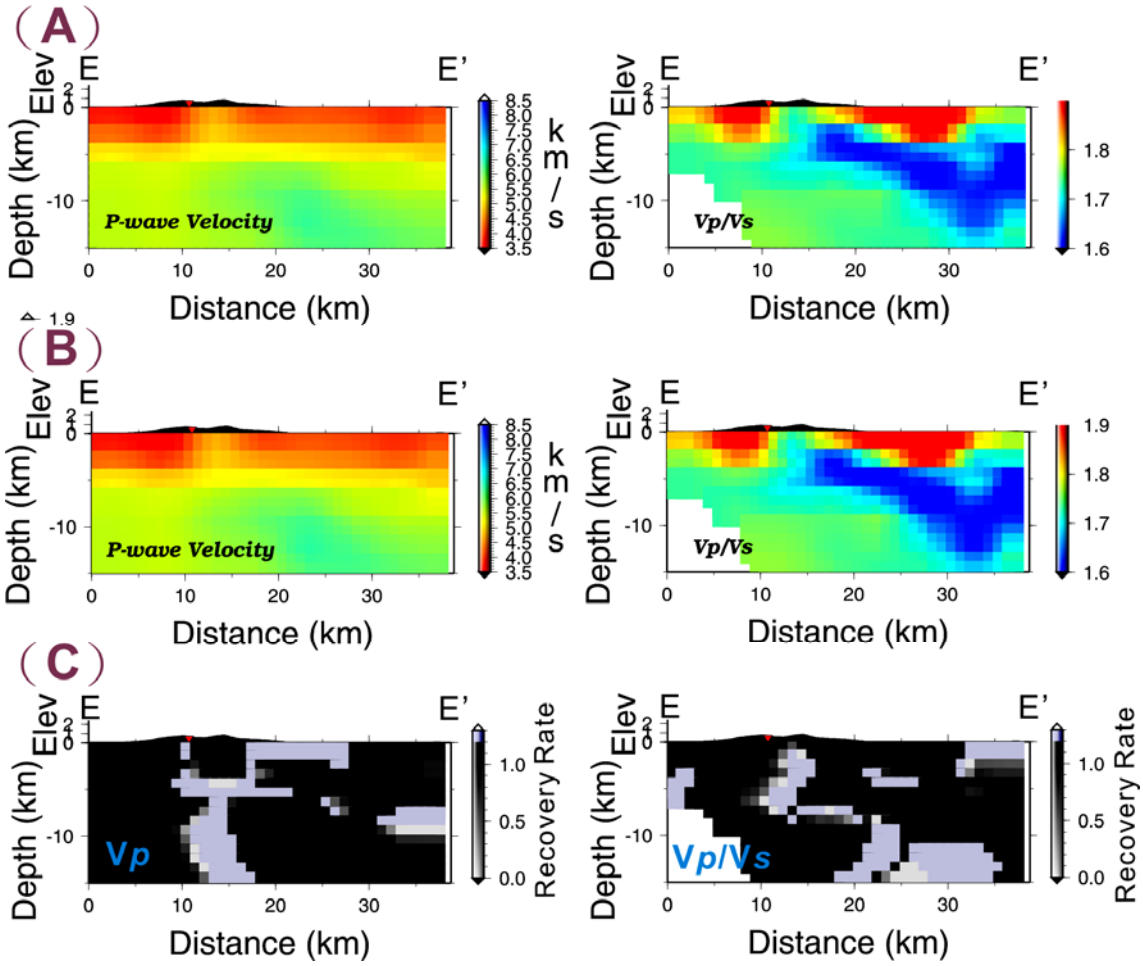

Figure 39. Reliability test along profile EE'. (A) Results of the coarse normal inversion along profile EE'. (B) Results of the RRT along profile EE'. (C) Tomographic recovery rate along EE'.

5.4 3-D Velocity Model Result

Detail tomographic images and the relocated hypocenters distribution were shown in Figure 40 to 44. The earthquakes within 2 km to the profile are plotted. Figure 46 shows the recordings number of each station was used in this study. In Figure 40, Figure 41 and Figure 44, the Taipei Basin is well imaged as the high *Vp*/*Vs* ratio in the near-surface portion.

A significant lower *Vp*/*Vs* ratio zone which seems associated with the Chinshan and Shanchiao fault is observed through entire region. Chang (2004) studied the 3-D *Vp*, *Vp*/*Vs* and Qp structures beneath TVG and also found the significant high *Vp*, high *Vs* and low *Vp*/*Vs* ratio inclining toward southeast beneath TVG. Because the Chinshan fault is formed earlier than the eruption of Tatun volcanoes, they inferred the feature to the solidification igneous rock along Chinshan fault. But, the significant zone is a continuous feature through entire study region in this study (Figure 44). Because of the poor resolution of the depth larger than 9 km in Taipei Basin and 6 km in TVG, the feature might reflect the hard rock site relative to the upper soft sedimentary. Besides, most of the earthquakes occurred beneath Taipei Basin are located within this zone. The feature also well depicts the half-graben shape of Taipei Basin in Figure 44.

A high *Vp* and low *Vp*/*Vs* ratio region beneath TVG at subsurface zone should represents the solidified igneous rock (Figure 42, Figure 43). In Figure 45, the *Vp* and *Vs* perturbation maps also show the shallow portion with higher *Vp* and higher *Vs* relative to the surrounding region.

Result of depth larger than 10km in Figure 42 and 43 due to lack of earthquakes, it is not clear to identify that a region with relatively high *Vp*/*Vs* and low *Vp* exist or not. It may be caused by inadequate ray-paths passing through and the unsuitable ray tracing

algorithms used in this study. Zhao et al. (1992) pointed out the pseudobending technique fails to work when velocity discontinuities exist and it only can be applicable to continuous velocity models. So, if a magma chamber or fluid saturated zone really exists, the pseudobending technique may be inappropriate.

Based on the earthquakes locations, there seems that a seismogenic zone is perpendicular to the Chinshan fault beneath TVG. This zone with seismicity may correlate with the Chinshan fault. This part will be discussed in next section.

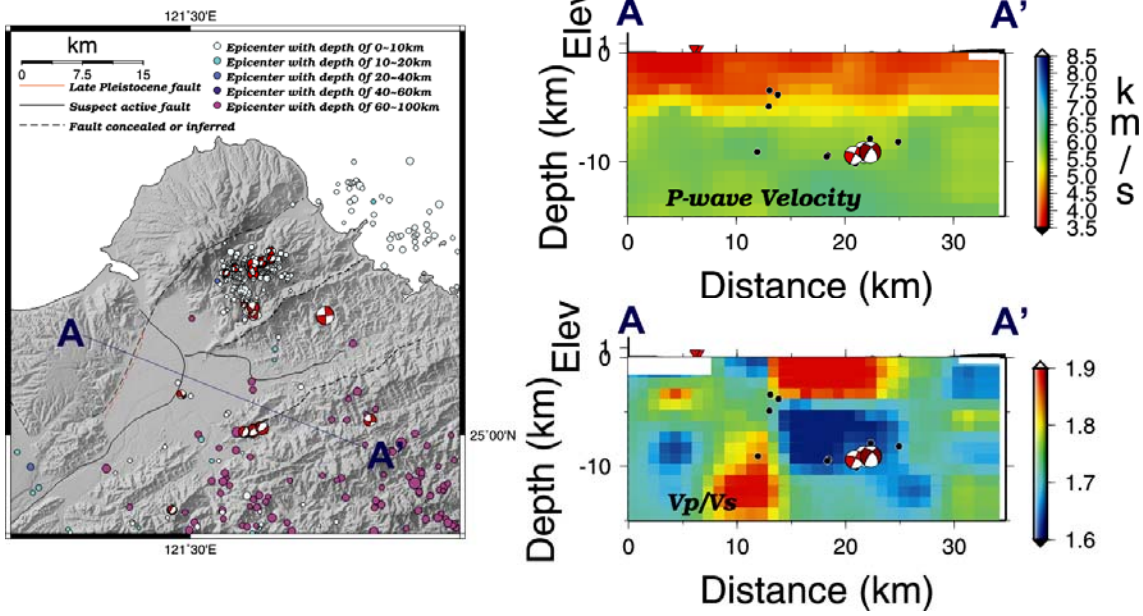

Figure 40. The tomographic profile along line AA'.

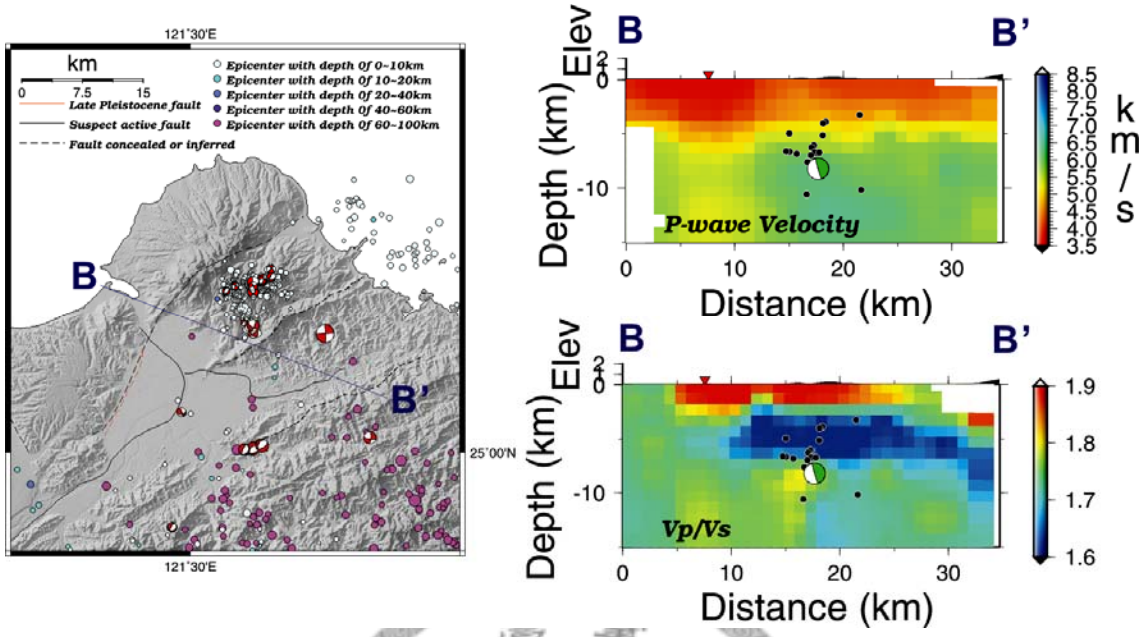

Figure 41. The tomographic profile along line BB'.

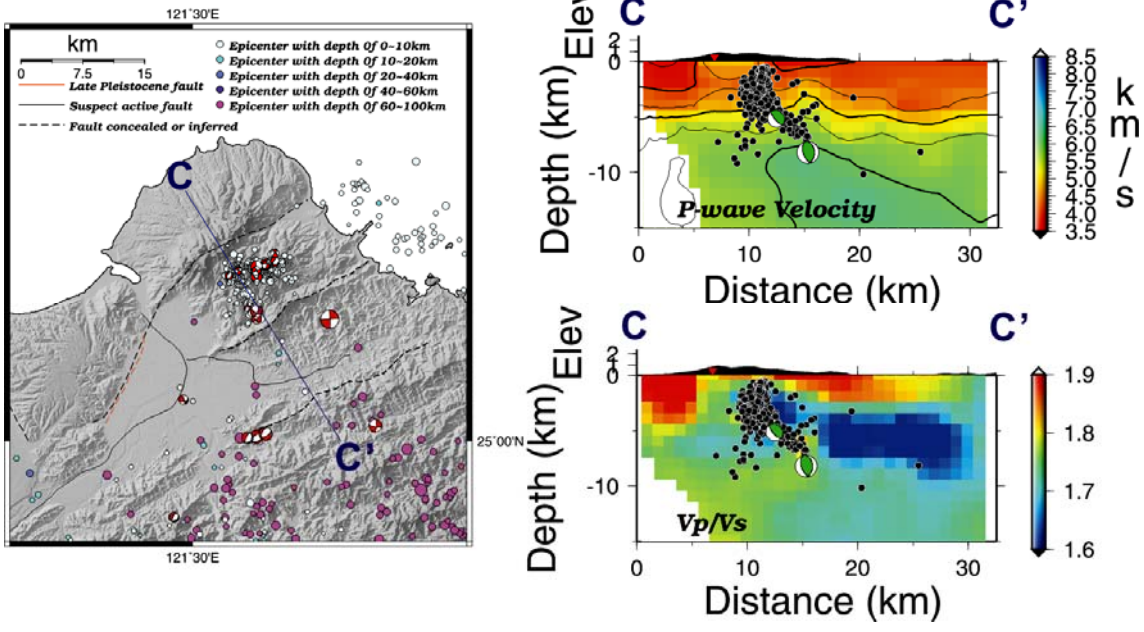

Figure 42. The tomographic profile along line CC'.

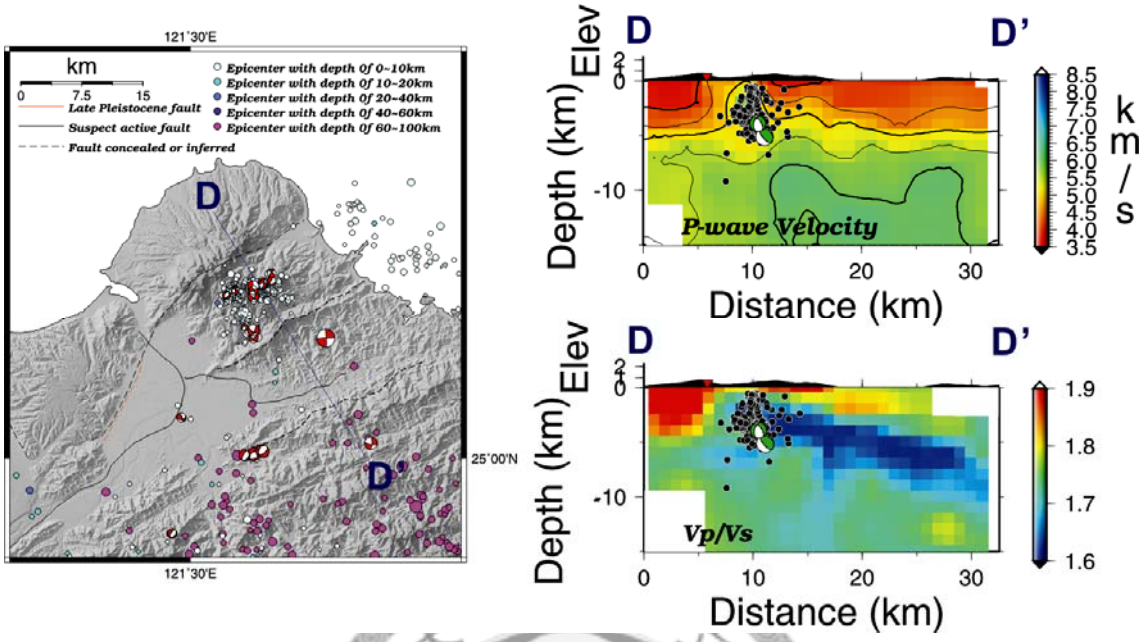

Figure 43. The tomographic profile along line DD'.

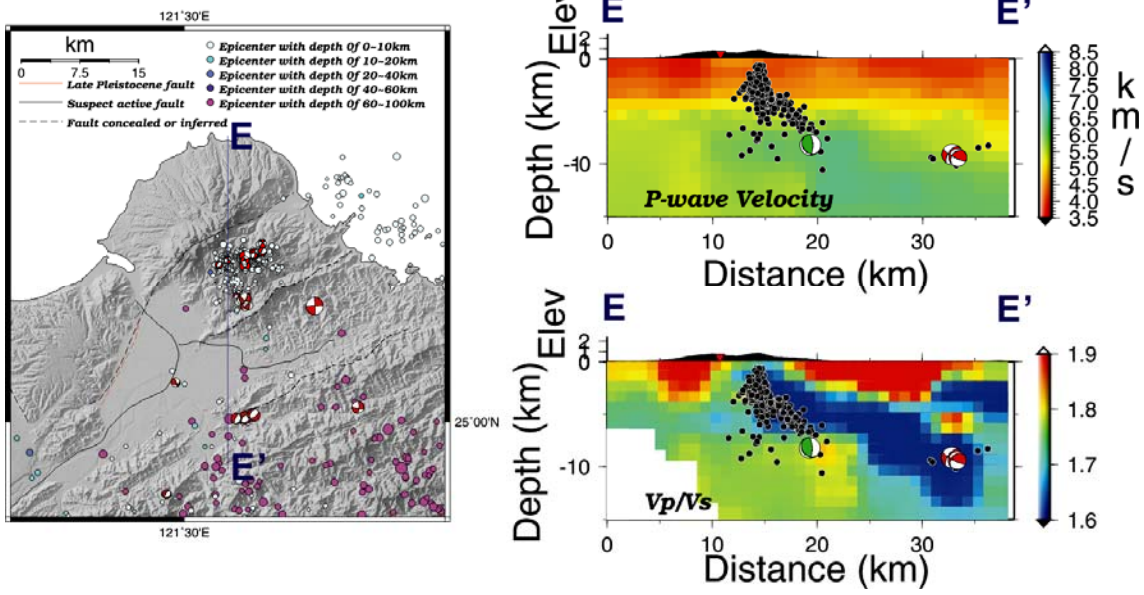

Figure 44. The tomographic profile along line EE'.

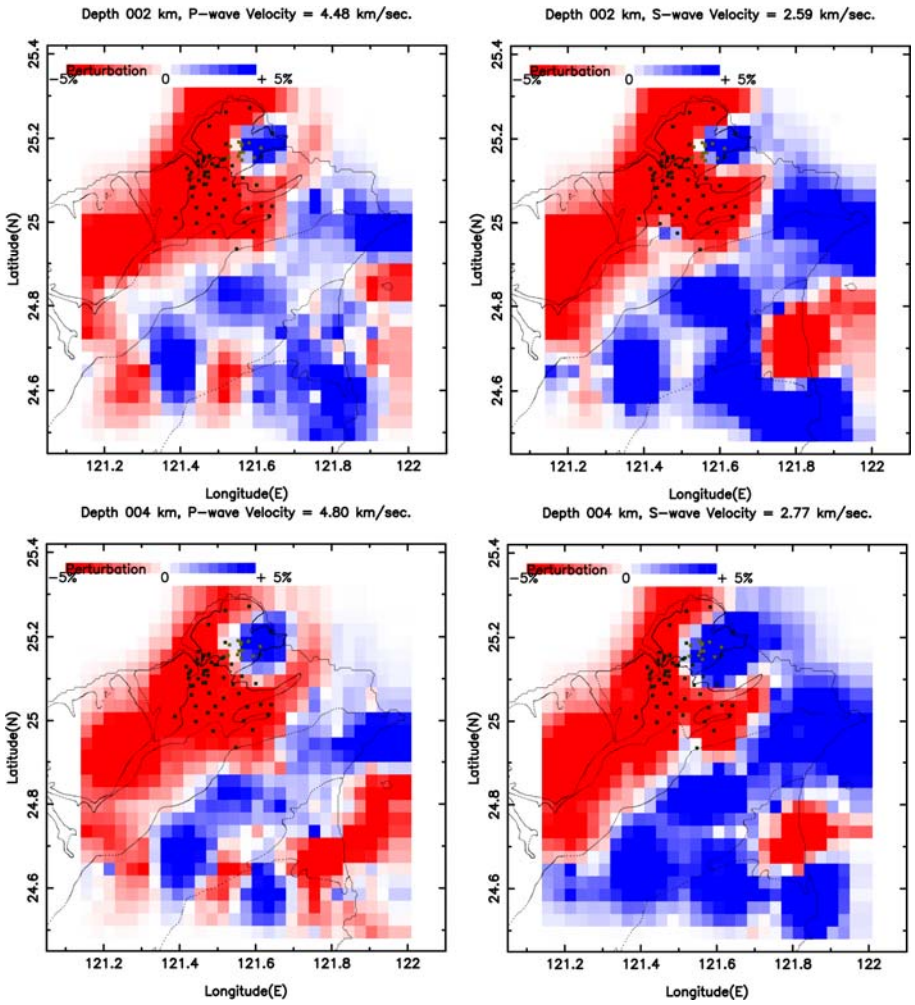

Figure 45. *Vp* and *Vs* perturbation maps at 2 and 4 km depth. The green square represents the seismic network in Taipei Basin and the gray square is the station in TVG.

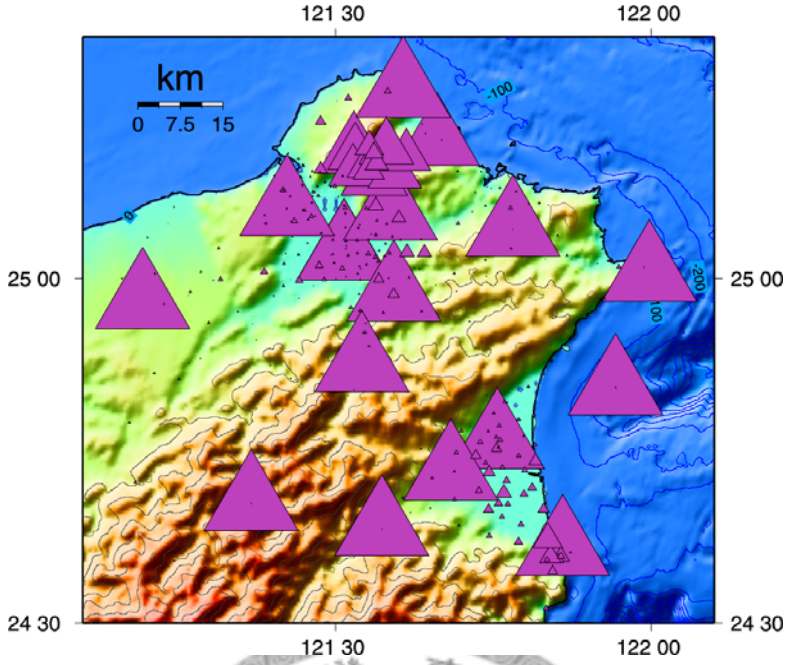

Figure 46. The recording number for SIMUL2000. The cartoon shows seismic recording number in each station during executing SIMUL2000 (see Table 5).

Table 6. The recording number for SIMUL2000.

Station	Number	The recording number for SIMUL2000 (P phases + P-S time)							
TWE	6049	TWU	1907	YM03	581	YM12	202	E038	126
TWC	6030	EGS	1757	YM06	567	TWCP	186	TB25	121
TWB1	5645	TAP1	1657	YM04	520	E027	161	E059	118
TWA	5459	NCU	1500	YM07	518	TB09	159	TB19	112
ENT	5136	TAP	1243	YM05	511	TB22	157	E007	109
TWS1	4856	TWZ	1149	YM10	332	TB28	151	E037	107
NSK	4639	TWX	893	E032	314	E027	146	TB32	107
NWF	4071	ANP	771	YM09	303	E055	144	E028	106
TWY	3180	YM01	704	YM11	247	TB02	144	E046	106
ILA	2324	YM08	582	E031	227	YM02	139	⋮	

5.5 Seismicity & Focal Mechanism

First motion focal mechanisms determined by genetic algorithm are used in this study (Wu et al., 2008). The events are recorded by at least 7 stations and offer equal or more than seven polarity readings. Only the solutions with quality factor Q larger than 0.1 were discussed hereafter.

The hypocenter distribution was plotted and examined in three-dimension with Gocad program (Mallet, 1989, 1992). Most of the earthquakes beneath TVG occurred at depth shallow than 8 km and most of the focal mechanisms of these earthquakes are dominantly in normal fault type with strike-slip component. The double-couple focal mechanisms in this area varied greatly even the events are close in time and spatial windows (Figure 47). The locations of three earthquake pairs with focal mechanism solutions can be identified in Figure 48 and their locations (red, blue and purple circle in Figure 48) are beneath the Tayukeng, and Matsao regions.

Based on the hypocenter distribution, all of earthquakes occurred within the hanging wall and extended to the surface. Those earthquakes can be divided into two groups with different trends (Figures 50, 51). These two seismogenic zones at the shallow portion are coincident with the surface hydrothermal regions with hot spring and fumaroles. Those regions include Chishing Mountain, Matsao and Tayukeng (Figure 52).

Chan et al. (2006) applied high-resolution airborne LiDAR-derived digital terrain model to characterize the TVG and they discovered clear distribution and pattern of the joints and fractures in TVG. Lee et al. (2008) also observed a short-term increasing trend in HCl concentration, SO_2/H_2S ratio and the temperature of fumaroles and they proposed that the ascending of more magmatic or primary hydrothermal fluid along the

fractures likely caused the change. In Figure 49 and Figure 52B, the earthquake distribution pattern is vertical near the surface. Thus, it seems that these earthquakes are weakly correlated with the nearest fault - Chinshan fault. Those earthquakes may occur around the broken zone and unobstructed conduits exist beneath the Matsao, Tayukeng and Chishing mountain regions for the gas and liquid passing through will be suggested in this study. Besides, the clear unobstructed conduits also can explain that the $^{3}He/^{4}He$ data obtained from Tayukeng show consistent variation and independent with the rainfall (Ho, 2001). Furthermore, the unobstructed conduits could maintain the outgasing system at relatively steady status.

In Figure 48 and 52B, there seems no obvious fracture between these two seismogenic zones and these two zones incline to different directions. The seismicity beneath Chishing mountain inclines to the southeast. Base on the result of seismicity and geochemistry analysis, Konstantinou et al. (2007) and Lee et al. (2008) concluded that a magma chamber might exist beneath in the area. Wright et al. (2006) studied the Nubia-Arabia plate boundary and concluded the magma intrusion would be rather via dyke pattern than segmented normal faulting. Motoki and Sichel (2008) proposed that the magma pressure, depth and local stresses conditions are important to define the cause of the intrusion. One is that tensile fracture formation for dyke intrusion takes place and the other one is the magma intrusions filled along pre-existing fractures. They also inferred that in an extensional stress field such as an active back-arc volcanoes, new fractures open relatively easily and magma does not fill the parallel normal faults. The dykes are formed by tensile fracturing and vertical. On the contrary, faults are formed by shear fracturing and show a high to low-angle dip. These two seismogenic zones (Figure 50, 51) may imply that they are different passageways for the hydrothermal fluid and gas to ascend along from different sources.

The swarm activity around active volcano is generally accompanied with vertical deformation (Hill et al., 2003). But, based on the precise leveling result, a total subsidence of 10mm was detected for 14 months from June 2006 to August 2007 around Chishing mountain (Murase et al., 2007). Thus, the micro-seismic activity and the opening fracture seem more closely related.

Based on gravity and magnetic surveys, Yang et al. (1994) pointed out the Chishing mountain has local high gravity zone but a low magnetic anomaly. It could be the result of hydrothermal alternation. The continuous and well-developed fracture zone beneath Chishing mountain seismological evidence in this study can support that the magnetic minerals in the rocks have high possible been removed or transformed already.

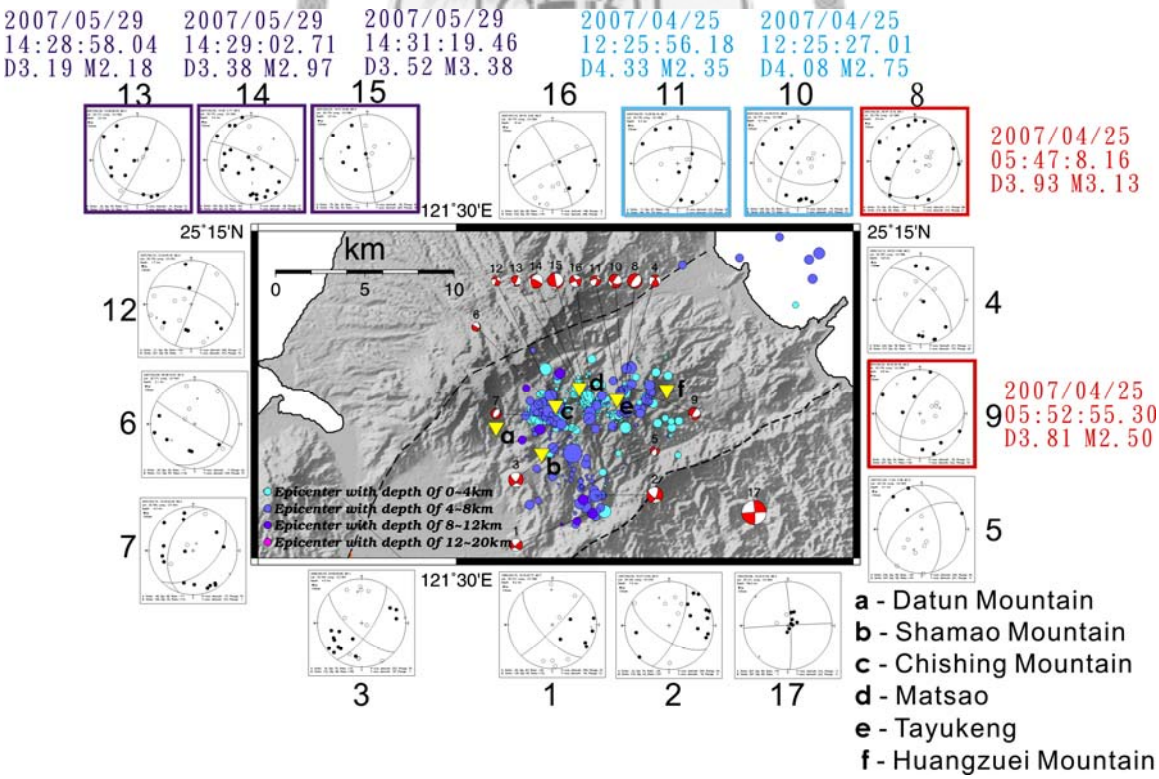

Figure 47. The focal mechanism distribution in TVG (see appendix Ⅱ). The group color means the cluster event.

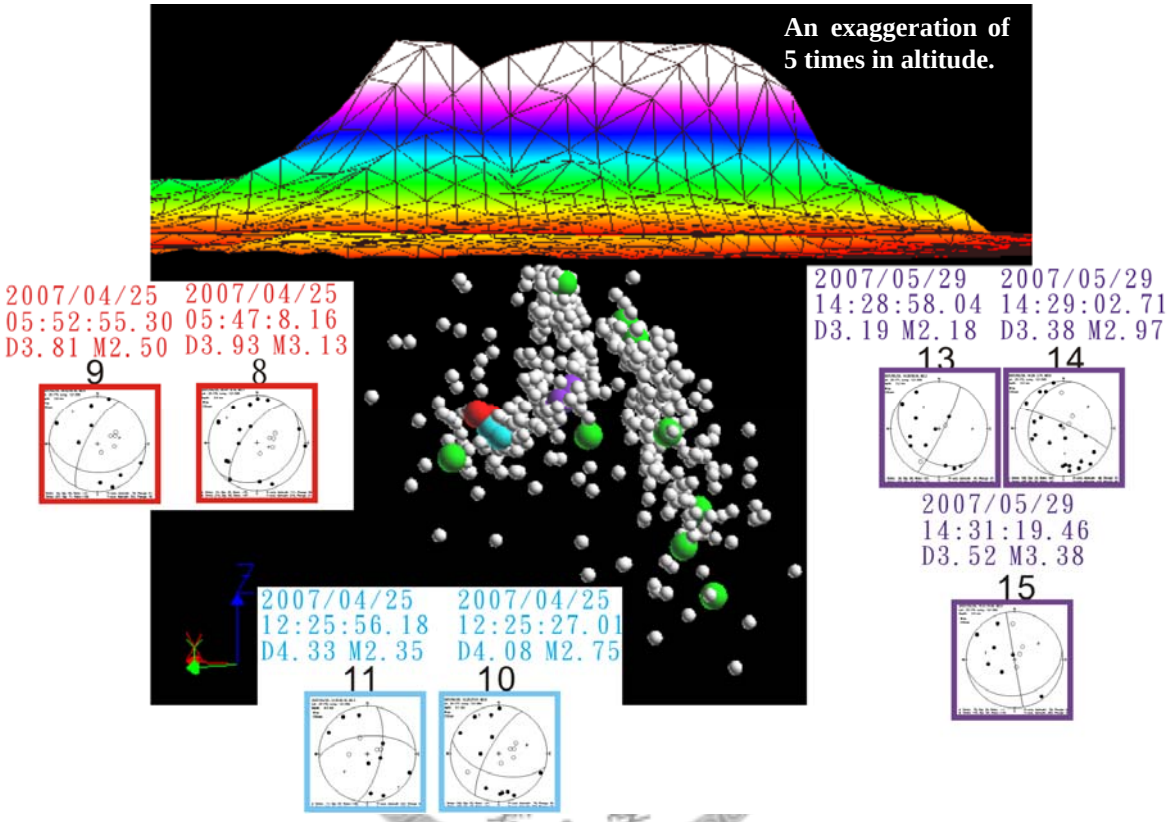

Figure 48. The 3-D focal mechanism distribution in TVG. The red circles represent the location of focal mechanism solution 8 and 9. The blue ones are solution 10 and 11 and the purple ones are solution 13, 14 and 15.The green circles represent the locations of the other focal mechanism solutions in Figure 47.

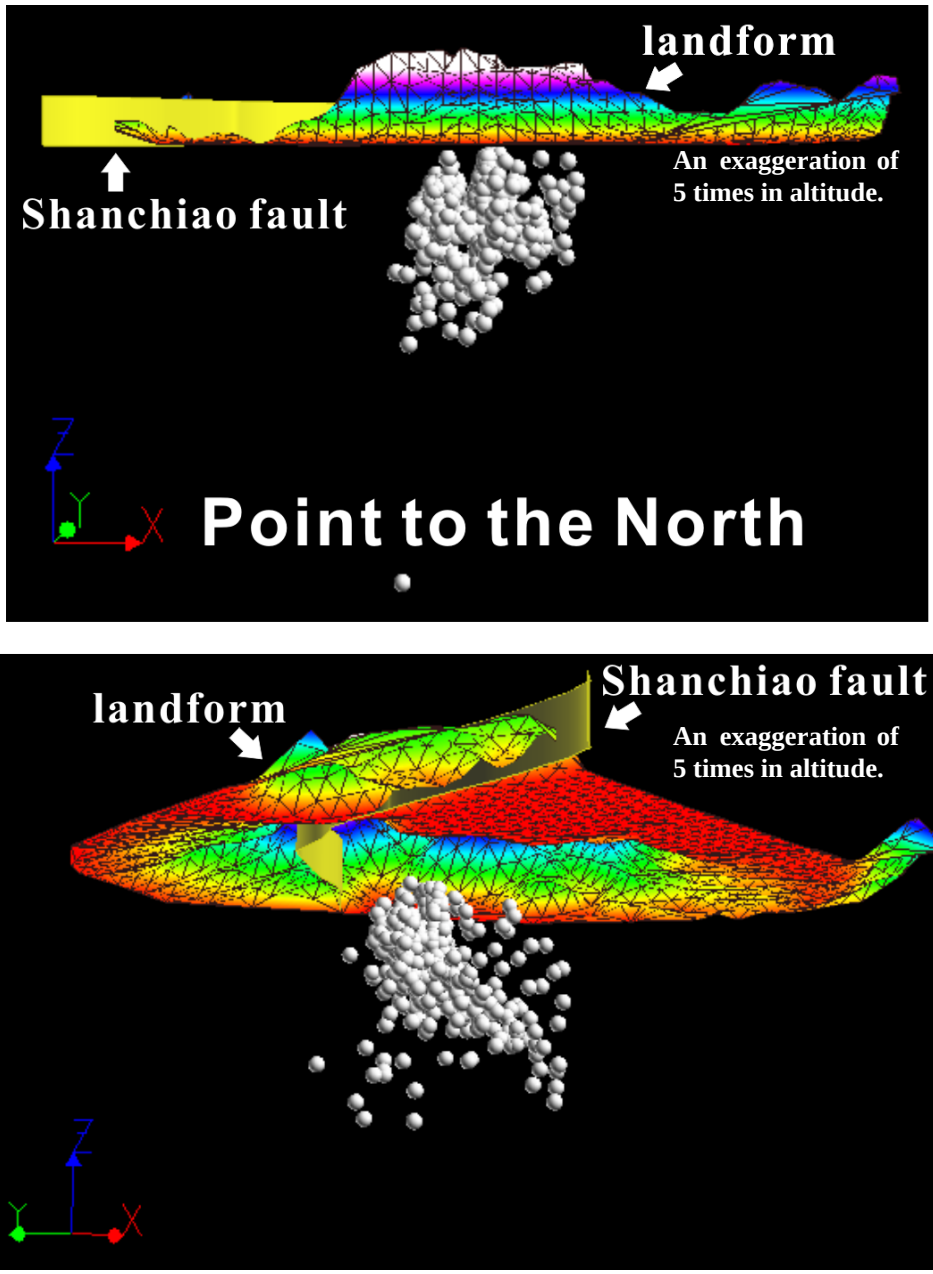

Figure 49. The hypocenter and the surface trace of the Shanchiao fault.

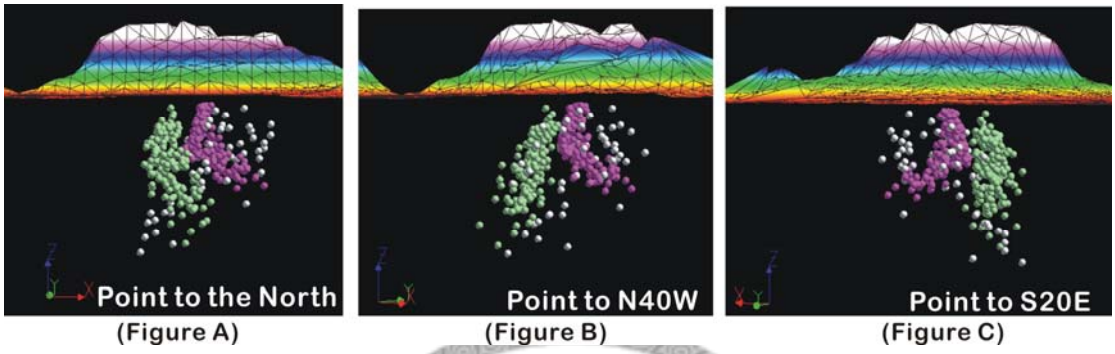

Figure 50. Two earthquake groups beneath TVG. Most of the earthquakes recorded by 7~10 stations can be identified into two clusters (green and red groups) based on its hypocenter distribution.

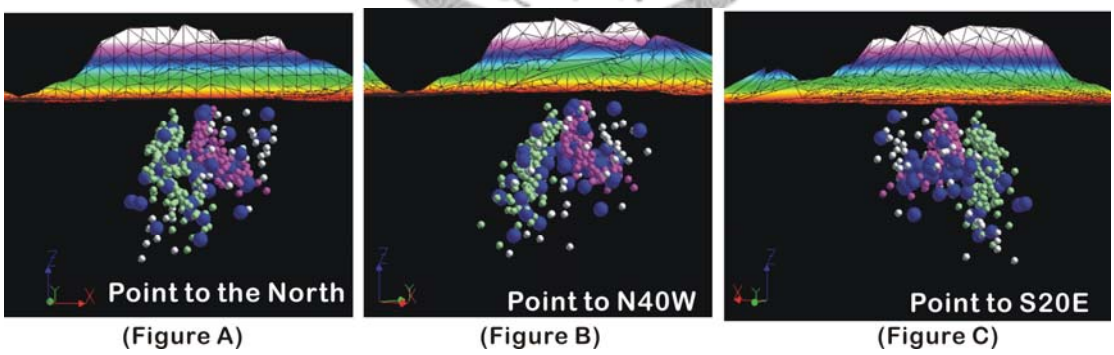

Figure 51. Two earthquake groups beneath TVG. The bigger blue balls represent the events were recorded by at least 11 stations and most of them still occurred within the two clusters.

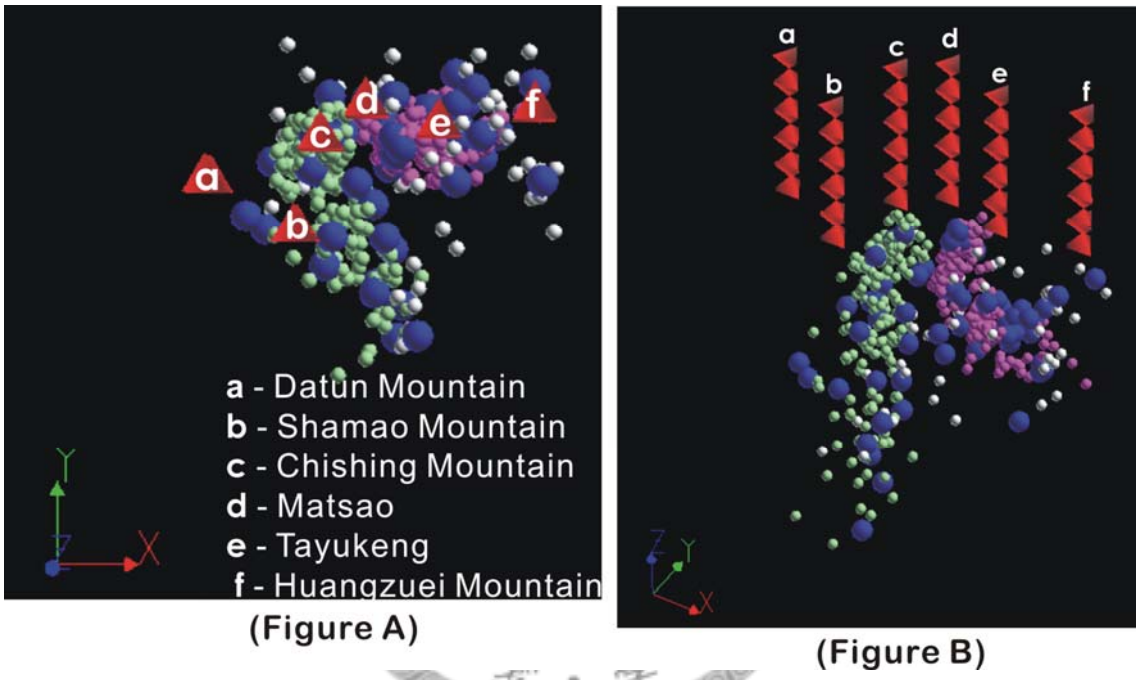

Figure 52. The earthquake clusters distribution beneath TVG and related localities. Taking the topography out, these two seismogenic zones are coincident with the surface significant hydrothermal regions with hot spring and fumaroles.

Chapter 6 Conclusions

In this study, a detail tomography was taken in order to understand the seismogenic structures, earthquake and volcanic activities in Northern Taiwan region especially in Taipei Basin and TVG regions. According to the analysis and discussion several results are obtained as follows:

(1) A significant half-graben shape is depicted in the tomography image with low *Vp*/*Vs* ratio through entire region. The feature might reflect the hard rock site relative to the upper soft sedimentary.

(2) The earthquakes occurred in the TVG region may correlate to local hydrothermal activity rather than Chinshan fault base on results from tomography, seismicity and focal mechanism, especially a considerable variation in focal mechanisms solutions.

(3) Two seismogenic zones beneath TVG are coincident with the surface hydrothermal regions. The unobstructed conduits may exist beneath the Matsao, Tayukeng and Chishing mountain regions.

(4) Because of no connection between these two seismogenic zones beneath the TVG. It may imply that there are two different hydrothermal sources.

The accurate earthquake location is very important to recognize the conduits beneath TVG. So, the tomography algorithm including calculating the difference of absolute travel-time between neighboring event pairs such as tomoDD (Zhang and

Thurber, 2003) should be an appropriate tool to study this region. Besides, because of the abundant seismogram recordings due to combining the data from different networks, it is worthy to more detail analyze the waveform information in the future.

Reference

Aki, K., & Lee, W. H. K. (1976). Determination of three-dimensional velocity anomalies under a seismic array using first P arrival times from local earthquakes, 1. A homogeneous initial model. *Journal of Geophysical Research, 81*(23), 4,381-4,399.

Chan, Y.-C., Chang, K.-J., Chen, R.-F., Lee, J.-C., & Hsieh, Y.-C. (2006) Active Extensional Structures Discovered by the Airborne LiDAR Mapping in the Tatun Volcanic Region, Taiwan. American Geophysical Union, Fall Meeting 2006, abstract #T33D-0541.

Chang, C.-H. (2004). Applications of a dense seismic network data on the study of seismogenic structures of central and eastern Taiwan. Doctoral Thesis, National Central University, 156p (in Chinese).

Chang, Y.-J. (2004). Vp, Vp/Vs and Qp three-dimensional structure inversion in Tatun Volcano Group. M.S. Thesis, National Chung Cheng University, 73p (in Chinese).

Chen, C.-H., Wu, Y.-J., & Wu, Y.-C. (1971). Volcanic geology of the Tatun geothermal area, northern Taiwan. *Proceedings of the Geological Society of China, 14*, 5-20.

Chen, K.-C. (2003). Strong ground motion and damage in the Taipei basin from the Moho reflected seismic waves during the March 31,2002, Hualien, Taiwan earthquake. *Geophysical Research Letters, 30*(11), 1551.

Chen, K.-J., & Yen, Y.-H. (1991). Gravity and microearthquake studies in the Chinshan-Tanshui area, northern Taiwan. *Terrestrial, Atmospheric and Oceanic Sciences, 2*(1), 35-50.

Chen, W.-S., Yang, C.-C., Tang, H.-C., & Liu, J.-K. (2003). Volcanic landform and

sequences of the Tatun Volcanoes. *Bulletin of the Central Geological Survey, 16*, 99-123 (in Chinese).

Clifford, P., Greenhalgh, S., Houseman, G., & Graeber, F. (2008). 3-D seismic tomography of the Adelaide fold belt. *Geophysical Journal International, 172*, 167-186.

DeGroot, M. H. (1975). *Probability and Statistics*: Reading, Mass. : Addison-Wesley.

Dias, N. A., Matias, L., Lourenco, N., Madeira, J., Carrilho, F., & Gaspar, J. L. (2007). Crustal seismic velocity structure near Faial and Pico Islands (AZORES), from local earthquake tomography. *Tectonophysics, 445*, 301-317.

Eberhart-Phillips, D. (1990). Three-dimensional P and S velocity structure in the Coalinga region, California. *Journal of Geophysical Research, 95*(B10), 15,343-15,363.

Eberhart-Phillips, D., Stanley, W. D., Rodriguez, B. D., & Lutter, W. J. (1995). Surface seismic and electrical methods to detect fluids related to faulting. *Journal of Geophysical Research, 100*(B7), 12,919-12,936.

Evans, J. R., Eberhart-Phillips, D., & Thurber, C. H. (1994). User's manual for SIMULPS12 for imaging Vp and Vp/Vs: a derivative of the "Thurber" tomographic inversion SIMUL3 for local earthquakes and explosions, USGS Open-File Report 94-431.

Grand, S. P. (1987). Tomographic inversion for shear velocity beneath the North American plate. *Journal of Geophysical Research, 92*(B13), 14,065–14,090.

Hill, D. P., Langbein, J. O., & Prejean, S. (2003). Relations between seismicity and deformation during unrest in Long Valley Caldera, California, from 1995 through 1999. *Journal of Volcanology and Geothermal Research, 127*(3-4), 175-193.

Ho, C. S. (1974). The Taipei fault and related structural features in northern Taiwan.

Proceedings of the Geological Society of China, 17, 95-109.

Ho, H.-H. (2001). *The volcanic gas sources of Tatun volcano Group, Northern Taiwan.* M.S. Thesis, National Taiwan University, 80p (in Chinese).

Hu, J.-C., Angelier, J., Lee, J.-C., Chu, H.-T., & Byrne, D. (1996). Kinematics of convergence, deformation and stress distribution in the Taiwan collision area: 2-D finite-element numerical modelling. *Tectonophysics, 255*, 243-268.

Hu, J.-C., Yu, S.-B., Chu, H.-T., & Angelier, J. (2002). Transition tectonics of northern Taiwan induced by convergence and trench retreat. *Geological Society of America, Special Paper 358*, 147-160.

Huang, S.-Y., Rubin, C. M., Chen, Y.-G., & Liu, H.-C. (2007). Prehistoric earthquakes along the Shanchiao fault, Taipei basin, northern Taiwan. *Journal of Asian Earth Sciences, 31*, 265-276.

Huang, W.-G. (2008). Broadband Seismic Array in Taipei area. Retrieved December 20, 2008, from Acadrmia Sinica, Data Management Center of Institute of Earth Sciences Web site: http://www.earth.sinica.edu.tw/~smdmc/

Humphreys, E., & Clayton, R. W. (1988). Adaptation of Back Projection Tomography to Seismic Travel Time Problems. *JOURNAL OF GEOPHYSICAL RESEARCH, 93*(B2), 1,073-1,085.

Husen, S., Kissling, E., & Flueh, E. R. (2000). Local earthquake tomography of shallow subduction in north Chile: A combined onshore and offshore study. *Journal of Geophysical Research, 105*, 28,183-28,198.

Inoue, H., Fukao, Y., Tanabe, K., & Ogata, Y. (1990). Whole mantle P-wave travel time tomography *Physics of The Earth and Planetary Interiors, 59*(4), 294-328.

Juang, W.-S., & Bellon, H. (1984). The potassium-argon dating of andesite from Taiwan. *Proceedings of the Geological Society of China, 27*, 86-100.

Juang, W.-S., & Chen, J.-C. (1989). Geochronology and geochemistry of volcanic rocks in northern Taiwan. *Bulletin of the Central Geological Survey, 5*, 31-66 (in Chinese).

Kim, K.-H., Chang, C.-H., Ma, K.-F., & Chiu, J.-M. (2005a). Modern seismic observations in the Tatun volcano region of northern Taiwan: Seismic/Volcanic hazard adjacent to the Taipei metropolitan area. *Terrestrial, Atmospheric and Oceanic Sciences, 16*(3), 579-594.

Kim, K.-H., Chiu, J.-M., Pujol, J., Chen, K.-C., Huang, B.-S., & Yeh, Y.-H. (2005b). Three-dimensional Vp and Vs structural models associated with the active subduction and collision tectonics in the Taiwan region. *Geophysical Journal International, 162*, 204-220.

Kissling, E. (1988). Geotomography with local earthquake data. *Reviews of Geophysics, 26*(4), 659-698.

Kissling, E., Ellsworth, W. L., Eberhart-Phillips, D., & Kradolfer, U. (1994). Initial reference models in local earthquake tomography. *Journal of Geophysical Research, 99*(B10), 19,635-19,646.

Kissling, E. (1995). Velest Users Guide. Internal report 26, Institute of Geophysics and Swiss Seismological Service, ETH Zurich, Switzerland.

Konstantinou, K. I., Lin, C.-H., & Liang, W.-T. (2007). Seismicity characteristics of a potentially active Quaternary volcano: The Tatun volcano group, northern Taiwan. *Journal of Volcanology and Geothermal Research, 160*, 300-318.

Kurashimo, E., & Hirata, N. (2004). Low Vp and Vp/Vs zone beneath the northern Fossa Magna basin, central Japan, derived from a dense array observation. *Earth Planets Space, 56*, 1301-1308.

Lee, H.-F., Yang, T. F., Lan, T. F., Chen, C.-H., Song, S.-R., & Tsao, S. (2008). Temporal

variations of gas compositions of fumaroles in the Tatun Volcano Group, northern Taiwan. *Journal of Volcanology and Geothermal Research, 178*(4), 624-635

Lee, J.-F., Lin, C.-C., Lai, D.-C., Su, T.-W., Chiu, Z.-L., & Zeng, C.-J. (1999). The study on the formation of Taipei basin. *Central Geological Survey Special Publication, 11*, 207-226 (in Chinese).

Lees, J. M. (2007). Seismic tomography of magmatic systems. *Journal of Volcanology and Geothermal Research, 167*, 37-56.

Lin, C.-H., Konstantinou, K. I., Liang, W.-T., Pu, H.-C., Lin, Y.-M., & You, S.-H. (2005a). Preliminary analysis of volcanoseismic signals recorded at the Tatun Volcano Group, northern Taiwan. *Geophysical Research Letters, 32*.

Lin, C.-H., Konstantinou, K. I., Pu, H.-C., Hsu, C.-C., Lin, Y.-M., & You, S.-H. (2005b). Preliminary Results from Seismic Monitoring at the Tatun Volcanic Area of Northern Taiwan. *Terrestrial, Atmospheric and Oceanic Sciences, 16*(3), 563-577.

Lin, C.-H. & Pu, H.-C. (2007). The potential magma chamber and long-term micro-earthquake observation project in TVG (V). Journal of National Park, p.176 (in Chinese).

Lin, G., Shearer, P. M., Hauksson, E., & Thurber, C. H. (2007). A three-dimensional crustal seismic velocity model for southern California from a composite event method. *Journal of Geophysical Research, 112*, B11306.

Lu, C.-Y., Angelier, J., Chu, H.-T., & Lee, J.-C. (1995). Contractional, transcurrent, rotational and extensional tectonics: Examples from northern Taiwan. *Tectonophysics, 246*, 129-146.

Mallet, J. L. (1989). DSI: Discrete Smooth Interpolation. *ACM Transactions on Graphics, 8*, 121-144.

Mallet, J. L. (1992). Discrete smooth interpolation in geometric modelling.

Computer-Aided Design, 24(4), 178-191.

Matsubara, M., Obara, K., & Kasahara, K. (2008). Three-dimensional P- and S-wave velocity structures beneath the Japan Islands obtained by high-density seismic stations by seismic tomography. *Tectonophysics, 454*(1-4), 86-103.

Motoki, A., & Sichel, S. E. (2008). Hydraulic fracturing as a possible mechanism of dyke-sill transitions and horizontal discordant intrusions in trachytic tabular bodies of Arraial do Cabo, State of Rio de Janeiro, Brazil. *Geofísica Internacional, 47*(1), 13-25.

Murase, M., Ishikawa, K., Lin, C. H., Lin, J. J., Pu, H. C., Kimata, F., Miyajima, R., Nakamichi, H., & Suzuki, A. (2007). Estimated pressure source and vertical deformation in Tatun volcano group, Taiwan, detected by precise leveling in June 2006-August 2007. American Geophysical Union, Fall Meeting 2007, abstract #V11C-0740.

Nakamichi, H., Watanabe, H., & Ohminato, T. (2007). Three-dimensional velocity structures of mount Fuji and the South Fossa Magna, central Japan. *Journal of Geophysical Research, 112*, B03310.

Natale, G. D., Troise, C., Trigila, R., Dolfi, D., & Chiarabba, C. (2004). Seismicity and 3-D substructure at Somma-Vesuvius volcano: Evidence for magma quenching. *Earth and Planetary Science Letters, 221*, 181-196.

Nolet, G. (1978). Simultaneous inversion of seismic data. *Geophysical Journal International, 55*(3), 679-691.

Nolet, G., (1987). Seismic wave propagation and seismic tomography, in, *Seismic Tomography*, pp. 1-23, ed. Nolet, G., Reidel, Dordrecht.

Patane, D., Chiarabba, C., Cocina, O., Gori, P. D., Moretti, M., & Boschi, E. (2002). Tomographic images and 3D earthquake locations of the seismic swarm

preceding the 2001 Mt. Etna eruption: Evidence for a dyke intrusion. *Geophysical Research Letters, 29*(10), 1497.

Pavlis, G. L., & Booker, J. R. (1980). The mixed discrete-continuous inverse problem: application to the simultaneous determination of earthquake hypocenters and velocity structure. *Journal of Geophysical Research, 85*(B9), 4801-4810.

Pavlis, G. L., & Booker, J. R. (1983). A study of the importance of nonlinearity in the inversion of earthquake arrival time data for velocity structure. *Journal of Geophysical Research, 88*(B6), 5047-5055.

Shyu, J. B. H., Sieh, K., Chen, Y.-G., & Liu, C.-S. (2005). Neotectonic architecture of Taiwan and its implications for future large earthquakes. *Journal of Geophysical Research, 110*, B08402.

Song, S.-R., Tsao, S., & Lo, H.-J. (2000a). Characteristics of the Tatun Volcanic eruptions, North Taiwan: Implications for a cauldron formation and volcanic evolution. *Journal of the Geological Society of China, 43*(2), 361-378.

Song, S.-R., Yang, T. F., Yeh, Y.-H., Tsao, S.-J., & Lo, H.-J. (2000b). The Tatun volcano group is active or extinct? *Journal of the Geological Society of China, 43*(3), 521-534.

Suppe, J. (1984). Kinematics of arc-continent collison, flipping of subduction, and back-arc spreading near Taiwan. *Memoir of the Geological Society of China, 6*, 21-33.

Tahara, M., Uehira, K., Shimizu, H., Nakada, M., Yamada, T., Mochizuki, K. (2008). Seismic velocity structure around the Hyuganada region, Southwest Japan, derived from seismic tomography using land and OBS data and its implications for interplate coupling and vertical crustal uplift. *Physics of the Earth and Planetary Interiors, 167*, 19-33.

Teng, L. S. (1996). Extensional collapse of the northern Taiwan mountain belt. *Geology, 24*(10), 949-952.

Teng, L. S., Lee, C. T., Peng, C.-H., Chen, W.-F., & Chu, C.-J. (2001). Origin and geological evolution of the Taipei basin, northern Taiwan. *Western Pacific Earth Sciences, 1*, 115-142.

Teng, L. S., Lee, C.-T., Liew, P.-M., Song, S.-R., Tsao, S.-J., Liu, H.-C. (2004). On the Taipei Dammed Lake. *Journal of Geographical Science, 36*, 77-100 (in Chinese).

Thurber, C. H. (1983). Earthquake locations and three-dimensional crustal structure in the Coyote Lake area, central California. *Journal of Geophysical Research, 88*(B10), 8226-8236.

Thurber, C. H., & Aki, K. (1987). Three-Dimensional Seismic Imaging. *Annual Review of Earth and Planetary Sciences, 15*, 115-139.

Thurber, C. H. (1993). Local earthquake tomography: velocities and Vp/Vs-theory. In H. M. Iyer & K. Hirahara (Eds.), Seismic Tomography, 563-583, London: Chapman and Hall.

Thurber, C. H., & Atre, S. R. (1995). Three-dimensional Vp and Vp/Vs structure at Loma Prieta, California, from local earthquake tomography. *Geophysical Research Letters, 22*(22), 3,079-3,082.

Thurber, C. H., & Eberhart-Phillips, D. (1999). Local earthquake tomography with flexible gridding. *Computers & Geosciences, 25*, 809-818.

Um, J., & Thurber, C. (1987). A fast algorithm for two-point seismic ray tracing. *Bulletin of the Seismological Society of America, 77*(3), 972-986.

Wang, C.-Y., Lee, Y.-H., Ger, M.-L., & Chen, Y.-L. (2004). Investigating subsurface structures and P- and S-wave velocities in the Taipei basin. *Terrestrial, Atmospheric and Oceanic Sciences, 15*(4), 609-627.

Wang, K.-L., Chung, S.-L., Chen, C.-H., Shinjo, R., Yang, T. F., & Chen, C.-H. (1999). Post-collisional magmatism around northern Taiwan and its relation with opening of the Okinawa Trough. *Tectonophysics, 308*, 363-376.

Wang, W.-H., & Chen, C.-H. (1990). The volcanology and fission track age dating of pyroclastic deposits in Tatun Volcano Group, northern Taiwan. *Acta Geol. Taiwan, 28*, 1-30.

Wang, Y.-R. (2007). 3D Finite Difference Simulation-Based Site Response Analysis of Taipei Basin. M.S. Thesis, National Central University, 107p.

Wright, T. J., Ebinger, C., Biggs, J., Ayele, A., Yirgu, G., & Keir, D. (2006). Magma-maintained rift segmentation at continental rupture in the 2005 Afar dyking episode. *Nature, 442*, 291-294.

Wu, Y.-M., Chang, C.-H., Hsiao, N.-C., & Wu, F. T. (2003). Relocation of the 1998 Rueyli, Taiwan, earthquake sequence using three-dimensions velocity structure with stations corrections. *Terrestrial, Atmospheric and Oceanic Sciences, 14*(4), 421-430.

Wu, Y.-M., Chang, C.-H., Zhao, L., Shyu, J. B. H., Chen, Y.-G., & Sieh, K. (2007). Seismic tomography of Taiwan: Improved constraints from a dense network of strong motion stations. *Journal of Geophysical Research, 112*, B08312.

Wu, Y.-M., Zhao, L., Chang, C.-H., & Hsu, Y.-J. (2008). Focal-mechanism determination in Taiwan by genetic algorithm. *Bulletin of the Seismological Society of America, 98*(2), 651-661.

Yang, C.-C., Liu, J.-K., Huang, M.-T., & Chen, W.-S. (2004). DTM for Mapping the Volcanic Landforms of Tatun Volcano Group in Northern Taiwan. *Journal of Photogrammetry and Remote Sensing, 9*(2), 1-8 (in Chinese).

Yang, C.-H., Shei, T.-C., & Lue, C.-C. (1994). Gravity and magnetic studies in the Tatun

volcanic region. *Terrestrial, Atmospheric and Oceanic Sciences, 5*(4), 499-514.

Yang, T. F., Sano, Y., & Song, S. R. (1999). $^{3}He/^{4}He$ ratios of fumaroles and bubbling gases of hot springs in Tatun volcano group, north Taiwan. *Il Nuovo Cimento C, 22*(03-04), 281-286.

Yang, T.F., Ho, H.H., Hsieh, P.S., Liu, N.J., Chen, Y.G., & Chen, C.-H., (2003). Sources of fumarolic gases from Tatun Volcano Group, North Taiwan. Journal of National Park 13, 127–156 (in Chinese).

Yang, Y., Ritzwoller, M. H., Levshin, A. L., & Shapiro, N. M. (2006). Ambient noise Rayleigh wave tomography across Europe. *Geophysical Journal International, 168*, 259-274.

Yeh, T. P., Tzou, Y.-H., & Lin, W.-H. (1984). Subsurface geology of the region of the Tatun Volcano Group. *Petroleum Geology of Taiwan, 20*, 143-154.

Yu, S.-B., Tsai, Y.-B., Hu, C.-C., & Lin, K.-A. (1980). Microearthquake and ground noise studies in the Tatun Volcanic region, northern Taiwan. *Bulletin of Exploration and Production Research.* Chinese Petroleum Corporation. *3*, 101-130 (in Chinese).

Yu, S.-B., Chen, H.-Y., & Kuo, L.-C. (1997). Velocity field of GPS stations in Taiwan area. *Tectonophysics, 274*, 41-59.

Yu, S.-B., Chen, H.-Y., Kuo, L.-C., Hou, C.-S., & Lee, J.-F. (1999). A study on the fault activities of the Taipei Basin. *Central Geological Survey Special Publication, 11*, 227-251 (in Chinese).

Zhao, D., Hasegawa, A., & Horiuchi, S. (1992). Tomographic Imaging of P and S Wave Velocity Structure Beneath Northeastern Japan. *Journal of Geophysical Research, 97*(B13), 19,909-19,928.

Zhao, D., Wang, Z., Umino, N., & Hasegawa, A. (2007). Tomographic Imaging outside a

Seismic Network: Application to the Northeast Japan Arc. *Bulletin of the Seismological Society of America, 97*(4), 1,121-1,132.

Zhang, H., & Thurber, C. H. (2003). Double-Difference Tomography: The Method and Its Application to the Hayward Fault, California. *Bulletin of the Seismological Society of America, 93*(5), 1,875-1,889.

Appendix

Ⅰ—1. An example of earthquake swarm and manual picking quality.

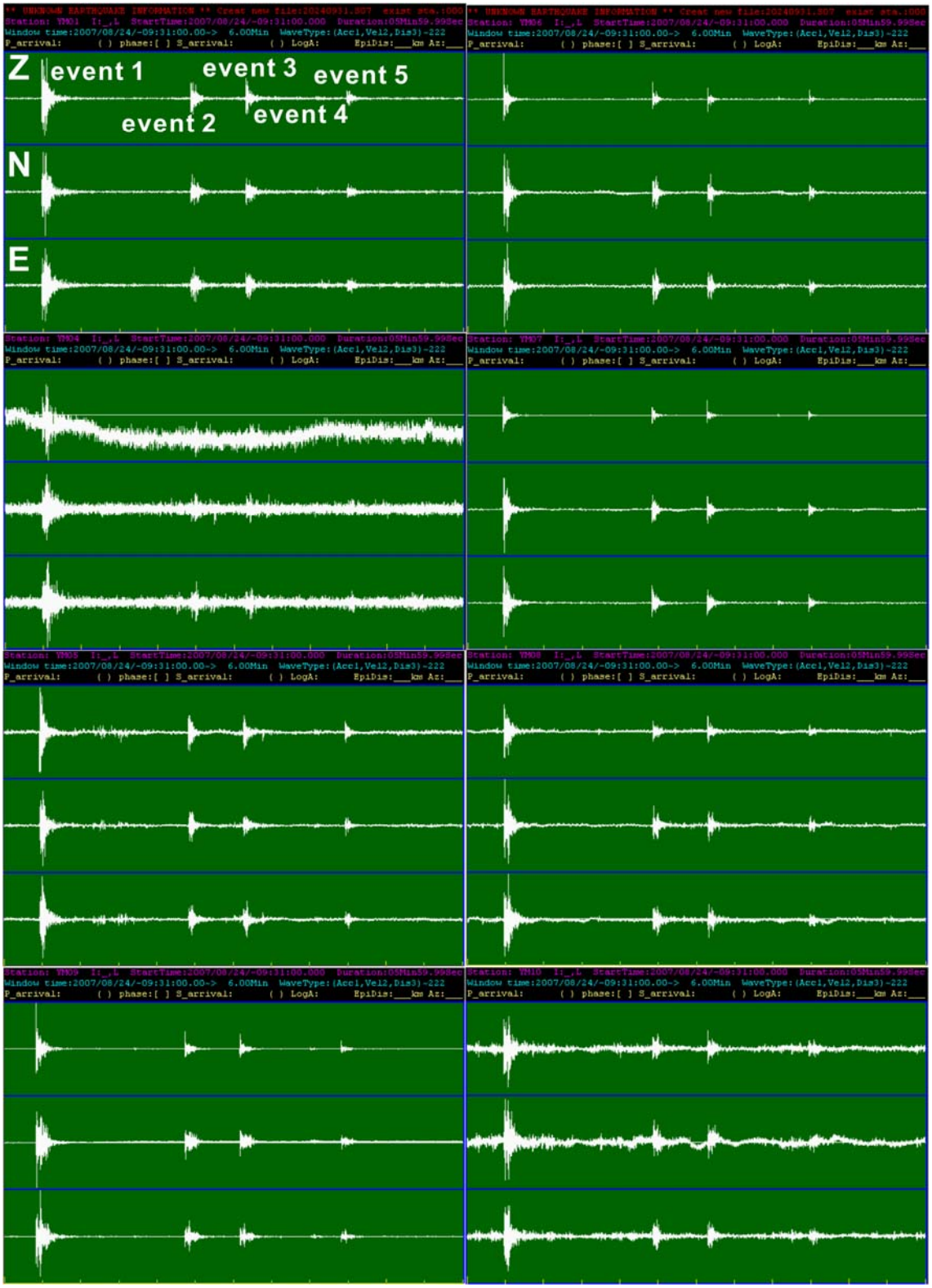

Ⅰ—1. An example of earthquake swarm and manual picking quality. (continued)

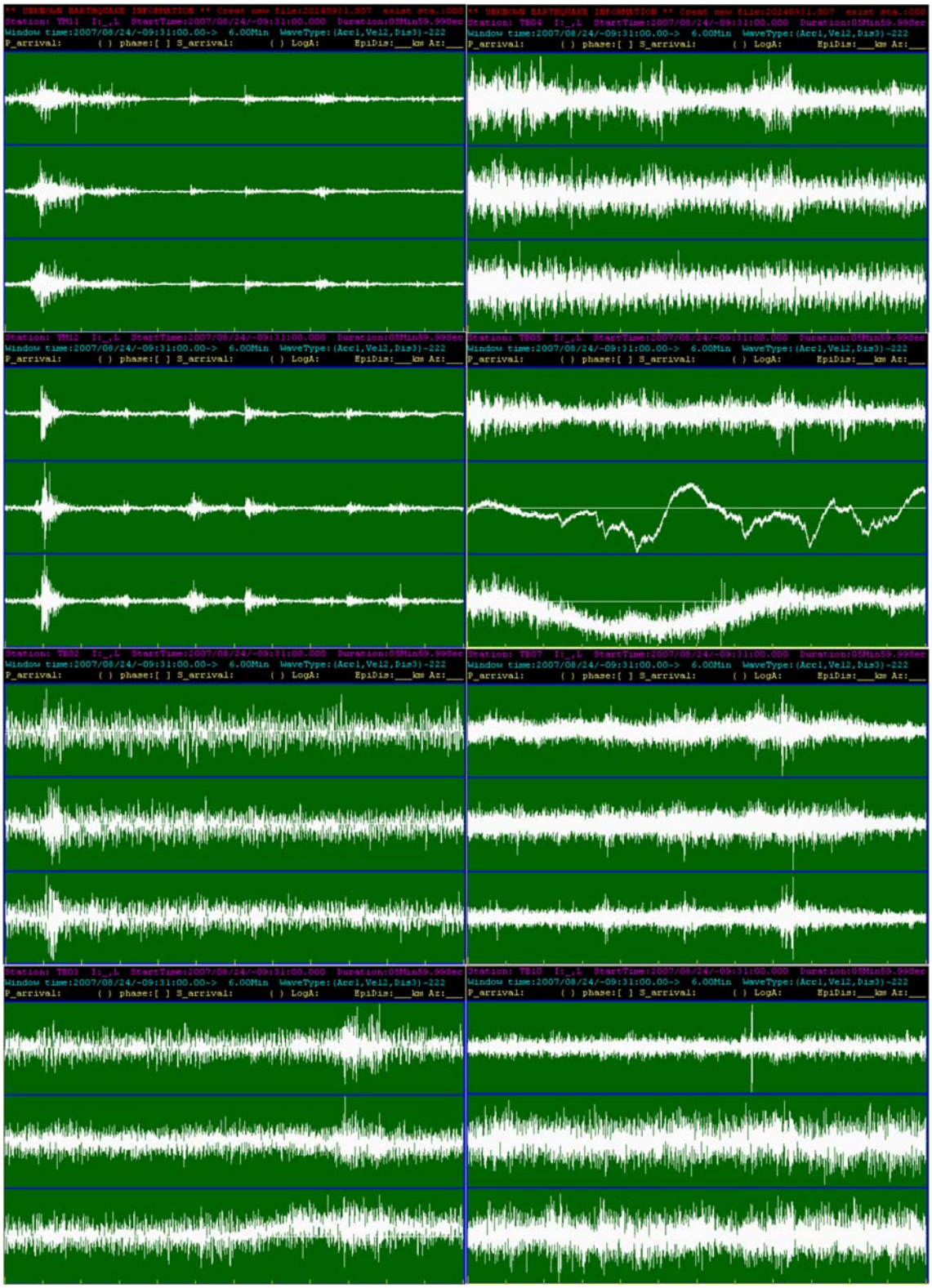

Ⅰ—1. An example of earthquake swarm and manual picking quality. (continued)

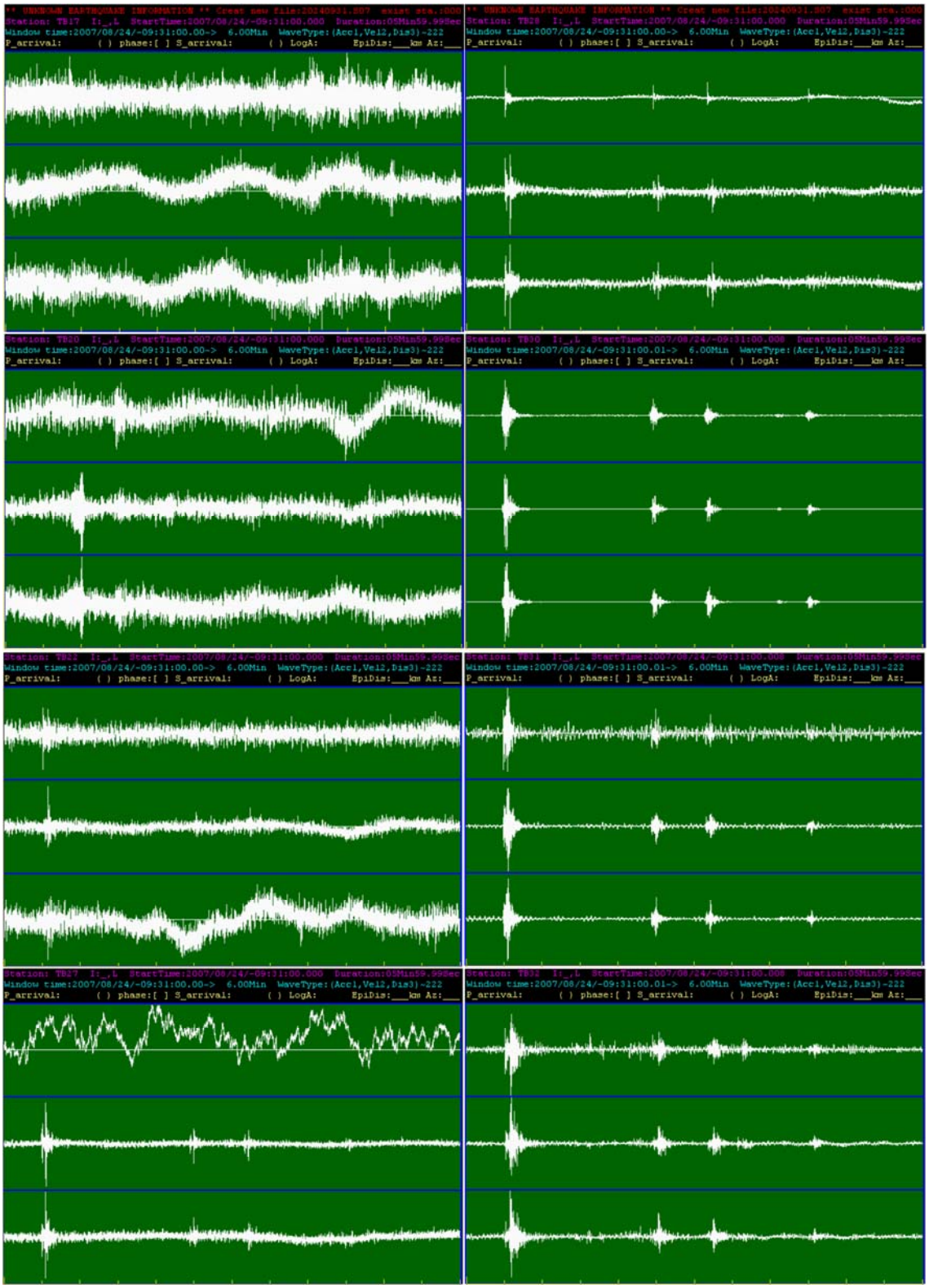

Ⅰ—2. The detail waveform of event 1.

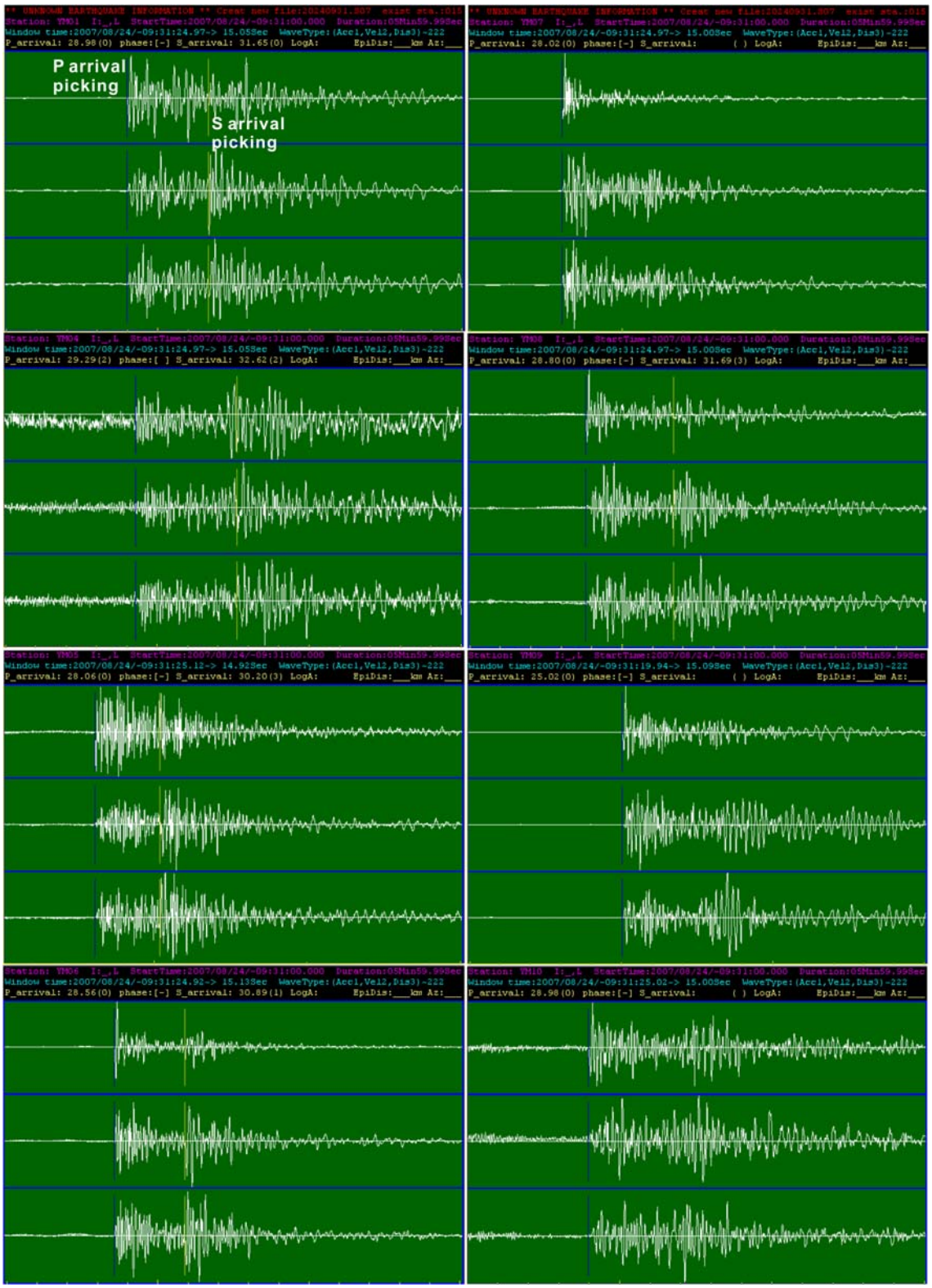

Ⅰ—2. The detail waveform of event 1. (continued)

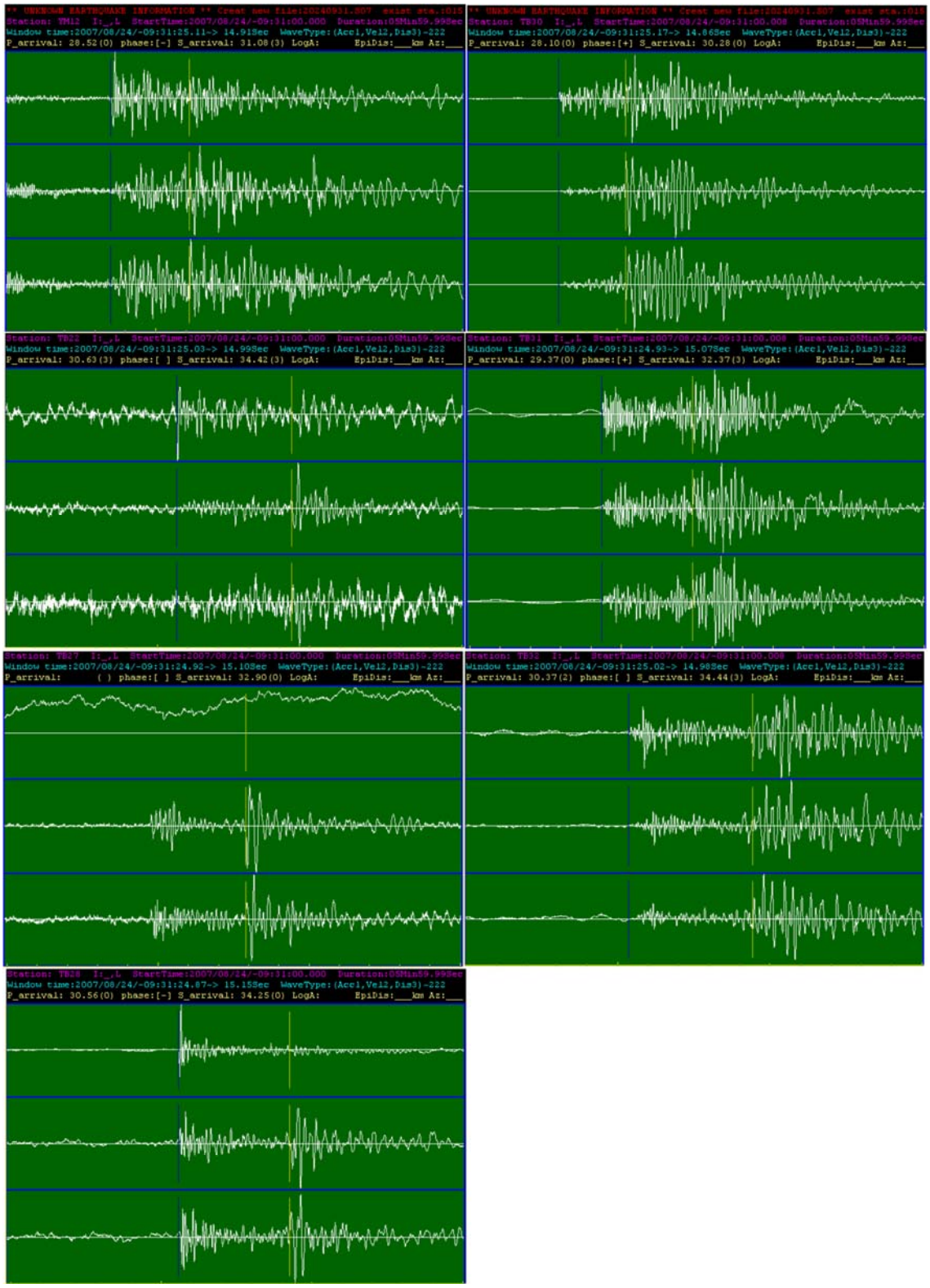

Ⅰ—3. The detail waveform of event 2.

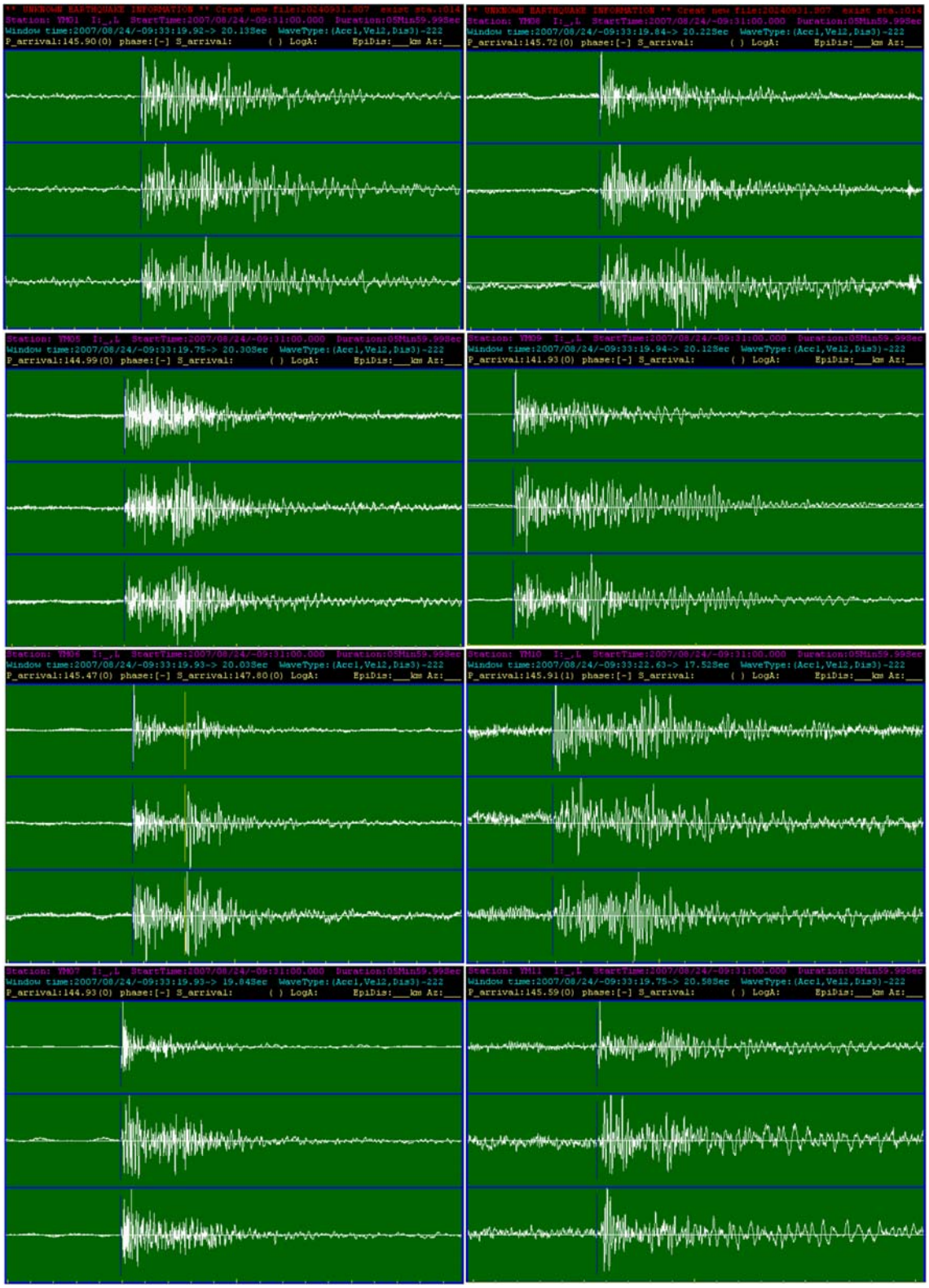

Ⅰ—3. The detail waveform of event 2. (continued)

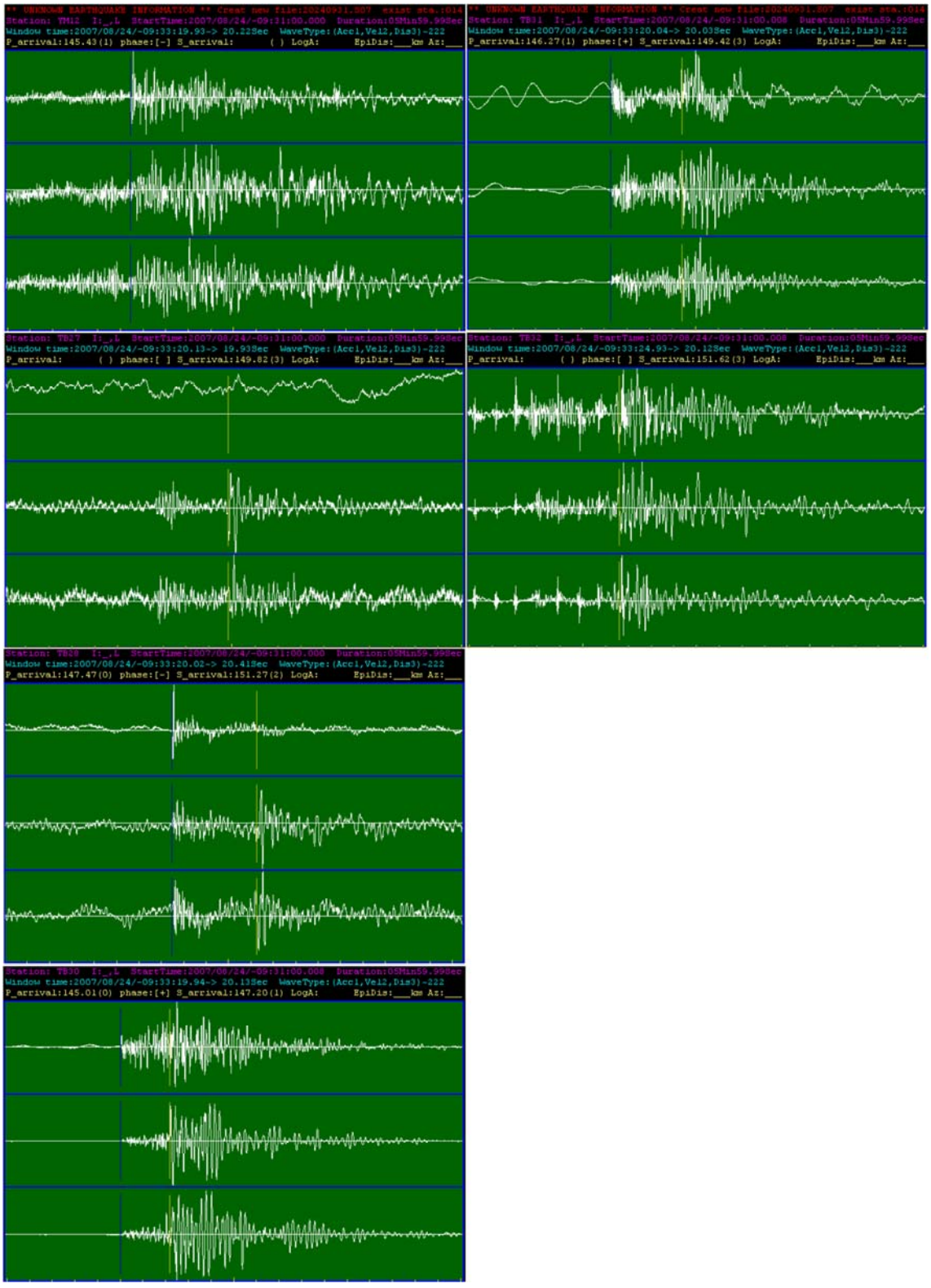

Ⅰ—4. The detail waveform of event 3.

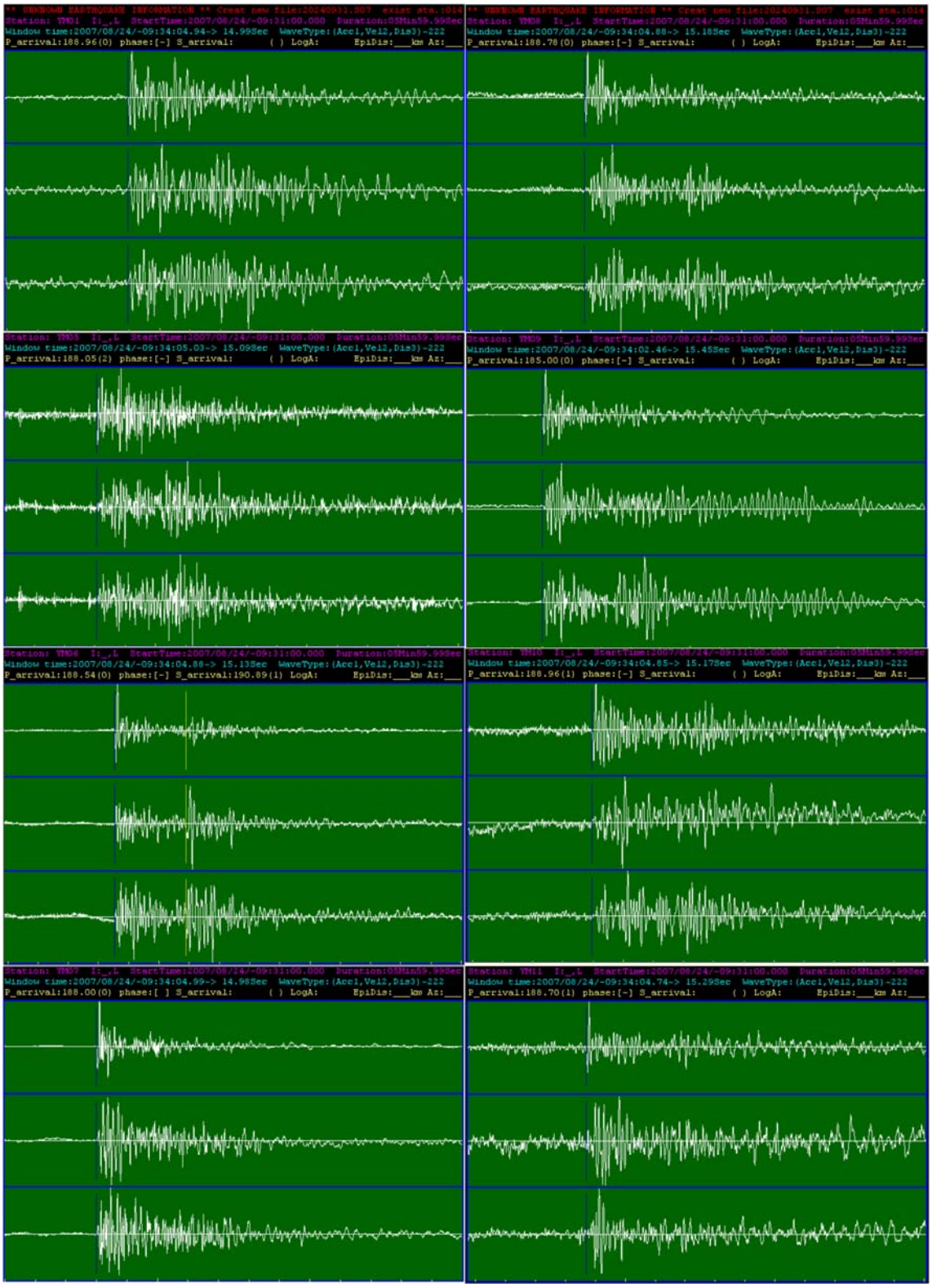

Ⅰ—4. The detail waveform of event 3. (continued)

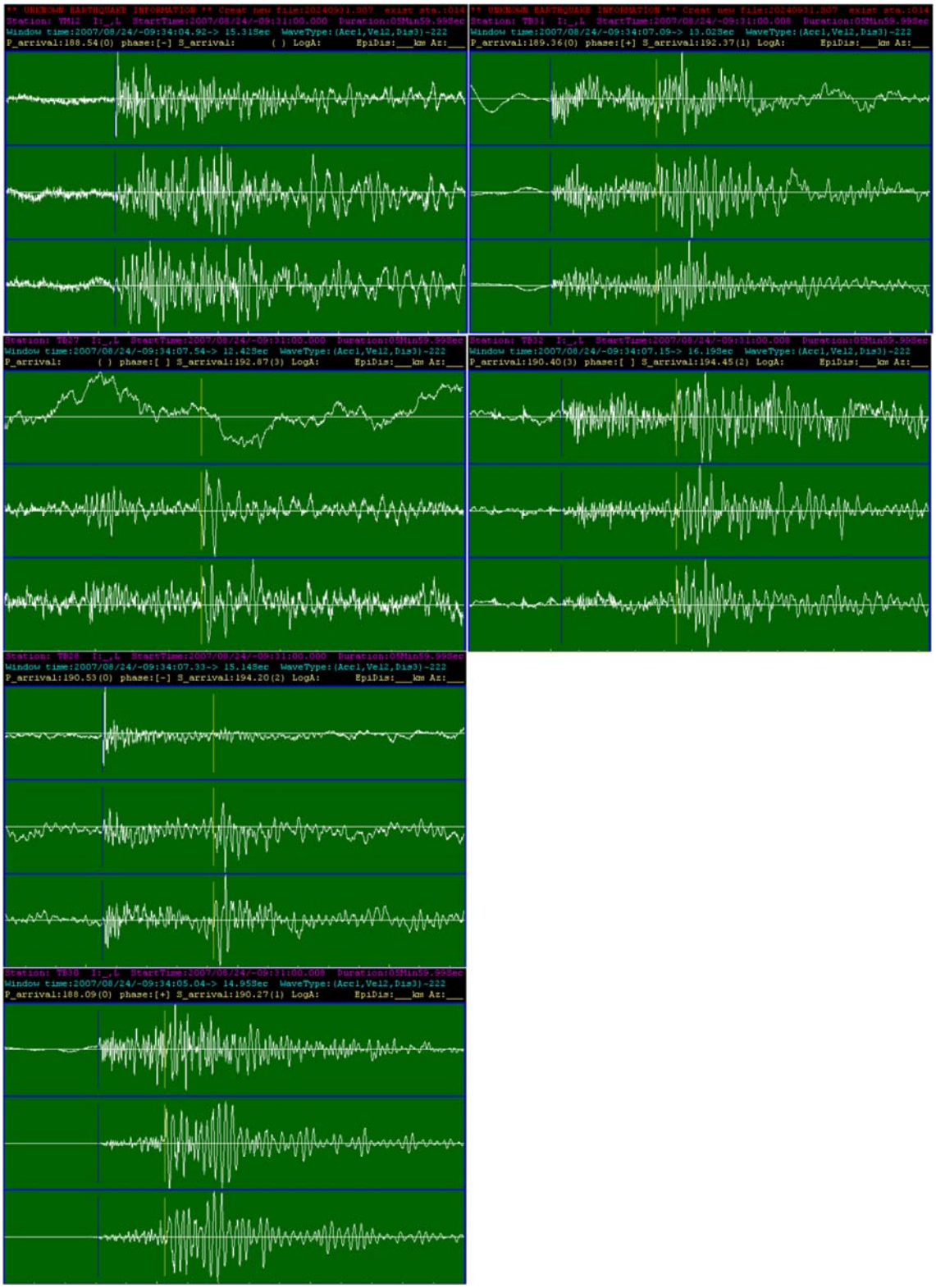

Ⅰ—5. The detail waveform of event 4.

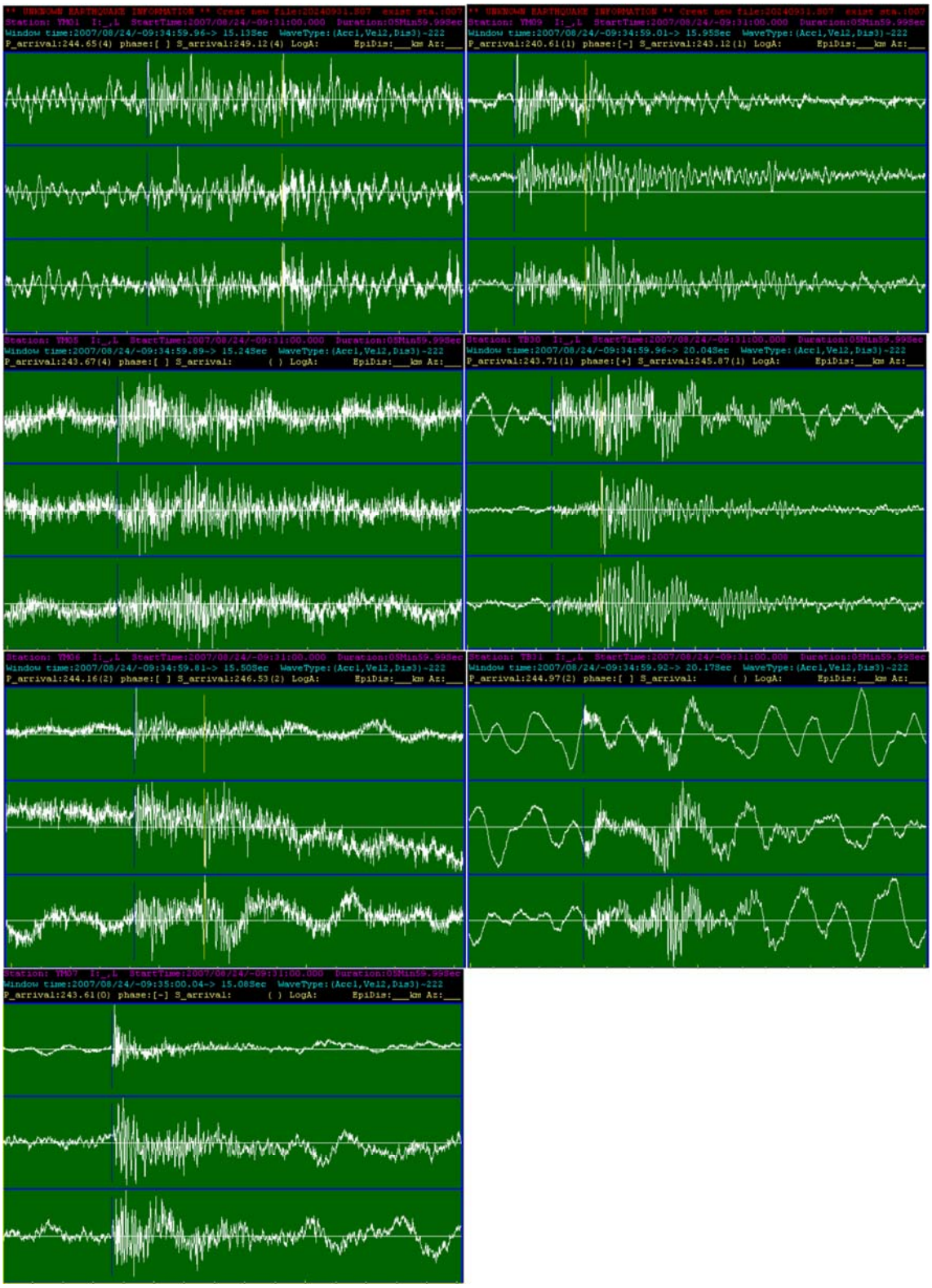

Ⅰ—6. The detail waveform of event 5.

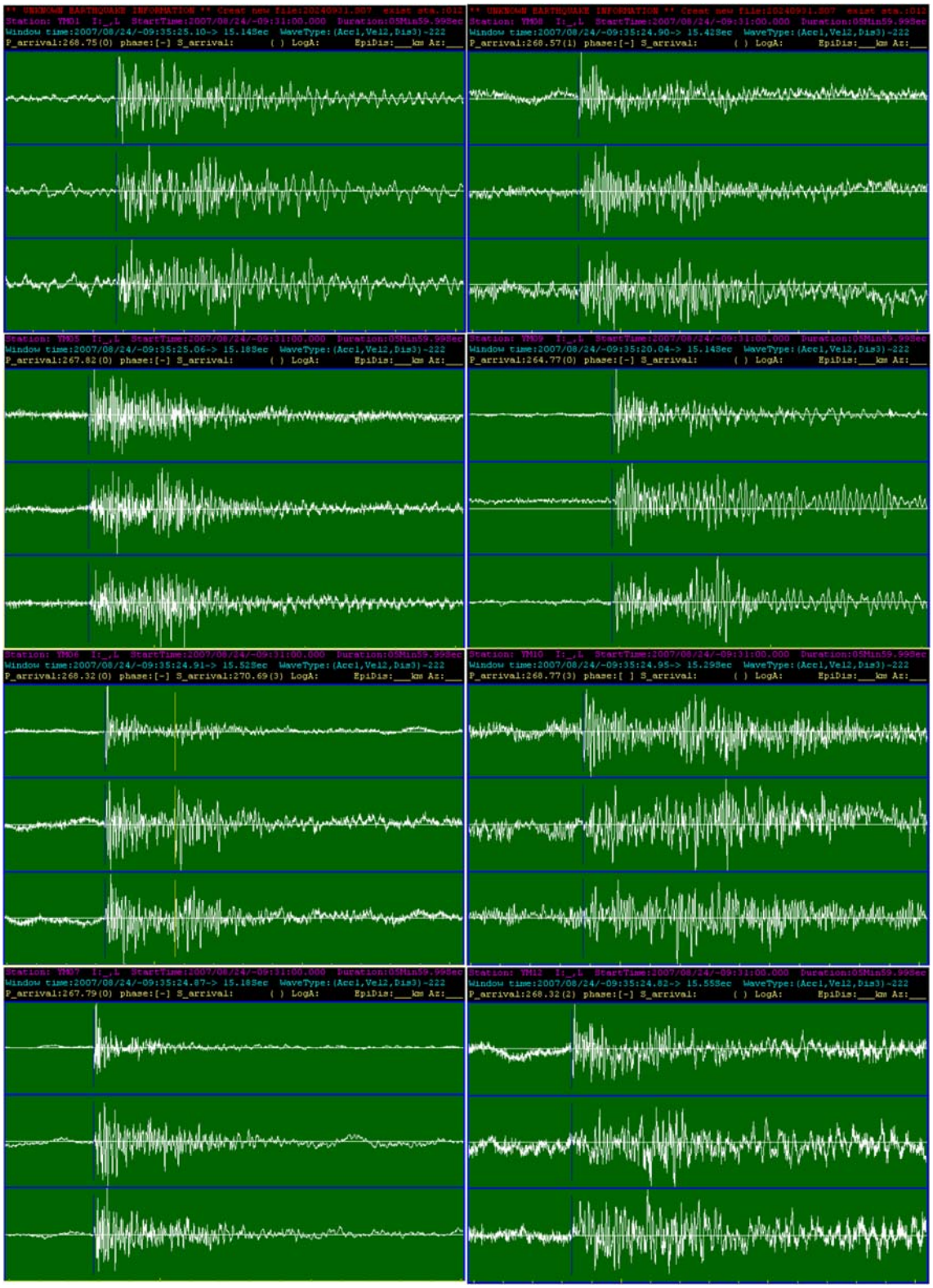

Ⅰ—6. The detail waveform of event 5. (continued)

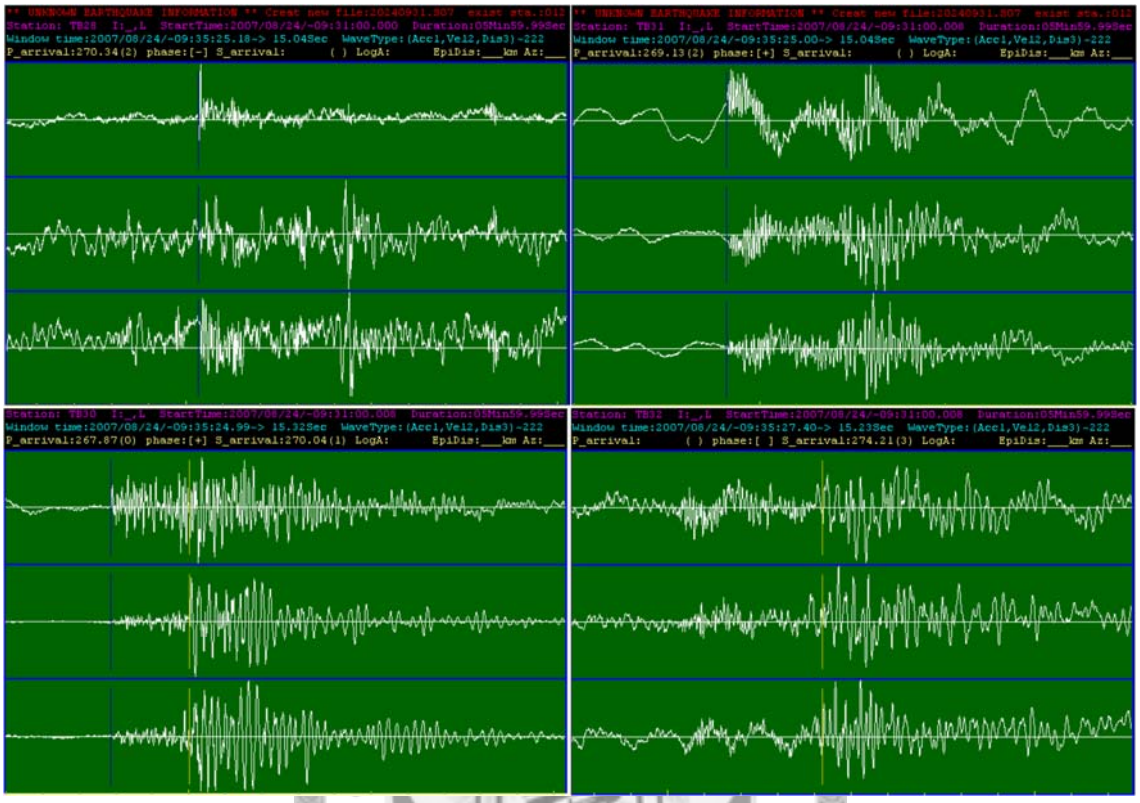

Ⅱ. Detail focal mechanism solutions in TVG.

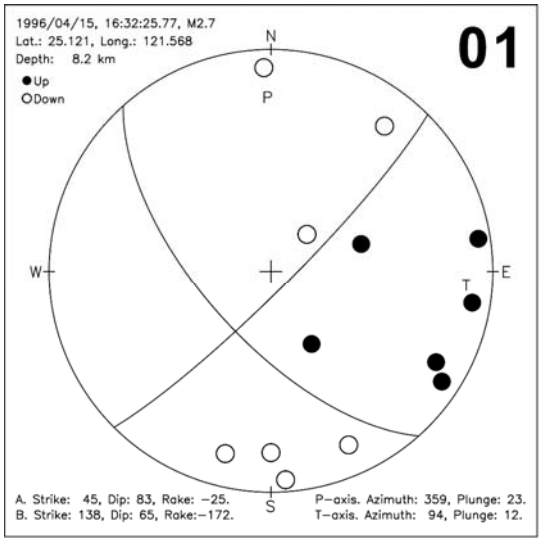

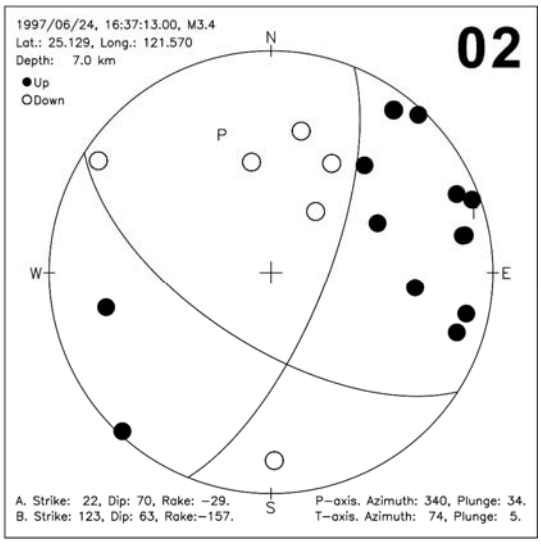

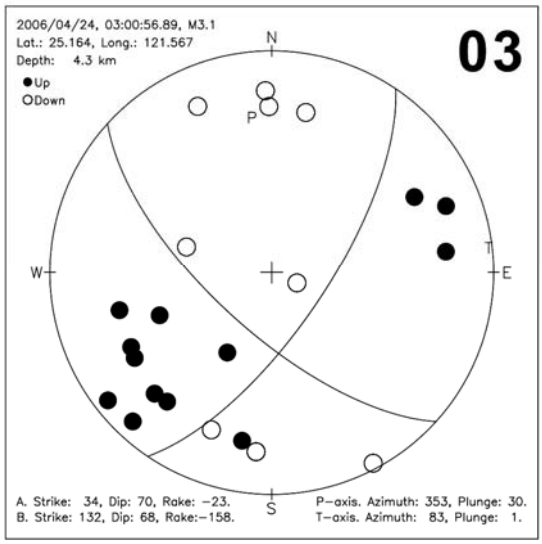

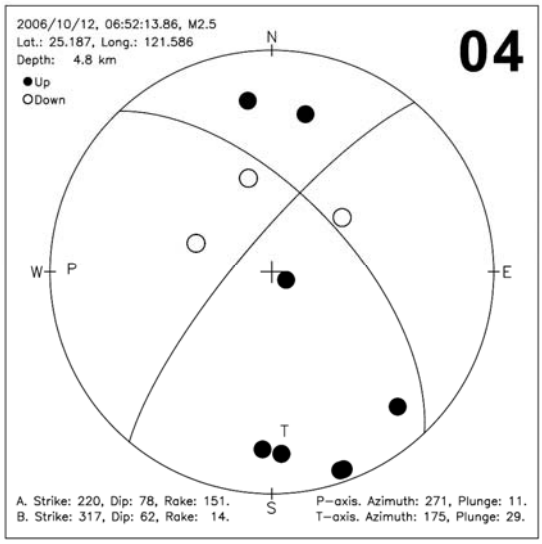

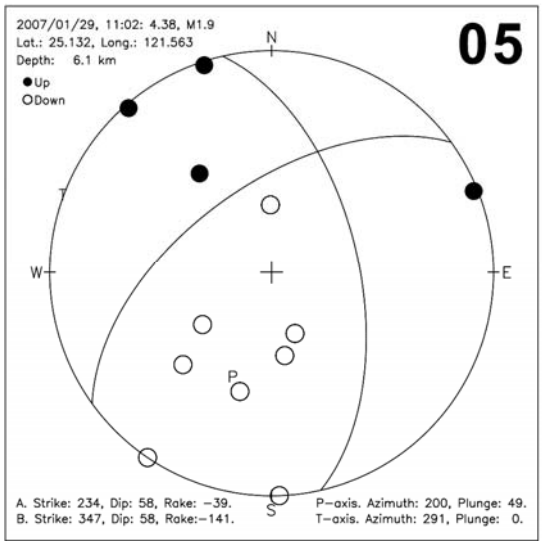

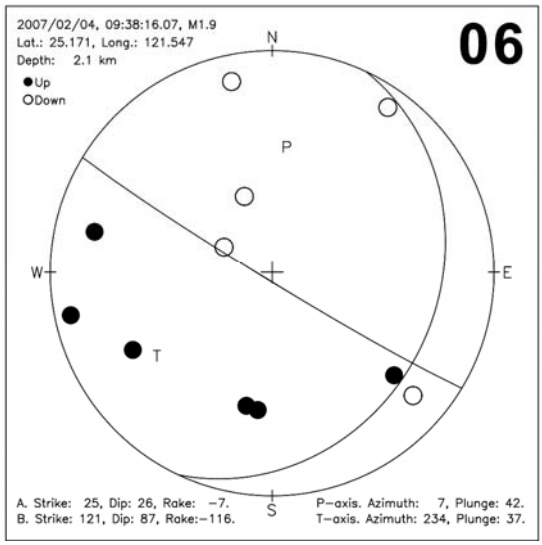

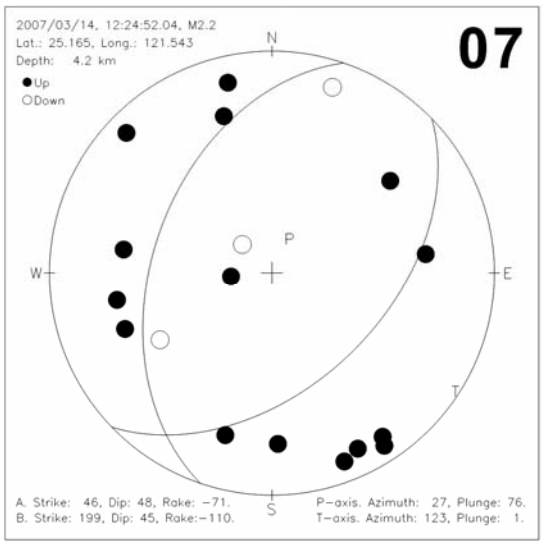
2007/03/14, 12:24:52.04, M2.2
Lat.: 25.165, Long.: 121.543
Depth: 4.2 km
●Up
○Down
07
N
W
E
S
P
T
A. Strike: 46, Dip: 48, Rake: −71.
B. Strike: 199, Dip: 45, Rake:−110.
P−axis. Azimuth: 27, Plunge: 76.
T−axis. Azimuth: 123, Plunge: 1.

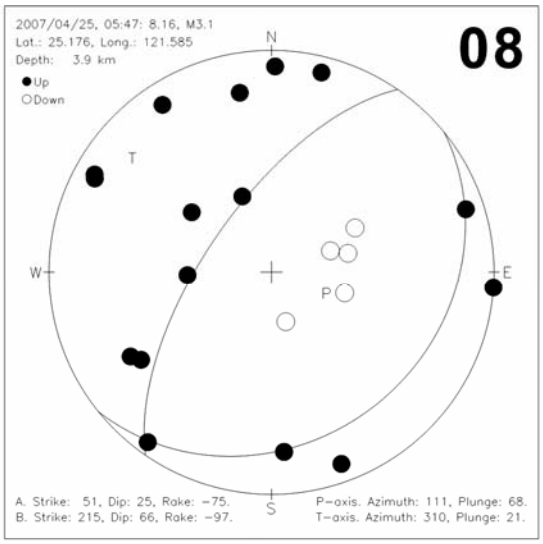
2007/04/25, 05:47: 8.16, M3.1
Lat.: 25.176, Long.: 121.585
Depth: 3.9 km
●Up
○Down
08
N
W
E
S
T
P
A. Strike: 51, Dip: 25, Rake: −75.
B. Strike: 215, Dip: 66, Rake: −97.
P−axis. Azimuth: 111, Plunge: 68.
T−axis. Azimuth: 310, Plunge: 21.

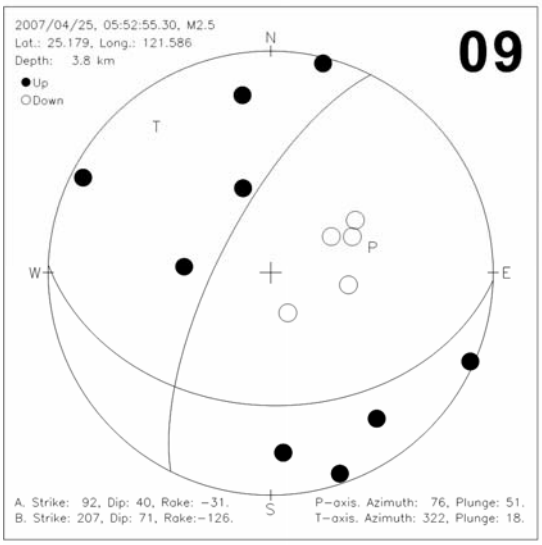
2007/04/25, 05:52:55.30, M2.5
Lat.: 25.179, Long.: 121.586
Depth: 3.8 km
●Up
○Down
09
N
W
E
S
T
P
A. Strike: 92, Dip: 40, Rake: −31.
B. Strike: 207, Dip: 71, Rake:−126.
P−axis. Azimuth: 76, Plunge: 51.
T−axis. Azimuth: 322, Plunge: 18.

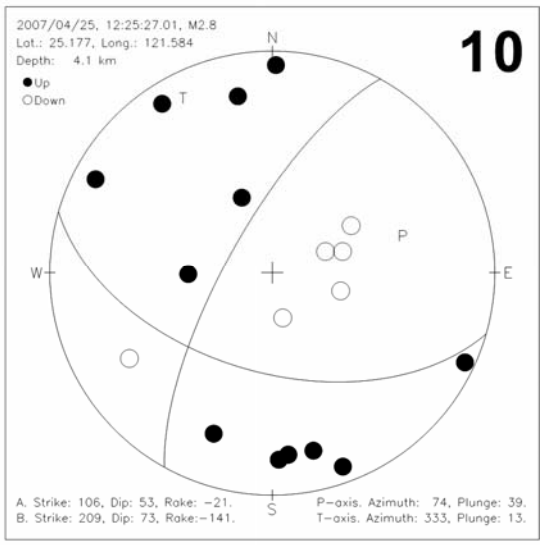
2007/04/25, 12:25:27.01, M2.8
Lat.: 25.177, Long.: 121.584
Depth: 4.1 km
●Up
○Down
10
N
W
E
S
T
P
A. Strike: 106, Dip: 53, Rake: −21.
B. Strike: 209, Dip: 73, Rake:−141.
P−axis. Azimuth: 74, Plunge: 39.
T−axis. Azimuth: 333, Plunge: 13.

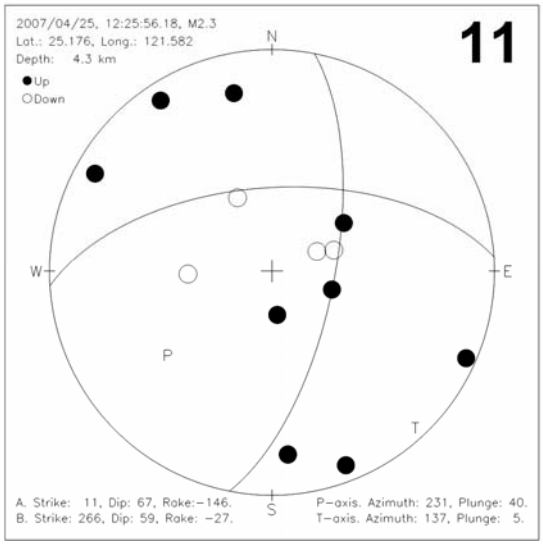
2007/04/25, 12:25:56.18, M2.3
Lat.: 25.176, Long.: 121.582
Depth: 4.3 km
●Up
○Down
11
N
W
E
S
P
T
A. Strike: 11, Dip: 67, Rake:−146.
B. Strike: 266, Dip: 59, Rake: −27.
P−axis. Azimuth: 231, Plunge: 40.
T−axis. Azimuth: 137, Plunge: 5.

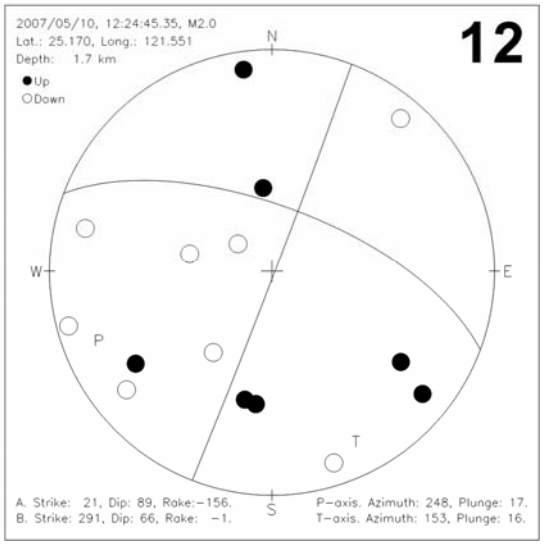
2007/05/10, 12:24:45.35, M2.0
Lat.: 25.170, Long.: 121.551
Depth: 1.7 km
●Up
○Down
12
N
W
E
S
P
T
A. Strike: 21, Dip: 89, Rake:−156.
B. Strike: 291, Dip: 66, Rake: −1.
P−axis. Azimuth: 248, Plunge: 17.
T−axis. Azimuth: 153, Plunge: 16.

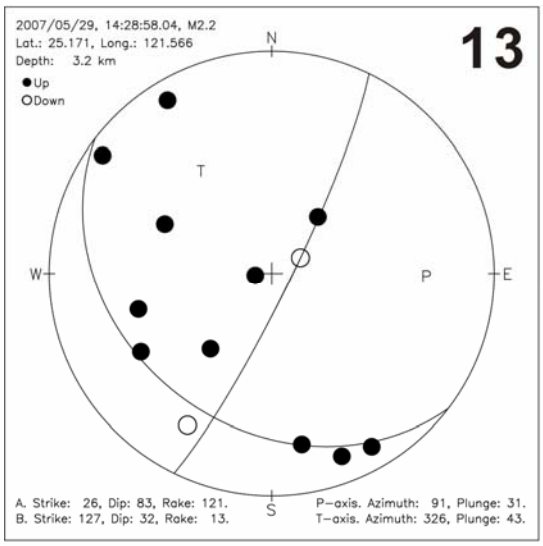
2007/05/29, 14:28:58.04, M2.2
Lat.: 25.171, Long.: 121.566
Depth: 3.2 km
Up
Down
13
N
W
E
S
T
P
A. Strike: 26, Dip: 83, Rake: 121.
B. Strike: 127, Dip: 32, Rake: 13.
P-axis. Azimuth: 91, Plunge: 31.
T-axis. Azimuth: 326, Plunge: 43.

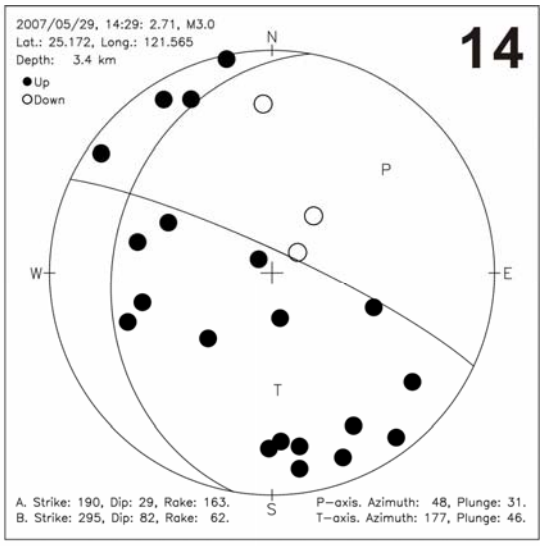
2007/05/29, 14:29: 2.71, M3.0
Lat.: 25.172, Long.: 121.565
Depth: 3.4 km
Up
Down
14
N
W
E
S
P
T
A. Strike: 190, Dip: 29, Rake: 163.
B. Strike: 295, Dip: 82, Rake: 62.
P-axis. Azimuth: 48, Plunge: 31.
T-axis. Azimuth: 177, Plunge: 46.

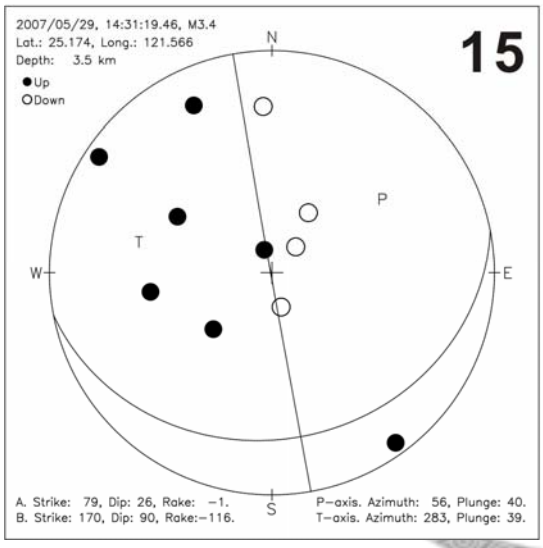
2007/05/29, 14:31:19.46, M3.4
Lat.: 25.174, Long.: 121.566
Depth: 3.5 km
Up
Down
15
N
W
E
S
P
T
A. Strike: 79, Dip: 26, Rake: -1.
B. Strike: 170, Dip: 90, Rake:-116.
P-axis. Azimuth: 56, Plunge: 40.
T-axis. Azimuth: 283, Plunge: 39.

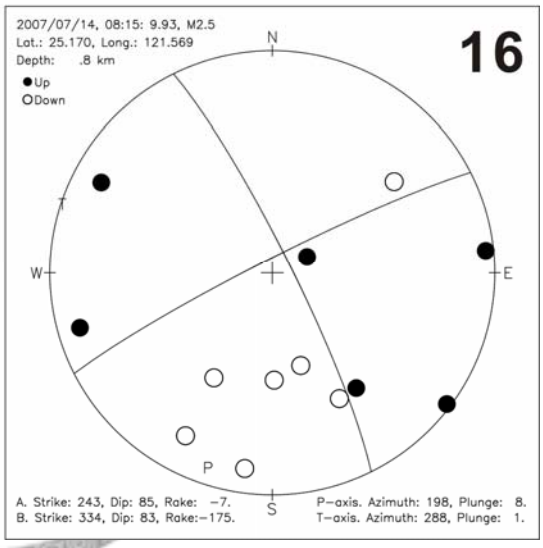
2007/07/14, 08:15: 9.93, M2.5
Lat.: 25.170, Long.: 121.569
Depth: .8 km
Up
Down
16
N
W
E
S
T
P
A. Strike: 243, Dip: 85, Rake: -7.
B. Strike: 334, Dip: 83, Rake:-175.
P-axis. Azimuth: 198, Plunge: 8.
T-axis. Azimuth: 288, Plunge: 1.